Complete oxidation of trans-4-pentylcyclohexanecarboxylic acid by catalytic ozonation using Cu-Mg bi-metallic catalysts

By

Miguel Aguilar Coronado

A Thesis submitted to
the Faculty of Graduate Studies
of Lakehead University of Thunder Bay
in partial fulfilment of the requirements
for the degree of
Master of Science in Chemical Engineering
Lakehead University
Thunder Bay

© Copyright Miguel Aguilar Coronado, March 2024. All rights reserved.

Abstract

This thesis studied the use of a bi-metallic Cu and Mg catalyst dispersed on γ-Al_2O_3 for the complete oxidation of a naphthenic acid (NA) model compound, trans-4-pentylcyclohexanecarboxylic acid (4PCH) by ozone. Mono-metallic Cu and Mg, and bi-metallic Cu-Mg catalysts were tested for the ozonation of 4PCH. The catalysts were characterized by ICP-OES, BET, SEM, TEM, XRD, NH_3-TPD and XPS. It was found that bi-metallic catalysts with high amount of surface hydroxyl groups and with pH_{pzc} close to the pH of the solution at 8.5 were suitable for the mineralization of 4PCH. The catalyst with 1 and 5 wt% of Cu and Mg loading, respectively, had the highest activity with 90% total organic carbon (TOC) removal at a dosage of 2 g/L in 120 min. The use of tert-butyl alcohol (TBA) confirmed the involvement of $OH^{\bullet}$ radicals in the oxidation mechanism of 4PCH. Mg fine-tuned the pH_{pzc} of the catalyst and provided a high concentration of neutrally charged surface hydroxyl groups to generate reactive oxygen species (ROS) to break down 4PCH in the liquid bulk. Cu participated in the complete oxidation of smaller carboxylic acid molecules through complexation and surface reactions with adsorbed ROS. The by-products of the oxidation of 4PCH were identified and a reaction network was proposed based on a meta-addition mechanism. The most active catalyst retained its TOC removal over 5 reusability cycles with an average Cu, Mg, and Al leaching of 0.07, 1.30 mg/L, and 0.2, respectively. The best performing catalyst was also proven effective for the complete oxidation of a mixture of 4 NA model compounds with an electric energy per order of 78.1 kWh/m^3.

Acknowledgement

Firstly, I would like to acknowledge my supervisors, Drs. Ebrahim Rezaei and Janusz Kozinski. This work would not have been possible without their funding. More importantly, their knowledge, patience and understanding were essential for the completion of this thesis. Their supervision pushed my abilities forward to achieve the objectives of my research.

I would like to thank the members of my thesis committee, Drs. Kang Kang and Francisco Ramos-Pallares. Their feedback was of great value on the improvement of this work.

Additionally, I am grateful to Lakehead University for providing me with the opportunity to obtain my master's degree.

I would also like to acknowledge Mohammad Babazadeh, whose PhD research was the pillar for this thesis. His listening and support were also essential to deepen the results of this thesis.

I am thankful for my friends in Canada, Martín, Fátima, and Yichen. They have made living in Canada a lovely experience.

I sincerely thank Fernanda Beltrán, whose care and kindness helped me believe in my abilities to complete this thesis. Her own ongoing pursue for working her best cheered me on to achieve a work that I can be proud of.

I would like to thank my father, Jorge Aguilar, for checking up on me daily and for always encouraging my ambitions. I would also like to thank my mother, Claudia Coronado, for always listening to me and for her emotional support. Above all, I would like to acknowledge my sibling, whose empathy and understanding have always helped me pursue what I think is best for me.

Table of contents

Abstract i

Acknowledgement ii

Table of contents iv

List of figures vii

List of tables xii

Abbreviations xiii

Nomenclature xv

Subscripts xv

Chapter 1: Introduction 1

1.1 Research background and motivation 1

1.2 Structure 3

Chapter 2: Literature review 4

2.1 Oil sands 4

2.1.1 Oil sands process water 4

2.2 Naphthenic acids and their removal methods from OSPW 6

2.2.1 Naphthenic acids 6

2.2.2 Removal methods of naphthenic acids from OSPW 8

2.2.2.1 Physico-chemical methods 8

2.2.2.2 Biological methods 10

2.2.2.3 Advanced oxidation processes 11

2.3 Ozonation of naphthenic acids 13

2.3.1 Ozone molecule 13

2.3.2 Single ozonation (non-catalytic ozonation of NAs) 15

2.3.3 Catalytic oxidation of NAs by ozone. 16

2.3.3.1 Interaction of ozone with catalysts 18

2.4 Knowledge gaps and research objectives 20

Chapter 3: Experimental 22

3.1 Catalyst synthesis and characterization 22

3.2 Model naphthenic acid molecules 24

3.3 Single (non-catalytic) and catalytic ozonation experiments 26

Chapter 4: Results and discussions 28

4.1 Optimization of the composition and dosage of Cu-Mg/γ-Al_2O_3 catalyst 28

4.2 Characterization of the mono-metallic and selected bi-metallic catalysts 40

4.3 Reaction mechanism and network 51

4.4 Insights into practical applications of the selected Cu(1)Mg(5)/γ-Al_2O_3 60

4.4.1 Reusability 60

4.4.2 Oxidation of a mixture of naphthenic acids 64

4.4.3 Toxicity of the by-products 70

Chapter 5: Conclusions and recommendations **73**

5.1 Conclusions 73

5.2 Recommendations for future work 75

References **77**

Appendix A: TOC calibration curve **95**

Appendix B: Repeatability of experiments **96**

Appendix C: Mass transfer limitations **99**

List of figures

Fig. 2.1. Generalized structure of monoacidic naphthenic acids. R represents aliphatic branching. Reprinted from Quinlan and Tam [21]. 7

Fig. 2.2. Surface charge dependence of surface hydroxyl groups. Adapted from Chen et al. (2015)[56]……………………………………………………………………………….19

Fig. 3.1. Schematic of the experimental set-up. Reprinted from Babazadeh et al. [10]....... 27

Fig. 4.1. Normalized TOC profiles of the mineralization of 4PCH using (a) 1g/L of γ-Al_2O_3, Cu(5)/γ-Al_2O_3, and Mg(5)/γ-Al_2O_3, (b) 1 g/L of Cu(5)Mg(x)/γ-Al_2O_3, (c) 1 g/L of Cu(x)Mg(5)/γ-Al_2O_3, and (d) 0.5 to 4 g/L of Cu(1)Mg(5)/γ-Al_2O_3. X = 1, 5, and 10 wt%, initial 4PCH concentration = 40 mg/L (TOC_0 = 29 mg/L), bicarbonate ionic strength = 5 mM, inlet gas phase ozone concentration = 23,616 ppmv, and initial pH = 8.5. The TOC profile of Cu(5)Mg(5)/γ-Al_2O_3 is shown twice in Figs. (b) and (c) for ease of comparison.31

Fig. 4.2. pH profiles the mineralization of 4PCH using (a) 1g/L of γ-Al_2O_3, Cu(5)/γ-Al_2O_3, and Mg(5)/γ-Al_2O_3, (b) 1 g/L of Cu(5)Mg(x)/γ-Al_2O_3, (c) 1 g/L of Cu(x)Mg(5)/γ-Al_2O_3, and (d) 0.5 to 4 g/L of Cu(1)Mg(5)/γ-Al_2O_3. x = 1, 5, and 10 wt%, initial 4PCH concentration = 40 mg/L (TOC_0 = 29 mg/L), bicarbonate ionic strength = 5 mM, inlet gas phase ozone concentration = 23,616 ppmv, and initial pH = 8.5. The TOC profile of the Cu(5)Mg(5)/γ-Al_2O_3 catalyst are shown twice in Figs (b) and (c) for ease of comparison. 33

Fig. 4.3. Liquid ozone concentration profiles the mineralization of 4PCH using (a) 1g/L of γ-Al_2O_3, Cu(5)/γ-Al_2O_3, and Mg(5)/γ-Al_2O_3, (b) 1 g/L of Cu(5)Mg(x)/γ-Al_2O_3, (c) 1 g/L of Cu(x)Mg(5)/γ-Al_2O_3, and (d) 0.5 to 4 g/L of Cu(1)Mg(5)/γ-Al_2O_3. x = 1, 5, and 10 wt%, initial 4PCH concentration = 40 mg/L (TOC_0 = 29 mg/L), bicarbonate ionic strength = 5

mM, inlet gas phase ozone concentration = 23,616 ppmv, and initial pH = 8.5. The TOC profile of the Cu(5)Mg(5)/γ-Al_2O_3 catalyst are shown twice in Figs. (b) and (c) for ease of comparison. 34

Fig. 4.4. Left panel: Surface hydroxyl groups (primary axis) and TOC removal after the initial 50 min of ozonation (secondary axis) of (a) γ-Al_2O_3, Cu(5)/γ-Al_2O_3, and Mg(5)/γ-Al_2O_3, (b) Cu(5)Mg(x)/γ-Al_2O_3, and (c) Cu(x)Mg(5)/γ-Al_2O_3; Right panel: pH_{pzc} (primary axis) and TOC removal at 120 min (secondary axis) of (d) γ-Al_2O_3, Cu(5)/γ-Al_2O_3, and Mg(5)/γ-Al_2O_3, (e) Cu(5)Mg(x)/γ-Al_2O_3, and (f) Cu(x)Mg(5)/γ-Al_2O_3. x = 1, 5, and 10 wt%. 39

Fig. 4.5. XRD analysis of the γ-Al_2O_3 support and the Cu(5)/γ-Al_2O_3, Mg(5)/γ-Al_2O_3, and Cu(1)Mg(5)/γ-Al_2O_3 catalysts (diamond symbols represent the diffraction peaks of γ-Al_2O_3)…………………………………………………………………………41

Fig. 4.6. XPS analysis of the γ-Al_2O_3 support and the Cu(5)/γ-Al_2O_3, Mg(5)/γ-Al_2O_3, and Cu(1)Mg(5)/γ-Al_2O_3 catalysts, (a) wide XPS spectra of (1) γ-Al_2O_3, (2) Cu(5)/γ-Al_2O_3, (3) Mg(5)/γ-Al_2O_3, and Cu(1)Mg(5)/γ-Al_2O_3, (b) XPS Mg 2p spectra, (c) XPS Cu $2p_{3/2}$ spectra, (d) Cu $L_3M_{4.5}M_{4.5}$ spectra, (e) XPS O 1s spectra, and (f) XPS Al 2p spectra……………...43

Fig. 4.7. SEM-EDS analysis of (a) and (b): γ-Al_2O_3, (c) and (d): Cu(5)/γ-Al_2O_3, (e) and (f): Mg(5)/γ-Al_2O_3, and (g) to (i) : Cu(1)Mg(5)/γ-Al_2O_3……………………………..........45

Fig. 4.8. (a) and (b) BF-TEM images of γ-Al_2O_3. HAADF-EDS images of (b) and (c) Cu(5)/γ-Al_2O_3, (d) and (e) Mg(5)/γ-Al_2O_3, and (g) to (i) Cu(1)Mg(5)/γ-Al_2O_3……….......47

Fig. 4.9. NH_3-TPD profiles of γ-Al_2O_3, Cu(5)/γ-Al_2O_3, Mg(5)/ γ-Al_2O_3, and Cu(1)Mg(5)/ γ-Al_2O_3……………………………………………………………………………..50

Fig. 4.10. 4PCH oxidation in the absence and presence of TBA, (a) Normalized 4PCH concentration and (b) liquid ozone concentration profiles of Cu(1)Mg(5)/γ-Al_2O_3. Initial 4PCH concentration = 40 mg/L, bicarbonate ionic strength = 5 mM, inlet gas phase ozone concentration = 23,616 ppmv, catalyst dosage = 2 g/L, initial pH = 8.5, TBA concentration = 2.7 mM…………………………………………………………………………...52

Fig. 4.11. Cu $2p_{3/2}$ photoelectron peaks of the Cu(1)Mg(5)/γ-Al_2O_3 catalyst (1) before and (2) after ozonation of 4PCH………………………………………………………………..56

Fig. 4.12. Reaction routes of 4PCH mineralization by ozonation using Cu(1)Mg(5)/γ-Al_2O_3. (1) Formation of $RO_2^{\bullet}$, (2) formation of $RO^{\bullet}$, (3) transformation of $RO_2^{\bullet}$ to ketone, hydroxyl, and peroxide groups, (4) ring opening by C-C scission of $RO^{\bullet}$, (5) ring opening following cleavage of the pentyl group, (6) H-abstraction of the carboxylic group, (7) chain breaking, and (8) mineralization…………………………...59

Fig. 4.13. Reusability of Cu(1)Mg(5)/γ-Al_2O_3 for 4PCH mineralization over 5 cycles, (a) Normalized TOC profiles, (b) pH profiles, (c) liquid ozone profiles, and (d) FT-IR spectra of the fresh and used Cu(1)Mg(5)/γ-Al_2O_3 catalyst. Initial 4PCH concentration = 40 mg/L (TOC_0 = 29 mg/L), bicarbonate ionic strength = 5 mM, inlet ozone concentration = 23,616 ppmv, catalyst dosage = 2 g/L, and initial pH = 8.5……………………………………….61

Fig. 4.14. Leaching after five reusability cycles of (a) Cu, (b) Mg, and (c) Al. Initial 4PCH concentration = 40 mg/L (TOC_0 = 29 mg/L), bicarbonate ionic strength = 5 mM, inlet ozone concentration = 23,616 ppmv, catalyst dosage = 2 g/L, and initial pH = 8.5……….64

Fig. 4.15. Normalized TOC profiles of the catalytic ozonation of (a) 4PCH, (b) 4MCH, (c) DCHA, (d) ADA, and (e) mixture of 4PCH, 4MCH, DCHA, ADA using Cu(1)Mg(5)/γ-

Al_2O_3. TOC_0 = 29 mg/L, bicarbonate ionic strength = 5 mM, inlet ozone concentration = 23,616 ppmv, catalyst dosage 2 g/L…………………………………………………..66

Fig. 4.16. Regression of -ln(TOC/TOC_0) vs time for the single and catalytic ozonation of (a) 4PCH, (b) 4MCH, (c) DCHA, (d) ADA, (e) mixture of 4PCH, 4MCH, DCHA, ADA using Cu(1)Mg(5)/γ-Al_2O_3. TOC_0 = 29 mg/L, bicarbonate ionic strength = 5 mM, inlet ozone concentration = 23,616 ppmv, catalyst dosage 2 g/L………………………………68

Fig. 4.17. Toxicity analysis of the by-product of 4PCH ozonation by Cu(1)Mg(5)/γ-Al_2O_3...72

Fig. A.1. Calibration curve for TC and IC measurements. ………………………………..95

Fig. B.1. Single ozonation of 4PCH. Initial 4PCH concentration = 40 mg/L (TOC_0 = 29 mg/L), bicarbonate ionic strength = 5 mM, inlet gas phase ozone concentration = 23,616 ppmv, and initial pH = 8.5…………………………………………………………………96

Fig. B.2. Catalytic ozonation of 4PCH using 1 g/L of Cu(1)Mg(5)/γ-Al_2O_3. Initial 4PCH concentration = 40 mg/L (TOC_0 = 29 mg/L), bicarbonate ionic strength = 5 mM, inlet gas phase ozone concentration = 23,616 ppmv, and initial pH = 8.5…………………………..97

Fig. B.3. Catalytic ozonation of 4PCH using 2 g/L of Cu(1)Mg(5)/γ-Al_2O_3. Initial 4PCH concentration = 40 mg/L (TOC_0 = 29 mg/L), bicarbonate ionic strength = 5 mM, inlet gas phase ozone concentration = 23,616 ppmv, and initial pH = 8.5…………………………..98

Fig. C.1. Catalytic ozonation of 4PCH using Cu(1)Mg(5)/γ-Al_2O_3 at different stirring speeds. Initial 4PCH concentration = 40 mg/L (TOC_0 = 29 mg/L), bicarbonate ionic strength = 5 mM, inlet gas phase ozone concentration = 23,616 ppmv, catalyst dosage = 2 g/L and initial pH = 8.5……………………………………………………………100

Fig. C.2. Catalytic ozonation of 4PCH using Cu(1)Mg(5)/γ-Al_2O_3 at different particle sizes. Initial 4PCH concentration = 40 mg/L (TOC_0 = 29 mg/L), bicarbonate ionic strength = 5 mM, inlet gas phase ozone concentration = 23,616 ppmv, catalyst dosage = 2 g/L and initial pH = 8.5…………………………………………………………………………101

List of tables

Table 2.1. Target components of OSPW with operational and environmental concerns....... 5

Table 3.1. Model NA molecules tested in this work. 25

Table 4.1. Characterization of the mono-metallic and bi-metallic catalysts by ICP-OES and BET analyses. 28

Table 4.2. Surface hydroxyl groups and pH_{pzc} of the γ-Al_2O_3 support and catalysts. 36

Table 4.3. Distribution of solid acid sites of the support and the catalysts......................... 50

Table 4.4. Identified by-products of the mineralization of 4PCH through HCO using Cu(1)Mg(5)/γ-Al_2O_3.. 58

Table 4.5. First order kinetic rate constants and electrical energy per order of the single and catalytic mineralization of the different NAs and their mixture by Cu(1)Mg(5)/γ-Al_2O_3. .. 69

Abbreviations

4MCH	Trans-4-methylcyclohexanecarboxylic acid
4PCH	Trans-4-pentylcyclohexanecarboxylic acid
ADA	1,3-adamantanedicarboxylic acid
AOP	Advanced oxidation process
BET	Brunauer-Emmett-Teller
BF	Bright field scanning
CEQG	Canadian environmental quality guidelines
CuO_x	Copper oxides
DCHA	Dicyclohexylacetic acid
DOC	Dissolved organic carbon
EDS	Energy dispersive spectroscopy
FT-IR	Fourier transform infrared spectroscopy
HAADF	High angle annular dark field
HCO	Heterogeneous catalytic ozonation
ICP-OES	Inductively coupled plasma optical emission spectroscopy
M^{n+}	Lower valence state of a metal site on a catalyst

$M^{(n+1)+}$	Higher valence state of a metal site on a catalyst
MS	Mass spectroscopy
MW	Molecular weight
NA	Naphthenic acid
PAHs	Polycyclic aromatic hydrocarbons
p-BQ	Parabenzoquinone
pH_{pzc}	pH point of zero charge
QSAR	Quantitative structure activity relationship
ROS	Reactive oxygen species
SEM	Scanning electron microscopy
TBA	Tert-butyl alcohol
TDS	Total dissolved solids
TEM	Transmission electron microscopy
TOC	Total organic carbon
SEM	Scanning electron microscopy
XPS	X-ray photoelectron spectroscopy
XRD	X-ray diffraction

Nomenclature

ChV	Chronic value index (mg/L)
EC_{50}	Half maximal effective concentration (mg/L)
E_{EO}	Electrical energy per order (kWh/m^3)
k	Kinetic constant for a reaction ($M^{-1}s^{-1}$ or min^{-1})
k_{ow}	Partition coefficient in water-octanol mixtures (unitless)
LC_{50}	Lethal concentration 50 (mg/L)
n	Number of carbon atoms in a naphthenic acid molecule
P	Power input to the ozone generator (kW)
t	time (min or h)
V	Volume of the reactor (m^3)
x	Loading of Cu or Mg in bi-metallic Cu-Mg catalysts (%wt)
X	Number of oxygen atoms in a naphthenic acid molecule
TOC_0	Initial total organic carbon concentration (mg/L)
Z	Hydrogen deficiency of a naphthenic acid molecule

Subscripts

0	Initial
24h	After 24 h

Chapter 1: Introduction

1.1 Research background and motivation

Canada has the third largest oil reserves in the world. Synthetic crude oil is originated in Canada from bitumen, which is entrapped in oil sands. Bitumen extraction by surface mining generates wastewater effluents, known as oil sands process water (OSPW). Most of OSPW is treated and recycled in the bitumen extraction process, but a fraction of it must be disposed of in engineered tailing ponds under the current zero discharge policy imposed in Alberta [1,2]. The water matrix of OSPW is composed of several chemical species with severe environmental concerns. Naphthenic acids (NAs) are among the main target pollutants in OSPW due to their corrosivity and high toxicity to aquatic organisms that may be exposed to the tailing ponds [3,4].

The Government of Canada has recently initiated developing regulations that will allow releasing the treated OSPW to the environment [5]. Wastewater treatment technologies have been tested in the past years to degrade NAs. Throughout the past decade, single ozonation (non-catalytic ozonation) has been studied to remove NAs and has been proven to reduce their toxicity [6]. However, it has limitations in complete oxidation of NAs to CO_2. Heterogeneous catalytic ozonation (HCO) is reported as a more efficient and cost-effective alternative to single ozonation for the mineralization of NAs [7]. Despite its potential, HCO has only been studied after 2019 for complete oxidation of model NA compounds and their mixtures [8–10]. Researchers have shown the potential of metal oxide and carbon-based catalysts to degrade NAs by HCO [8–11]. Their studies have provided preliminary insight into the feasibility of HCO to mineralize NAs and to reduce the toxicity of NA containing wastewaters. Despite the effectiveness of HCO for the removal of NAs, the relationship between the physico-chemical properties of catalysts and their activity in the oxidation of NAs is not thoroughly studied. There is currently a lack of knowledge in how the catalysts' active sites progress the NA oxidation reactions. Furthermore, the mechanism and reaction network of complete oxidation of NAs by HCO, as well as the reusability and economic performance of HCO for the mineralization of NAs are not fully investigated.

Al_2O_3 with high porosity and structural stability has long been used as a catalyst support in liquid and gas phase reactions [12–14]. Building on the previous findings of our research group on the effectiveness of catalysts based on Cu and Mg for the catalytic ozonation of NAs [10], this work aims at formulating a new bi-metallic catalyst by dispersing Cu and Mg on the surface of γ-Al_2O_3 to mineralize a recalcitrant NA model compound, i.e., trans-4-pentylcyclohexanecarboxylic acid (4PCH). This work also elucidates the role of catalysts' active sites and solid acidity of catalysts in the complete oxidation of 4PCH. The reaction network and mechanism of 4PCH mineralization, as well as practical aspects of the formulated bi-metallic catalyst (reusability, metal oxide leaching, oxidation of mixture of NAs, and toxicity of reaction by-products) are also investigated. It is expected that the results of this dissertation contribute to the generation of fundamental and practical knowledge, which can be used for the treatment of OSPW in Canada.

1.2 Structure

Chapter 2 presents a literature review on the OSPW effluents in Canada, the environmental impacts of NAs, and different treatment methods that have been studied in recent years for the removal of NAs form the tailing ponds. The HCO process and its applications in the treatment of NAs are also reviewed in Chapter 2. Chapter 3 presents the experimental methods and analytical techniques used in this work to conduct the proposed research in this thesis. Chapter 4 presents and discusses the results of catalytic ozonation of 4PCH and a mixture of NAs, as well as the characterization of the bi-metallic catalysts. The reaction mechanism and practical aspects of the catalytic ozonation of 4PCH are also presented in Chapter 4. Finally, Chapter 5 includes the conclusions of the present work and presents recommendations for future works.

Chapter 2: Literature review

2.1 Oil sands

2.1.1 Oil sands process water

Discovered bitumen and heavy oil reserves in Canada (170 billion barrels) represent 10% of the total reserves in the world, placing Canada among the top five petroleum producing countries worldwide [15,16]. The majority of bitumen in Alberta is entrapped in oil sands, which consist of around 85% clay and quartz and 15% bitumen and water. Due to the high viscosity (greater than 100,000 cp) and low API degree (less than 10) of bitumen, special recovery methods are used for the extraction of bitumen from oil sands, i.e., surface mining for deposits near the surface and steam assisted gravity drainage for deposits deeper than 75 m. The surface mining process involves crushing oil sands and mixing it with large volumes of alkaline hot water (70-80 ºC) for bitumen extraction [15]. The bitumen is separated from water and sands in the form of froth by injecting air. The separated bitumen is then mixed with diluents and sent for upgrading to synthetic crude oil and further refining. The majority of process water separated from sands and bitumen is recycled for bitumen extraction. Between 1.06 to 4.56 barrels of fresh water are required per barrel of oil equivalent produced by surface mining. This accounts for 20 % of the total water demand of bitumen extraction, while the remaining 80% is supplied by recycling the treated process water. In 2022, a total of 1043 million m^3 of water (6560 million barrels) were used to produce 657 million barrels of oil equivalent [16]. The wet sands are stored in tailing ponds to separate water and sand by gravity [15].

The accumulated water in tailing ponds (OSPW) has a pH between 7.7 and 8.8 with a hardness of 15-25 mg/L Ca^{2+} and 5-10 mg/L Mg^{2+}[3]. OSPW includes inorganic components such as chlorides, bicarbonates, and sulphates, as well as trace metals such as Al, As, Cd, Cr, and Cu. The organic content of tailing ponds consists of volatile organic compounds, polycyclic aromatic hydrocarbons (PAHs), and NAs [3]. Table 2.1 presents a summary prepared by Allen on the components of OSPW with potential operational and environmental concerns. Among the chemicals listed in Table 2.1, ammonia, chloride, sulphates, NAs, and total dissolved solids (TDS) can cause equipment corrosion, which hinders OSPW reusability. PAHs, NAs, TDS, and some trace metals are sources of chronic and acute toxicity. In addition, the presence of hardness and suspended solids are undesired in the bitumen extraction process [4].

Table 2.1. Target components of OSPW with operational and environmental concerns.

Target chemical	**Concentration range in tailing ponds (mg/L)**
Ammonia	~ 3-14
Aromatic hydrocarbons (benzene, phenols, toluene, PAHs)	0.01-5
Bitumen (heavy oil)	25-7500
Chloride	80-720
Hardness	70-112
NAs	50-70
Sulphate	230-290
Suspended solids	Variable with depth; < 1% in surface water
TDS	1900-2200
Trace metals (Cr, Cu, Pb, Ni, Zn)	~ 0.001-3

Reprinted from Allen (2008b) [4]

Canada has long operated under a zero-discharge policy, which mandates the storage of OSPW in tailing ponds in Alberta. The Alberta Energy Regulator report states that the total volume of OSPW in the tailing ponds has increased from 1075×10^6 m^3 in 2014 to 1392×10^6 m^3 in 2022 due to the increase in bitumen extraction from oil sands in recent years [17]. The Government of Canada has recently announced the development of regulations that allow the discharge of treated OSPW to the environment, which can alleviate concerns about the growth of the tailing ponds [18]. Therefore, it is imperative to develop new technologies for the treatment of OSPW before its discharge to nearby water bodies.

2.2 Naphthenic acids and their removal methods from OSPW

Among the different components listed in Table 2.1, NAs have been identified as the major toxic component in OSPW [3]. They are toxic to several organisms, including flora and fauna [19]. Their presence in the growing tailing ponds represents an environmental risk for all organisms that may be exposed to them. The next subsections present an overview of NAs and different methods that have been studied for the removal of NAs from OSPW.

2.2.1 Naphthenic acids

NAs are weak alicyclic, aliphatic, and non-aromatic carboxylic acids. NAs follow the general formula $C_nH_{2n+Z}O_X$, where n is the number of carbon atoms in the molecule, Z is the hydrogen deficiency related to the number of rings in the molecule (Z is equal to negative two times the number of rings), and X is the number of oxygen atoms in the molecule [20].

A generalized structure of monoacidic NAs ($X = 2$) with different number of rings ($-6 > Z > 0$) is shown in Fig. 2.1 [21]. NAs have been reported to be present in OSPW in a concentration range of 20-120 mg/L with a uniform distribution of different molecules having 0 ($Z = 0$) to 4 ($Z = -8$) rings [6,22–24]. Frank et al. found that the toxicity of monoacidic NAs is proportional to their molecular weight (MW) and that the introduction of more carboxylic groups into the structure of NAs reduces their toxicity [25]. The toxicity of several NA molecules has been predicted by using the publicly available ECOSAR software [21].

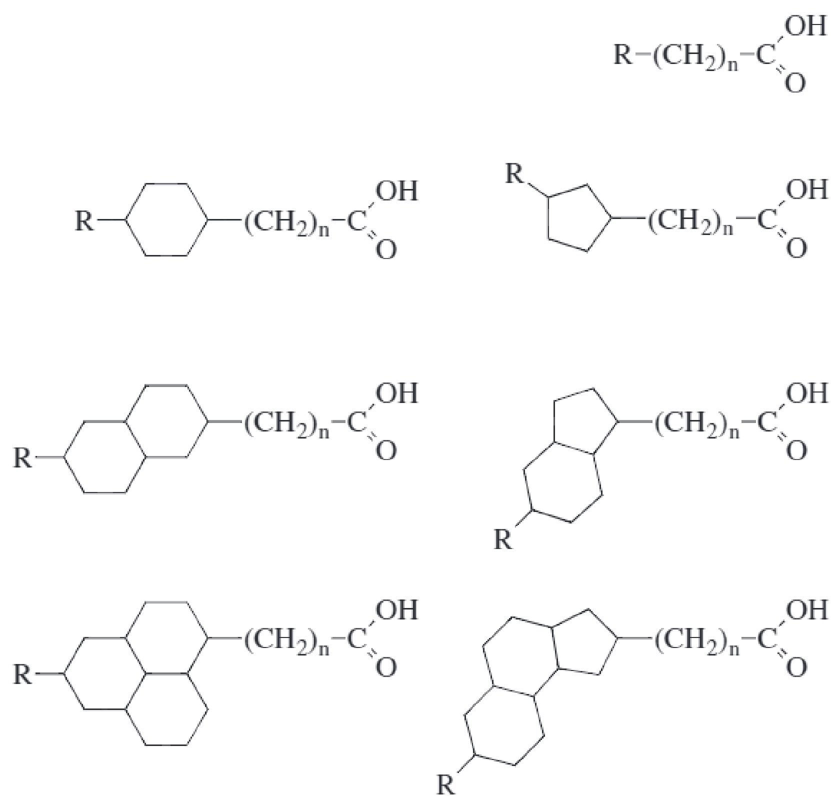

Fig. 2.1. Generalized structure of monoacidic naphthenic acids. R represents aliphatic branching. Reprinted from Quinlan and Tam [21].

2.2.2 Removal methods of naphthenic acids from OSPW

A review paper by Quinlan and Tam (2015) presented several remediation technologies, which were studied to remove NAs from OSPW [21]. They included biodegradation, coagulation/flocculation, membrane filtration, adsorption, and advanced oxidation processes (AOPs). The next subsections present a literature review on physico-chemical methods (coagulation/flocculation, membrane filtration, and adsorption), biological treatment technologies, and AOPs used for the treatment of NAs.

2.2.2.1 Physico-chemical methods

In coagulation/flocculation technologies, a coagulant is used to transform pollutants to suspended particles (also known as flocs), which can be separated from wastewater by settling or flotation [14,15]. Pourrezaei et al. studied the use of two commercial coagulants (alum and polydiallyldimethylammonium chloride) to remove organic compounds from OSPW [15]. They found that NAs with X = 2 were removed by 37%, while NAs with X = 3 were removed by 86%. Furthermore, they reported higher removal of polycyclic NAs, where the concentration of NAs with Z = -2 and -12 was reduced by 55% and 93%, respectively. A patent by Sasaki et al. reported a coagulation/flocculation process using iron oxides followed by magnetic separation, resulting in 91% NAs removal from a simulated OSPW [16]. Coagulation/flocculation techniques are low energy consuming technologies, which are mainly used to remove suspended solids [17]. Nonetheless, the previously mentioned studies prove coagulation/flocculation technologies to be efficient in removing high-MW NAs from OSPW. Therefore, this technology has been reported to be more effective as a pretreatment step to other remediation techniques such as membrane filtration and ozonation [18–20]. Reported disadvantages of coagulation/flocculation processes are the high cost of coagulants and the production of large volumes of sludge, which requires further treatment [17,21].

Membrane filtration separates pollutants by passing wastewater through a porous medium that is only permeable to water [14,20,22]. The efficiency of membranes depends on their pose size with nanomembranes being more effective than micromembranes for the removal of NAs. Alpatova et al. reported that when micromembrane filtration was used after the coagulation/flocculation treatment of OSPW, the membrane was only able to remove 12% of NAs [20]. The low efficiency of the membrane for the removal of NAs was attributed to the large pore size (0.01-0.1 μm) of the membrane, which prevented the rejection of low-MW NAs. In contrast, Peng et al. achieved 95% NAs rejection from previously clarified OSPW samples (TDS removed by settling) using nanomembranes with pore sizes in the range of 0.34-0.81 nm [22]. Motta Cabrera et al. studied the use of titanium nanomembranes (average pore size of 5 nm) to improve recyclability of OSPW in a Canadian oil sands mine and reported a 92% total organic carbon (TOC) rejection [23]. Although the TOC removal was mainly attributed to residual bitumen in OSPW, the NA fraction of TOC was still found to be reduced. Membrane filtration allows the continuous treatment of large volumes of OSPW [14,22]. Furthermore, membrane filtration technologies are effective to treat OSPW to the quality needed for recycling [17]. Membrane fouling is one of the operational obstacles of the membrane filtration method, which could be fixed by backwashing. However, the backwashing water would then need further treatment or storage [3,14,17,20,22,23].

Adsorption technologies can selectively remove dissolved organic pollutants depending on the surface properties of the adsorbents such as surface area, porosity, and functional groups [4,24]. Gamal El-Din et al. showed that the application of a petroleum coke adsorbent resulted in 85% removal of NAs from OSPW [25]. The adsorbent preferentially adsorbed 99% of NAs with five and six rings (Z = -10 and Z = -12). Despite high removal efficiency of the petroleum coke, more research was needed on the regeneration and/or disposal methods of the adsorbent [25]. Da Silva Medeiros et al. studied a sludge-based biochar modified by Sb and Zn to adsorb NAs from OSPW [26]. They reported a maximum NA removal efficiency of 86%, where 100% of NAs with 20 to 22 carbons were removed. Additionally, they reported a three-fold decrease in the toxicity of OSPW. Their adsorbents were saturated and needed regeneration after 24 h. A decrease in the adsorption capacity of the adsorbents was also observed after the fifth regeneration cycle. Adsorbents can preferentially remove high concentrations of high-MW NAs and reduce the toxicity associated with them [24]. Adsorption processes are cost-effective, especially when adsorbents are produced from process wastes, such as petroleum coke or sludge. However, the energy demand associated with the regeneration of adsorbents and the need for the purchase of fresh adsorbents (due to loss of activity after regeneration) could result in high operational costs [14,17,25,26].

2.2.2.2 Biological methods

Biodegradation technologies utilize bacteria, algae, or fungi, which degrade organic pollutants by digesting and metabolizing them [26]. McKenzie et al. studied the application of a continuous bioreactor to remove NAs from OSPW [27]. The bioreactor removed 39%

of NAs over 16 months with a removal rate of 2.32 mg NAs/(L day) for a residence time of 6.7 days. The bioreactor was found not to be effective for the removal of large non-biodegradable NA molecules with 4 to 6 rings. However, it reduced the toxicity of the OSPW by 73% [28]. The remaining toxicity was attributed to the presence of NAs with 14 and 15 carbon atoms and the ones with 1 and 2 rings. More recently, Arslan et al. (2022) tested a fixed-bed biofilter with a bacteria consortium indigenous to tailing ponds, which removed 32.5 % of NAs with $X = 2$ from OSPW in 15 days [29]. However, the removal of NAs with X values from 4 to 6 was insignificant.

In contrast to coagulation/flocculation, micromembrane filtration, and adsorption, biodegradation is highly effective in removing lower-MW NAs. Additionally, it is reported as a cost effective remediation technique [26,30]. The limitations of the biological treatment of OPSW are related to its ineffectiveness to degrade large-MW NAs and the need for high reactor space times (large investment). Furthermore, microorganisms must thrive in the toxic medium of OSPW to degrade NAs [3,31]. Due to these limitations, it has been recommended that biological treatment methods are more efficient when used in combination with other remediation techniques such as AOPs (explained in Section 2.2.2.3) or adsorption [32,33].

2.2.2.3 Advanced oxidation processes

AOPs refer to several technologies that can completely oxidize organic matter to CO_2 by utilizing the high oxidation potential of reactive oxygen species (ROS) such as hydroxyl radicals ($OH^{\bullet}$), superoxide radicals ($O_2^{\bullet-}$), singlet oxygen ($^1O_2$), and sulfate radicals ($SO_4^{\bullet-}$). These ROS are generated by UV, H_2O_2, sonication, ozonation, and ionizing radiation

[21,34–36]. Despite earlier conclusions of Quinlan and Tam that AOPs (such as UV/H_2O_2 and Fenton) were more effective in the degradation of polycyclic NAs and less effective in the degradation of low-MW NAs [21], Abdalrhman et al. reported 90% removal of cyclohexanecarboxylic acid, a single-ringed low-MW NA, using a UV/chlorine combined AOP [21,37]. Similarly, Xu et al. reported an 80% mineralization of cyclohexanecarboxylic acid using a combined sulfate/Fenton process at 80°C [38]. The remaining 20% organic molecules were identified as short-chain carboxylic acids such as acetic, formic, oxalic, and fumaric acid. Kumar et al. reported an 84% removal of dicyclohexylacetic acid (DCHA) by simultaneous utilization of ultrasound and H_2O_2 to enhance the generation of $OH^{\bullet}$ radicals [36]. Using electrochemically activated peroxymonosulfate, Abdelrahman et al. reported 92% removal of NAs from OSPW in 4 h, resulting in 85% TOC removal [39].

AOPs have a high potential to rapidly convert NAs to water and CO_2. They are considered clean technologies that remove a broad range of NAs [40,41]. Nevertheless, the oxidation of NAs through AOPs might lead to the production of toxic and stable by-products if a complete oxidation is not achieved. Furthermore, AOPs are often associated with high operational costs [38,42]. AOPs that involve the activation of ROS through UV, ultrasound, or electrically powered cathode-anode couples have high energy demands [34,37,42], while sulfate based AOPs have high reagent costs [38]. The application of ozone (catalytic and non-catalytic) has also been reported since as early as 2008 as an AOP to remove NAs [43]. More information about the principle and performance of ozone-based technologies are provided separately in the next section.

2.3 Ozonation of naphthenic acids

2.3.1 Ozone molecule

Ozone is a powerful oxidant, which is highly reactive due to its resonance structures and its electron abstracting and donating capabilities [7,44]. More importantly, ozone can undergo a decomposition process in alkaline water, which transforms it into ROS such as hydroxyl radicals, superoxide radicals, and singlet oxygen for effective oxidization of organic pollutants. Eqs. (2.1) to (2.6) show the ozone decomposition process in the absence of a catalyst at alkaline conditions [44–46]. Molecular ozone reacts with water to form $OH^{\bullet}$ and O_2 in Eq. (2.1). Ozone can also react with hydroxide ions (OH^{-}) to form $O_2^{\bullet -}$ and peroxy radicals ($O_2H^{\bullet}$) in Eq. (2.2). Following the initiation reactions, the produced $OH^{\bullet}$ and $O_2H^{\bullet}$ further react with molecular ozone to continue the ozone decomposition through Eqs. (2.3) and (2.4). Eq. (2.5) shows the formation of singlet oxygen through the reaction of hydroxyl and superoxide radicals. The process is terminated with the formation of hydrogen peroxide (H_2O_2) through the recombination of peroxy radicals in Eq. (2.6) [47]. Since the initiation of ozone decomposition involves hydroxide ions, higher pH values result in faster decomposition of ozone and in high concentrations of ROS (singlet oxygen, and hydroxyl and superoxide radicals).

$$O_3 + H_2O \rightarrow 2OH^{\bullet} + O_2 \tag{2.1}$$

$$O_3 + OH^{-} \rightarrow O_2^{\bullet -} + O_2H^{\bullet} \tag{2.2}$$

$$O_3 + OH^{\bullet} \rightarrow O_2 + O_2H^{\bullet} \tag{2.3}$$

$$O_3 + O_2H^{\bullet} \rightarrow 2O_2 + OH^{\bullet} \tag{2.4}$$

$$OH^{\bullet} + O_2^{\bullet-} \rightarrow {}^1O_2 + OH^- \quad (2.5)$$

$$2O_2H^{\bullet} \rightarrow O_2 + H_2O_2 \quad (2.6)$$

The involvement of ROS in the oxidation of a pollutant can be confirmed using quenchers. The quenching method is based on the introduction of a molecule that interrupts the ozone decomposition cycle by scavenging specific ROS [48–50]. For instance, tert-butyl alcohol (TBA) can be introduced into the reaction medium to study the presence of $OH^{\bullet}$ radicals as it reacts slowly with ozone ($k = 2\times10^{-5}$ $M^{-1}s^{-1}$) and rapidly with $OH^{\bullet}$ ($k = 6\times10^{8}$ $M^{-1}s^{-1}$) [51]. If the degradation rate of a pollutant is decreased after the addition of TBA, one can conclude that $OH^{\bullet}$ radicals play a role in the oxidation of the pollutant. Other frequently used quenchers include para-benzoquinone (p-BQ) and sodium azide (NaN_3). p-BQ can be used to quench $OH^{\bullet}$ ($k = 1.2 \times10^{9}$ $M^{-1}s^{-1}$) and $O_2^{\bullet-}$ ($k = 8.3 \times10^{8}$ $M^{-1}s^{-1}$), while NaN_3 may be utilized for reacting with $OH^{\bullet}$ ($k = 1.2 \times10^{9}$ $M^{-1}s^{-1}$) and $^1O_2$ ($k = 2 \times10^{9}$ $M^{-1}s^{-1}$). Given that p-BQ and NaN_3 can quench different ROS, the use of multiple quenchers has been suggested in the literature to assign the contribution of each ROS in the oxidation of pollutants [48,50,52]. For instance, Guo et al. estimated the contribution of $OH^{\bullet}$ and $O_2^{\bullet-}$ in the oxidation of 1,3-dichlorobenzene by ozone by using TBA and p-QB [50]. They first employed TBA to determine the contribution of $OH^{\bullet}$. Afterwards, p-BQ was used to measure the contribution of $O_2^{\bullet-}$ by comparing the removal efficiencies in the presence of TBA and p-BQ [50]. Similarly, NaN_3 has been used after initial tests with TBA to confirm the role of $^1O_2$ in the oxidation of para-hydroxylbenzoic acid [48,50,53].

2.3.2 Single ozonation (non-catalytic ozonation) of NAs

Scott et al. reported that the treatment of an OSPW sample by single ozonation increased its biodegradability and decreased its toxicity [43]. The authors reported a 95% removal of NAs with an insignificant reduction in the TOC of the OSPW, showing that single ozonation was not effective in the mineralization of NAs. [43]. Pérez-Estrada et al. studied the reactivity of two NA model compounds (4PCH and 1,3-adamantanedicarboxylic acid (ADA)) towards ozone. Their findings showed that NA molecules with higher Z value (more rings) were easily oxidized by ozone due to the presence of a higher number of tertiary carbon atoms, which are more reactive towards ROS [54]. Similar findings were reported by Vaiopolou et al., where they studied the removal of a commercial mixture of naphthenic acids by ozonation and found an 85% removal of NAs after 60 min [32]. Linear naphthenic acids ($Z = 0$) such as octanoic acid and 2-ethylhexanoic acid had a conversion of 32 and 37%, while DCHA ($Z = -4$) had a 40% conversion. Kumar et al. tested ozone for the removal of DCHA from a solution [36], where ozonation removed 79% of the molecule at pH 8. It is worth noting that the reports by Pérez-Estrada et al., Vaiopolou et al., and Kumar et al. did not report the complete oxidation of NAs by measuring TOC. Islam et al. found that the oxidation of NAs through ozonation did not correlate to the removal of TOC [55]. For example, only 30% of TOC was reduced when 100% removal of NAs with $X = 2$ was achieved by single ozonation. To address the deficiency of single ozonation for complete mineralization of NAs, HCO has been investigated in recent years, which is discussed in the next section.

2.3.3 Catalytic oxidation of NAs by ozone.

Even though HCO has been extensively investigated to degrade organic pollutants in water and wastewater, it has only been recently studied to oxidize NAs [7,49]. The application of HCO for the mineralization of a petroleum refinery wastewater effluent was studied by Chen et al. in 2017 [11]. The wastewater was collected from the Huizhou refinery (Guangdong, China) and contained a fraction of NAs. They tested a poly-metallic catalyst based on Mn-Fe-Mg-Ce dispersed on pseudoboehmite (65.4 wt% Al_2O_3). They optimized the formulation of the catalyst by varying the loading of the active metals on the support, changing the impregnation sequence of the active metals, and calcining the catalysts at different temperatures. The best catalyst formulation (2.2 wt% MnO, 2.2 wt% Fe_2O_3, 0.9 wt% MgO, 0.9 wt% CeO_2) removed 50.4 % of the TOC associated with the wastewater after 15 min. The authors claimed that the catalyst was able to mineralize NAs with two oxygen atoms ($X = 2$). The TOC removal efficiency of the catalyst was attributed to the high dispersion of Mn, Fe, and Ce after an initial impregnation of the support with Mg and Ce. Surface hydroxyl groups were suggested as the catalyst active sites to convert ozone to $OH^{\bullet}$ radicals for the oxidaiton NAs. No further details were provided on the role of individual metal oxides (Lewis acid sites) in the mineralization of NAs.

The first study of HCO focusing solely on NAs was presented by Al jibouri et al. in 2019 [8]. They focused on an activated carbon catalyst to remove a commercial mixture of NAs. The tested activated carbon removed 85 % of the NA mixture in a third of the time required by single ozonation to reach the same removal extent. It was found that, out of the 85% NA removal, 15% was related to the adsorption of NAs on the surface of activated carbon and 70% was associated with the oxidation of NAs by ozone. The toxicity of the tested mixture was reduced to a minimum of 1.2% (percentage measuring the inhibition of bioluminescence of *Vibrio Fischeri* using a Microtox test) after 45 min. HCO increased the biodegradability of the treated water (measured as the ratio of the biological and chemical oxygen demands) to 0.5, whereas the treated water by single ozonation only had a biodegradability of 0.1. Even though authors highlighted the role of activated carbon for the generation of $OH^{\bullet}$ radicals, they did not provide any insight on the mechanism of the oxidation of NAs by these radicals [8]. Furthermore, the efficiency of the catalyst for complete oxidation (TOC removal) of NAs, as well as the stability and the reusability of the exposed activated carbon to ozone were not reported.

Messele et al. tested a carbon xerogel catalyst to remove the NA model compound ADA [9]. The tested carbon xerogel removed 97% of ADA in 60 min and maintained this removal efficiency (±3%) for three reusability cycles. They observed that the carbon xerogel generated $OH^{\bullet}$ radicals in the liquid phase for the oxidation of ADA. The high removal extent of ADA was attributed to the large surface area and pore volume of the catalyst. A reaction mechanism was proposed for the oxidation of ADA by HCO. The mechanism included the oxidation of ADA in the bulk of the liquid phase, as well as on the surface of the catalyst. Authors did not identify the active sites of the catalyst and did not report the mineralization extent of ADA oxidation.

Babazadeh et al. (a publication from our own research group) recently tested several supported metal oxide catalysts to mineralize trans-4-methylcyclohexanecarboxylic acid (4MCH) in 2023 [10] . Cu was found to be an effective catalyst, especially when supported on MgO. At low loadings of Cu (1 and 5 % wt.), the HCO process removed a maximum of 93% of the TOC of 4MCH in 125 min. Although the Cu/MgO catalyst was highly effective for the mineralization of 4MCH, it had considerable leaching of Cu and Mg at 3.4 and 44 mg/L, respectively. Babazadeh et al. proposed that Mg provided positively charged surface hydroxyl groups that decomposed ozone to ROS, while Cu participated in the mineralization of the reaction by-products by complexation with small carboxylic acid molecules. No direct relationships were established between the observed catalytic activities and physico-chemical properties of the catalyst to elucidate the role of the catalyst's Lewis and Brönsted active sites.

2.3.3.1 Interaction of ozone with catalysts

Chen et al. presented a review paper of metal-oxide catalyst active sites in HCO [56]. They have included surface hydroxyl groups (acting as Brönsted acid sites), oxygen vacant sites, and metal redox couples (Lewis acids and bases). Given their relevance to the present work, the role of surface hydroxyl groups and metal redox pairs as Lewis acid/base sites is further explained in this section.

The mechanism through which surface hydroxyl groups interact with ozone is dependant on their charge, which is determined by the pH of the solution and the pH value of point of zero charge (pH_{pzc}) of the surface of a catalyst. Fig. 2.2 shows the dependency of the charge of surface hydroxyl groups to the solution pH and the catalyst's $pH_{pzc.}$ Surface hydroxyl groups are positively charged when the pH_{pzc} of the catalyst is higher than the pH of the solution. In contrast, surface hydroxyl groups are negatively charged when the pH of the solution is higher than the pH_{pzc} of the catalyst. Surface hydroxyl groups have a neutral charge when the pH is equal to the pH_{pzc} of the catalyst. A common agreement is that a catalyst with a neutral surface charge is more effective for the decomposition of ozone

[51,57]. Ozone can be adsorbed on neutrally charged surface hydroxyl groups by the attachment of its positively and negatively charged ends to oxygen and hydrogen atoms of hydroxyl groups, respectively [58]. This results in the decomposition of ozone to ROS that can completely oxidize organic pollutants.

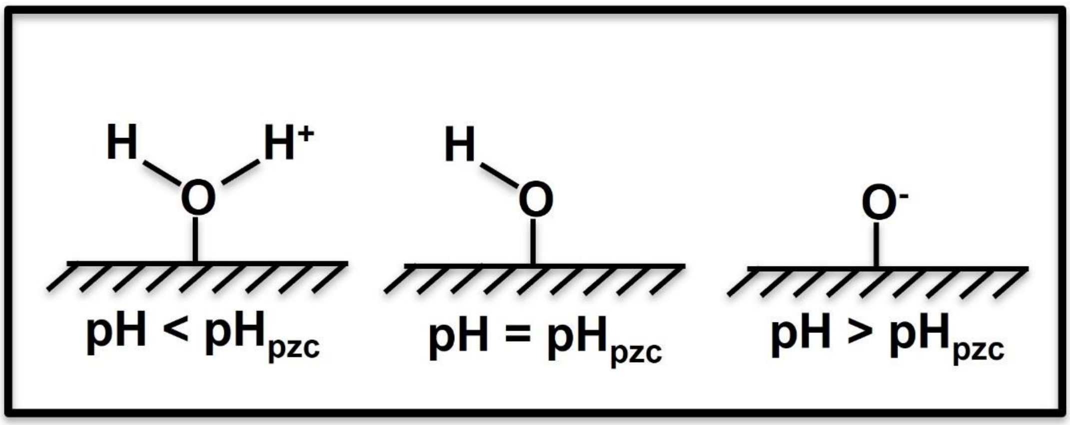

Fig. 2.2. Surface charge dependence of surface hydroxyl groups. Adapted from Chen et al. (2015) [56].

Metal oxides with mixed oxidation states acting as Lewis acid/base sites (e.g., Cu, Fe, and Mn) have also been reported as active sites for ozone decomposition to generate ROS for the oxidation of pollutants [12–14]. Wang and Chen summarized the interaction of ozone with metals having multiple oxidation states through Eqs. (2.7) and (2.8) [49]:

$$M^{n+} + O_3 + H_2O \rightarrow M^{(n+1)+} - OH + OH^{\bullet} + O_2 \quad (2.7)$$

$$M^{(n+1)+} - OH + O_2H^{\bullet} \rightarrow M^{n+} + H_2O + O_2 \quad (2.8)$$

Eq. (2.7) shows how the lower valence state of a metal (M^{n+}) is oxidized to $M^{(n+1)+}$ by ozone, generating $OH^{\bullet}$ in the liquid. Afterwards, the oxidized $M^{(n+1)+}$ is reduced back to M^{n+} by peroxy radicals (Eq. (2.8)), which are originated from ozone decomposition in water (See Eqs. (2.1) to (2.3)) [45,49]. Transition metals (specially copper) have also been proven to form complexes with carboxylates, which can enhance the mineralization extent of the by-products of the oxidation of organic pollutants with ozone [59–61].

2.4 Knowledge gaps and research objectives

As explained in Section 2.3.3, heterogeneous catalysis has been rarely investigated for the complete oxidation of NAs. There is currently not much information available on desired surface properties of catalysts (solid acidity and pH_{pzc}) for the mineralization of NAs. Reaction by-products and the mechanism of catalytic oxidation of NAs by ozone, as well as catalyst stability and reusability are among other topics that are not fully addressed in the literature. Building on the previous findings of our research group on the high activity of Cu/MgO catalysts to mineralize 4MCH, the main objectives of this thesis are to: (1) formulate a bi-metallic catalyst by confining the nano-particles of Cu and Mg in the porous structure of γ-Al_2O_3 to reduce the leaching of Cu and Mg; (2) to study the effect of catalyst surface properties (Lewis and Brönsted acidity and pH_{pzc}) on the mineralization extent of 4PCH; (3) identify reaction by-products of 4PCH oxidation to develop a reaction network for its mineralization by the Cu-Mg/γ-Al_2O_3 catalyst; (4) propose a mechanism for the generation of ROS and oxidation of 4PCH by the Cu-Mg/γ-Al_2O_3 catalyst; and (5) evaluate the TOC removal effectiveness and economics of the Cu-Mg/γ-Al_2O_3 catalyst for the mineralization of 4MCH, ADA, and DCHA, as well as their mixture with 4PCH.

Chapter 3: Experimental

3.1 Catalyst synthesis and characterization

γ-Al_2O_3 (Fisher Scientific, 99.997%) was first crushed and sieved to obtain particles between 105 and 210 µm. Mono-metallic catalysts, CuO_x/γ-Al_2O_3 and MgO/γ-Al_2O_3, with a metal loading of 5 wt% were prepared by the dry impregnation of γ-Al_2O_3 with the nitrate precursors of Cu and Mg, i.e. Cu ($Cu(NO_3)_2.3H_2O$, Fisher Scientific, 99%) and Mg ($Mg(NO_3)_2.6H_2O$, Fisher Scientific, 98%), followed by drying (12 h at 100 ºC) and calcination (5 h at 500 ºC). These catalysts were denoted as Cu(5)/γ-Al_2O_3 and Mg(5)/γ-Al_2O_3. Bi-metallic catalysts, CuO_x-MgO/γ-Al_2O_3, were prepared with an initial dry impregnation of γ-Al_2O_3 with the Mg precursor, followed by drying and a second dry impregnation of the resulting Mg-containing γ-Al_2O_3 with the Cu precursor. The drying and calcination procedure of the bi-metallic catalysts were the same as those of the mono-metallic catalysts. Two sets of bi-metallic catalysts were synthesized by (1) fixing the Cu loading at 5 wt% at three Mg loadings of 1, 5, and 10 wt% and (2) fixing the Mg loading at 5 wt% at three Cu loadings of 1, 5, and 10 wt%. These catalysts were labeled as Cu(x)Mg(5)/γ-Al_2O_3 and Mg(5)Cu(x)/γ-Al_2O_3 with x = 1, 5, and 10 wt%. The final catalysts were crushed and sieved to obtain particle sizes between 105 and 210 µm to be used for the oxidation of 4PCH.

Inductively coupled plasma optical emission spectroscopy (ICP-OES, Varian Agilent Vista Pro Radial, USA) was used to determine the actual loading of the catalysts. Brunauer Emmett Teller (BET) analysis was used to measure the surface area and pore volume of the catalysts using a Micromeritics Gemini VII 2390a (USA). The catalysts were degassed at

200 °C for 2 h before N_2 adsorption. X-ray diffraction (XRD) was used to identify the crystal structure of the catalysts using a PANalytical X'pert Pro multipurpose x-ray diffractometer (Netherlands) with a Cu kα source. Data was collected in a 2θ range of 6-97°. X-ray photoelectron spectroscopy (XPS) was used to determine the oxidation state of the catalysts using a Kratos Axis Ultra Spectrometer (UK) in the range of 0 to 1200 eV. The pass energy for core level spectra was 20 eV, while the survey spectra was obtained at a pass energy of 160 eV. The energy offset of the spectra was calibrated using the C 1s peak at 284.8 eV. Analysis of the XPS data was done using the ESCApe software (Version 1.5). The morphology and surface elemental mapping of the catalysts were studied by scanning electron microscopy (SEM) with energy dispersive spectroscopy (EDS). SEM micrographs were taken using a Hitachi SU-70 microscope (Japan) equipped with EDS mapping. Transmission electron microscopy (TEM) including EDS, bright field scanning (BF), and high angle annular dark field (HAADF) was utilized to visualize the dispersion of CuO_x and MgO particles and to estimate their particle size using a JEOL JEM-ARM200CF S/TEM (Japan) with an accelerating voltage of 200 kV. The solid acidity (Brönsted and Lewis acidity) of the catalysts was quantified by ammonia temperature-programmed desorption (NH_3-TPD) using a Micromeritics AutoChem II 2920 chemisorption system (USA). The samples were first pretreated with He at 400 °C for 2 h and then cooled to 50 °C. Next, NH_3 adsorption was performed at 50 ºC for 1 h at a flow rate of 50 sccm (10.1 mol% NH_3 with balancing He). Desorption was then performed with a heating rate of 15 °C/min up to 900 °C. Fourier transform infra-red (FT-IR) spectroscopy was employed to study the surface of the used catalysts. The spectra were collected using a Tensor 37-Bruker (Germany) with a KBr beam splitter. Transmittance was collected in a wavelength range of

600-4000 cm^{-1}. The pH_{pzc} of the catalysts was measured by the pH drift method [62]. NaCl was added to Erlenmeyer flasks with 50 mL of deionized water. The pH of each flask was adjusted with NaOH (0.1 N) and HCl (0.1 N) to values ranging from 6 to 12. Afterwards, 0.1 g of the catalyst was added to the solution and the pH was measured again after 24 h. The pH_{pzc} was determined as the value where $pH_0 = pH_{24h}$. The amount of surface hydroxyl groups of the catalysts was quantified using the saturated – deprotonation method reported by Yuan et. al. [59]. In a typical analysis, 0.3 g of the catalyst was mixed in a solution of NaOH (0.05 M) and stirred for 24 h. The resulting solution was filtered and titrated using HCl (5.4 mM) and the residual NaOH concentration was calculated. The amount of surface hydroxyl groups was equal to double the amount of NaOH divided by the grams of the catalysts. Mass spectroscopy (MS) was used to measure the concentration of 4PCH and to identify the by-products of its catalytic oxidation by ozone. The MS spectra were collected using a Bruker amaZon X Ion Trap (Germany) with an m/z range of 50 to 240. Negative electrospray ionization was used in enhanced resolution mode of the MS (0.30 u). MS samples were prepared by diluting 10 times with methanol (Fisher Scientific, 99.9%).

3.2 Model naphthenic acid molecules

The catalytic ozonation of four recalcitrant low-MW NA model compounds and their mixture are studied in this work. The model compounds include 4PCH (Fisher Scientific, >99%), 4MCH (Fisher Scientific, >98%), DCHA (Sigma Aldrich, 99%), and ADA (Fisher Scientific, >97%) with limited number of rings between 1 and 3. The molecular structures of the NA model compounds are presented in Table 3.1. 4PCH was selected since it was one of the most difficult NA molecules to be completely oxidized by ozone [54]. 4MCH was chosen to compare the performance of the bi-metallic catalyst in this work to the performance of Cu/MgO in our previously published work [10]. DCHA and ADA were selected as model NA molecules with two-ringed (Z = -4) and three-ringed (Z = -6) structures.

Table 3.1. Model NA molecules tested in this work.

ID	Name	MW (g/mol)	Molecular structure
4PCH	trans-4-pentylcyclohexanecarboxylic acid	198	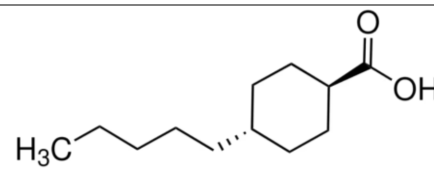
4MCH	trans-4-methylcyclohexanecarboxylic acid	142	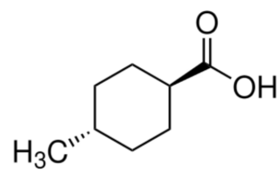
DCHA	dicyclohexylacetic acid	224	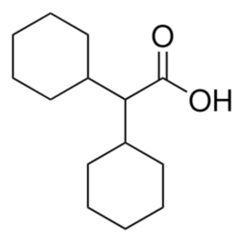
ADA	1,3-adamantanedicarboxylic acid	224	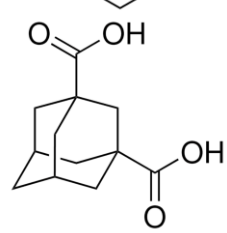

3.3 Single (non-catalytic) and catalytic ozonation experiments

The experimental set-up used for the single and catalytic ozonation experiments is shown in Fig. 3.1 [10]. A 2.2 L semi-batch reactor was first filled with deionized water, the NA model compounds or their mixture, and the sodium bicarbonate buffer ($NaHCO_3$, Sigma Aldrich, 99.7%). The initial TOC concentration (TOC_0) in all experiments was 29 mg/L. The catalyst was then added to the reactor and the initial pH of the solution was adjusted to 8.5 (i.e., the pH of the OSPW) with HCl (0.1 N) and NaOH (0.1 N). The pH adjustment was necessary since the stock solutions of the NA model compounds were prepared in NaOH (pH = 12). After the pH adjustment, ozone was continuously bubbled into the reactor for 120 min. The reactor was maintained under constant stirring (600 rpm). The inlet gas phase ozone flow rate and concentration to the reactor were 600 mL/min and 23,616 ppmv, respectively, in all experiments. All experiments were performed at room temperature. Samples with a volume of 15 mL were extracted every 10 min and quenched with 0.5 mL of $Na_2S_2O_3$ (0.1 M). The samples were filtered with a 0.22 µm nylon syringe filter (Choice^{TM}) to analyze their TOC with a Shimadzu TOC-LCSH/CSN analyzer in the range of 0 – 40 mg/L (Japan). TOC was measured by subtracting the inorganic carbon (IC) of the $NaHCO_3$ buffer from the total carbon (TC) content of the samples (See calibration curve in Appendix A). The pH and ozone concentration in water were continuously measured throughout the 120 min of reaction with an Orion Star A211 pH meter (Canada) and an MS 08 AMT GmbH ozone analyzer (Germany), respectively. The data was recorded using LabView (Version 20.0.1). Selected experiments were repeated three times with a maximum standard deviation of ± 3% in terms of TOC/TOC_0 as shown in Appendix B.

Appendix C shows that no mass transfer limitations were present during the ozonation experiments.

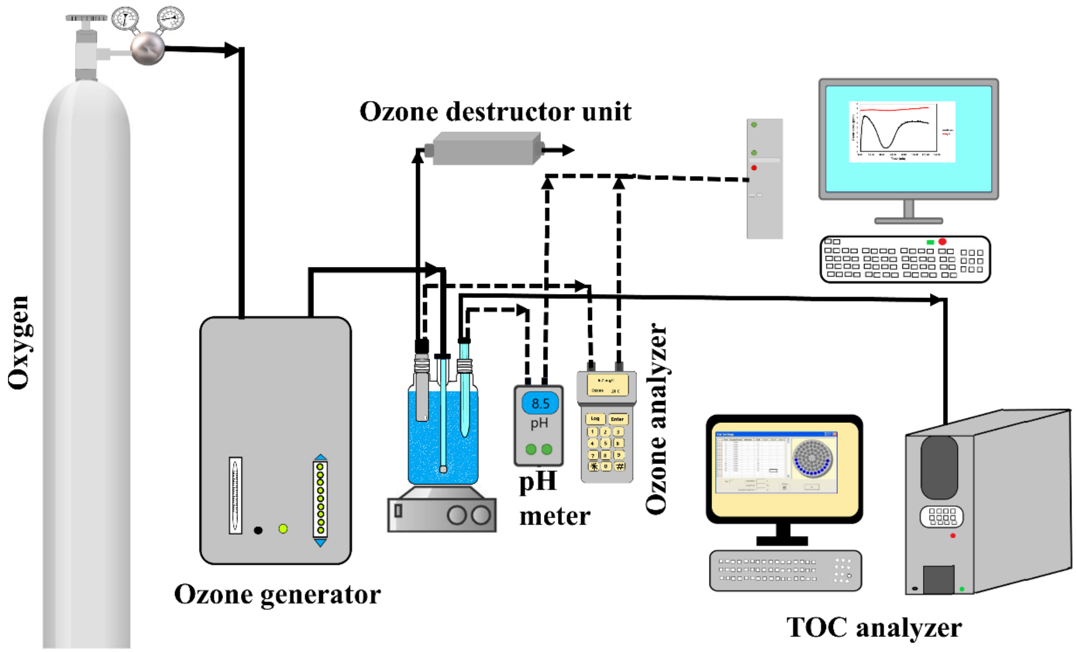

Fig. 3.1. Schematic of the experimental set-up. Reprinted from Babazadeh et al. [10].

Chapter 4: Results and discussions

4.1 Optimization of the composition and dosage of Cu-Mg/γ-Al_2O_3 catalyst

4PCH was selected as the NA model compound to find the best loadings of Cu and Mg that resulted in the highest TOC removal of the bi-metallic catalysts, i.e., Cu(x)Mg(5)/γ-Al_2O_3 and Cu(5)Mg(x)/γ-Al_2O_3 (x = 1, 5, and 10 wt%). A catalyst dosage of 1 g/L was used. The BET surface area and pore volume, as well as the ICP-OES measurements of the mono- and bi-metallic catalysts are reported in Table 4.1. ICP-OES confirmed that the actual loading of the catalysts was close to their nominal loading. Additionally, a consistent decrease of surface area and pore volume was found with the increase of Cu or Mg loadings on γ-Al_2O_3. The decrease in surface area and pore volume suggested that Cu and Mg particles were formed either inside the porous structure of γ-Al_2O_3 or outside the pores, resulting in partial pore blocking.

Table 4.1. Characterization of the mono-metallic and bi-metallic catalysts by ICP-OES and BET analyses.

Catalyst	Cu content (% wt.)	Mg content (% wt.)	BET surface area (m^2/g)	Pore volume (cm^3/g)
γ-Al_2O_3	-	-	224.0	0.76
Cu(5)/γ-Al_2O_3	4.56	0.00	200.6	0.68
Mg(5)/γ-Al_2O_3	0.00	4.40	200.0	0.69
Cu(1)Mg(5)/γ-Al_2O_3	0.96	4.84	191.5	0.67
Cu(5)Mg(5)/γ-Al_2O_3	5.50	4.64	187.6	0.63
Cu(10)Mg(5)/γ-Al_2O_3	9.12	4.63	167.3	0.56
Cu(5)Mg(1)/γ-Al_2O_3	4.71	0.81	200.9	0.71
Cu(5)Mg(10)/γ-Al_2O_3	5.69	9.21	169.0	0.58

The normalized TOC profiles of the ozonation experiments with mono- and bi-metallic catalysts are shown in Figs. 4.1(a-c) to determine the best loadings of the Cu and Mg. Once the optimum loadings were identified, the effect of catalyst dosage (0.5 to 4 g/L) was studied on the TOC removal of the catalyst with the optimized loadings. The normalized TOC profiles of the selected catalyst at different dosages are shown in Fig. 4.1(d). Fig. 4.1(a) shows the mineralization of 4PCH by single and catalytic ozonation with γ-Al_2O_3 and the mono-metallic Cu(5)/γ-Al_2O_3 and Mg(5)/γ-Al_2O_3 catalysts. Single ozonation of 4PCH resulted in an 80% TOC removal after 120 min, while the catalytic ozonation of 4PCH with γ-Al_2O_3 resulted in a 63% TOC removal. Cu(5)/γ-Al_2O_3 showed a very similar normalized TOC profile to that of the single ozonation. However, a slight improvement in the final stages of the reaction was observed, resulting in an 85 % TOC removal after 120 min. Mg(5)/γ-Al_2O_3 showed a TOC removal of 77% after 120 min, which was statistically the same as that of the single ozonation (difference within experimental error). Fig. 4.1(b) shows the results of the complete oxidation of 4PCH with the bi-metallic Cu(5)Mg(x)/γ-Al_2O_3 catalysts (x = 1, 5, and 10 wt%). The TOC removal of Cu(5)Mg(1)/γ-Al_2O_3 (Fig. 4.1(b)) showed no significant difference when compared to that of Cu(5)/γ-Al_2O_3 in Fig. 4.1(a). Cu(5)Mg(5)/γ-Al_2O_3 had a steeper normalized TOC profile in Fig. 4.1(b) than that of Cu(5)/γ-Al_2O_3 in Fig. 4.1(a) with a final TOC removal of 89%. Further increase of Mg loading to 10 wt% in Cu(5)Mg(10)/γ-Al_2O_3 resulted in a TOC removal of 83%, which was similar to that of the single ozonation experiment. Fig. 4.1(c) shows the results obtained for the Cu(x)Mg(5)/γ-Al_2O_3 bi-metallic catalysts (x = 1, 5, and 10 wt%). All the Cu(x)Mg(5)/γ-Al_2O_3 catalysts showed an increase in the final TOC removal in comparison to that of the single ozonation. The normalized TOC profiles of the Cu(x)Mg(5)/γ-Al_2O_3 catalysts were very close to each other. Cu(1)Mg(5)/γ-Al_2O_3 and Cu(5)Mg(5)/γ-Al_2O_3 showed an 89%

TOC removal after 120 min. Cu(10)Mg(5)/γ-Al_2O_3 showed an 86% TOC removal, which was statistically the same as the Cu(x)Mg(5)/γ-Al_2O_3 catalysts with x = 1 and 5 wt%. Cu(1)Mg(5)/γ-Al_2O_3 was selected as the most promising catalyst because of its high TOC removal and lower amount of copper. This catalyst was further studied to optimize its dosage as shown in Fig. 4.1(d). A direct relationship was observed between the dosage of Cu(1)Mg(5)/γ-Al_2O_3 and the mineralization extent of 4PCH up to 2 g/L. Increasing the dosage from 2 to 4 g/L did not change the normalized TOC profile of the catalysts. This suggested that a sufficient amount of catalyst was present in the reaction medium at a catalyst dosage of 2 g/L to interact with dissolved ozone and organic molecules. A further increase of the dosage to 4 g/L likely resulted in the futile decomposition of ozone with no positive effect on TOC removal. Therefore, 2 g/L was chosen as the optimum dosage of Cu(1)Mg(5)/γ-Al_2O_3 and was used in experiments conducted in Sections 4.2 to 4.5.

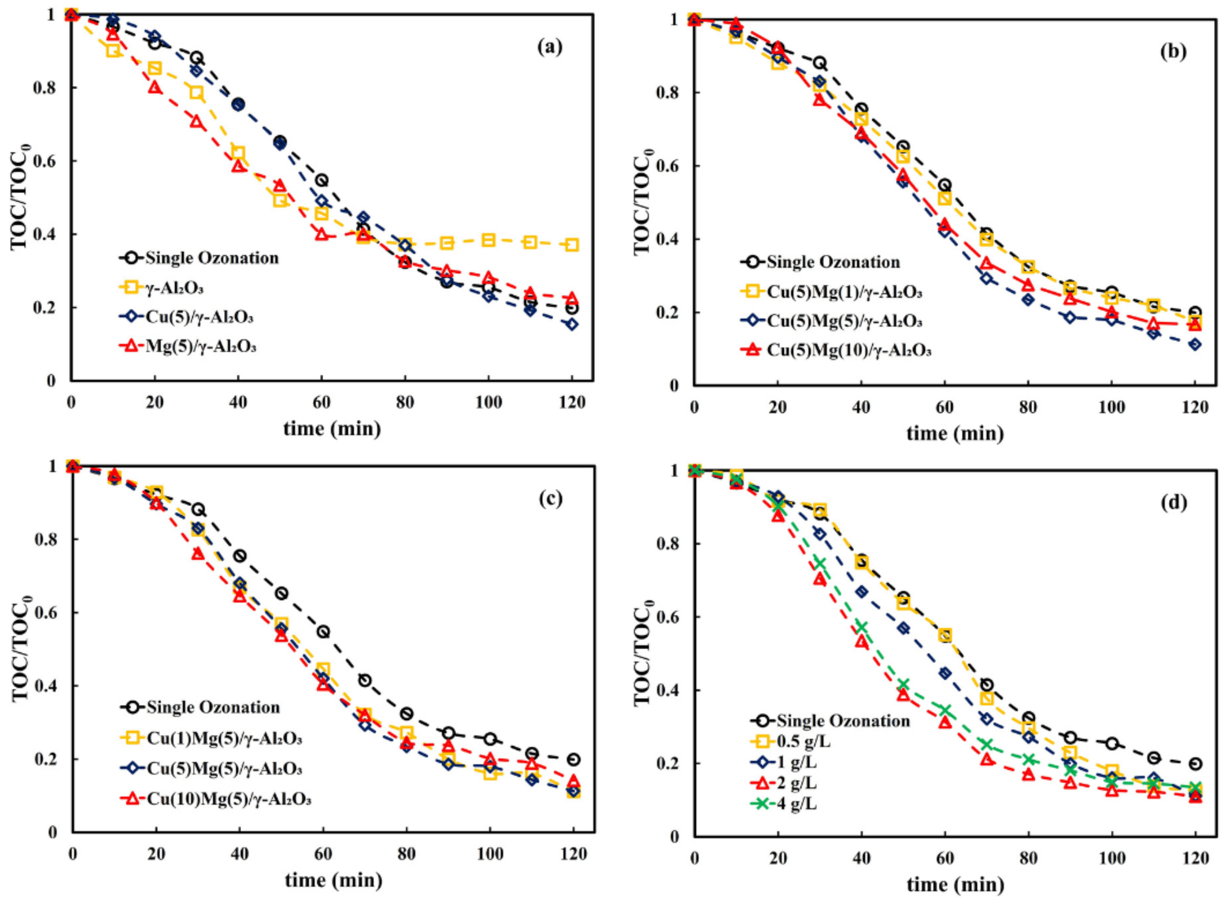

Fig. 4.1. Normalized TOC profiles of the mineralization of 4PCH using (a) 1g/L of γ-Al_2O_3, Cu(5)/γ-Al_2O_3, and Mg(5)/γ-Al_2O_3, (b) 1 g/L of Cu(5)Mg(x)/γ-Al_2O_3, (c) 1 g/L of Cu(x)Mg(5)/γ-Al_2O_3, and (d) 0.5 to 4 g/L of Cu(1)Mg(5)/γ-Al_2O_3. X = 1, 5, and 10 wt%, initial 4PCH concentration = 40 mg/L (TOC_0 = 29 mg/L), bicarbonate ionic strength = 5 mM, inlet gas phase ozone concentration = 23,616 ppmv, and initial pH = 8.5. The TOC profile of Cu(5)Mg(5)/γ-Al_2O_3 is shown twice in Figs. (b) and (c) for ease of comparison.

The pH and liquid ozone concentration profiles associated with Fig. 4.1 are shown in Figs. 4.2 and 4.3, respectively. The pH profiles show that the pH dropped slightly during the first 60 min of the reaction, which was likely due to the production of acidic by-products during the reaction. Afterwards, the pH returned to the initial value of 8.5. Overall, the pH of the solution was fairly constant at the target value of 8.5 during the 120 min of the reaction. The liquid ozone concentration profiles show a general decreasing trend during the first 40-60 min of the reaction due to the production of ROS by ozone decomposition. This was followed by a general increasing trend towards the end of the reaction because of lower ozone consumption and its dissolution in the liquid phase.

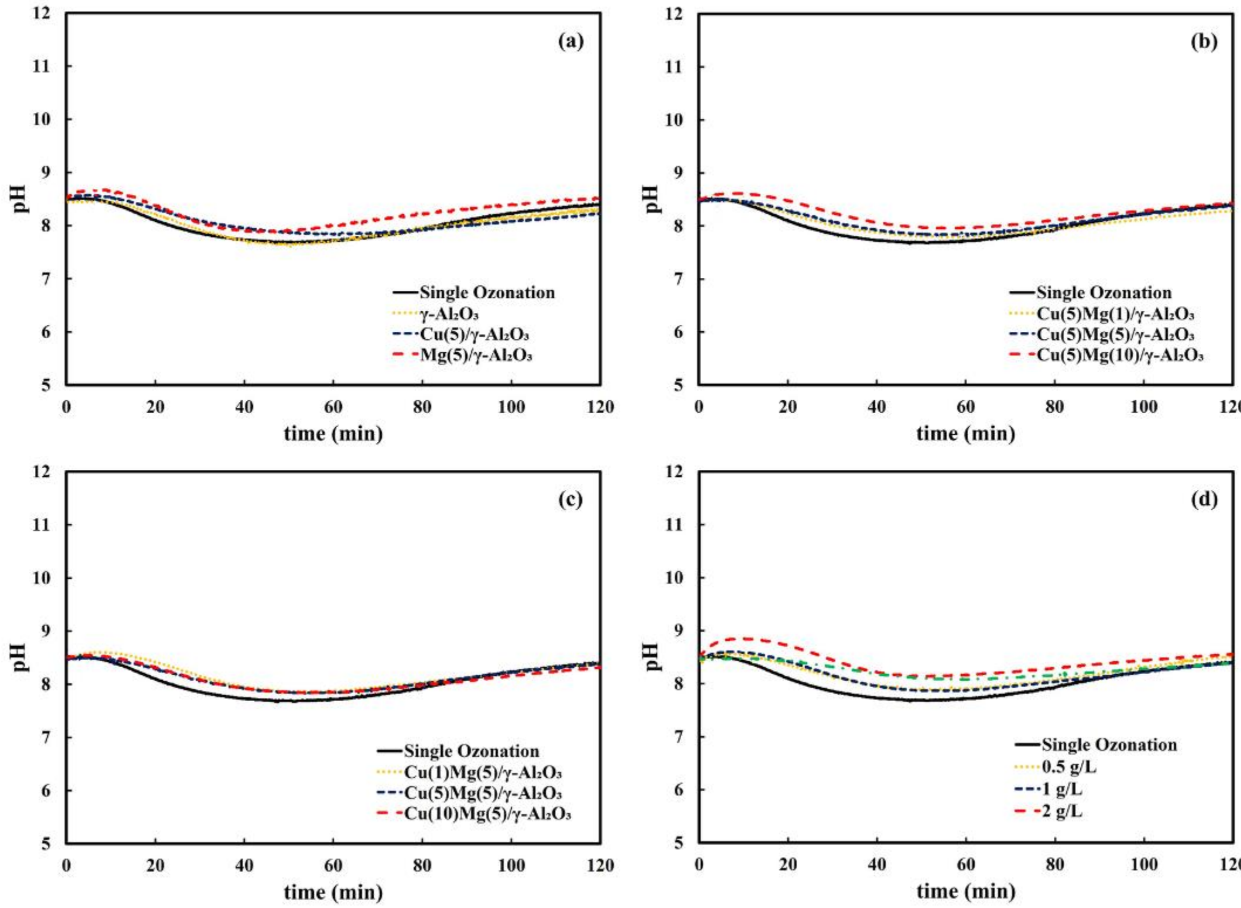

Fig. 4.2. pH profiles the mineralization of 4PCH using (a) 1g/L of γ-Al_2O_3, Cu(5)/γ-Al_2O_3, and Mg(5)/γ-Al_2O_3, (b) 1 g/L of Cu(5)Mg(x)/γ-Al_2O_3, (c) 1 g/L of Cu(x)Mg(5)/γ-Al_2O_3, and (d) 0.5 to 4 g/L of Cu(1)Mg(5)/γ-Al_2O_3. x = 1, 5, and 10 wt%, initial 4PCH concentration = 40 mg/L (TOC_0 = 29 mg/L), bicarbonate ionic strength = 5 mM, inlet gas phase ozone concentration = 23,616 ppmv, and initial pH = 8.5. The TOC profile of the Cu(5)Mg(5)/γ-Al_2O_3 catalyst are shown twice in Figs (b) and (c) for ease of comparison.

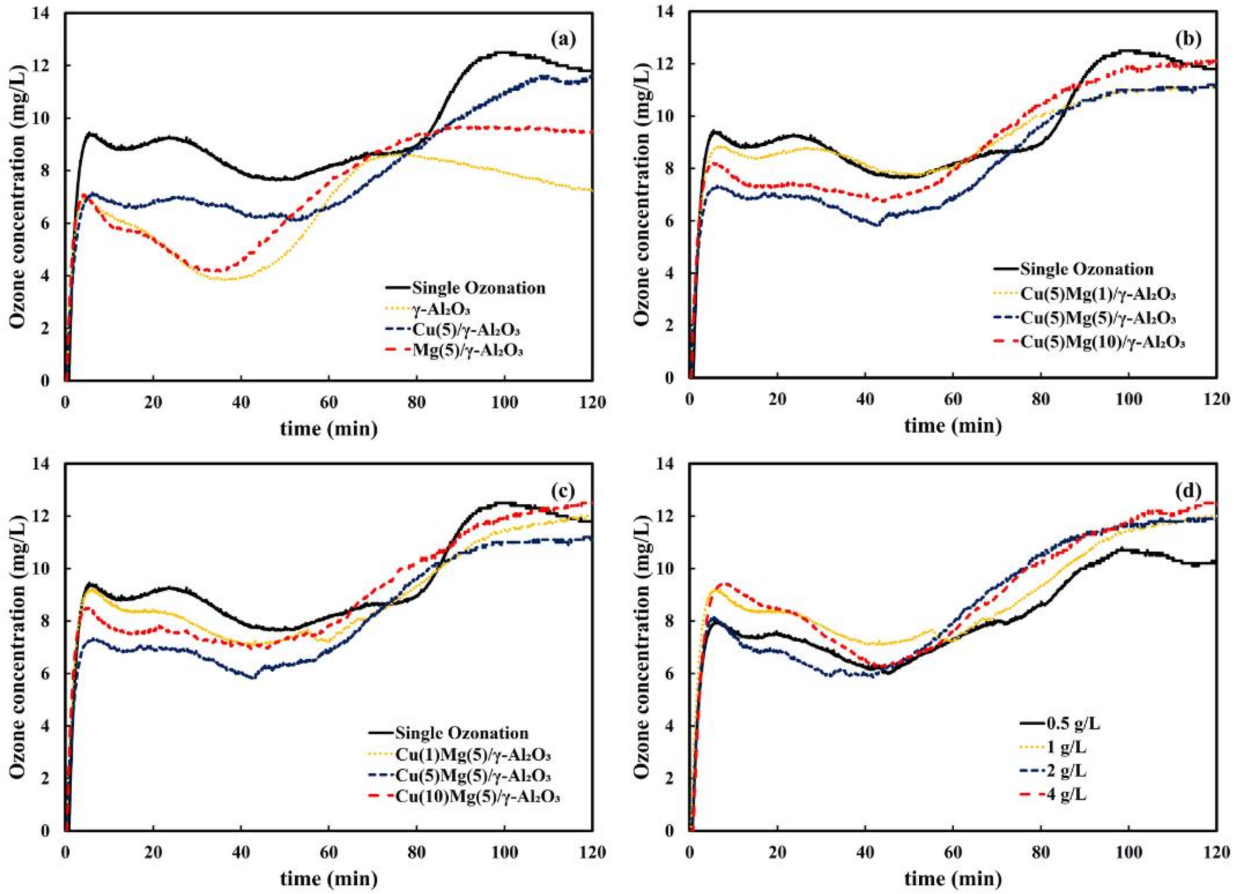

Fig. 4.3. Liquid ozone concentration profiles the mineralization of 4PCH using (a) 1g/L of γ-Al_2O_3, Cu(5)/γ-Al_2O_3, and Mg(5)/γ-Al_2O_3, (b) 1 g/L of Cu(5)Mg(x)/γ-Al_2O_3, (c) 1 g/L of Cu(x)Mg(5)/γ-Al_2O_3, and (d) 0.5 to 4 g/L of Cu(1)Mg(5)/γ-Al_2O_3. x = 1, 5, and 10 wt%, initial 4PCH concentration = 40 mg/L (TOC_0 = 29 mg/L), bicarbonate ionic strength = 5 mM, inlet gas phase ozone concentration = 23,616 ppmv, and initial pH = 8.5. The TOC profile of the Cu(5)Mg(5)/γ-Al_2O_3 catalyst are shown twice in Figs. (b) and (c) for ease of comparison.

To provide an insight into the TOC removal trends observed in Fig. 4.1, the amount of surface hydroxyl groups and pH_{pzc} of all tested catalysts were determined. The results are summarized in Table 4.2. Mg(5)/γ-Al_2O_3 and γ-Al_2O_3 had the highest amount of surface hydroxyl groups at 0.74 and 0.71 mmol/g, respectively, which were close to the values reported in the literature for γ-Al_2O_3 [63]. The addition of Cu to γ-Al_2O_3 decreased the amount of surface hydroxyl groups to 0.44 mmol/g in Cu(5)/γ-Al_2O_3. This was likely because of the attachment of Cu to the surface of γ-Al_2O_3 by removing a hydrogen atom from surface OH groups and binding with the remaining oxygen atom, leading to the formation of Cu_2O [64–66]. The amount of surface hydroxyl groups of the bi-metallic catalysts was mainly between 0.57 and 0.59 mmol/g. The only exception was Cu(5)Mg(1)/γ-Al_2O_3 with a surface hydroxyl group amount of 0.43 mmol/g, which was close to that of Cu(5)/γ-Al_2O_3 (0.44 mmol/g). The γ-Al_2O_3 support had the lowest pH_{pzc} at 6.98 followed by Cu(5)/γ-Al_2O_3 at 7.15. The addition of Mg to γ-Al_2O_3 significantly increased the pH_{pzc} of the support to 8.42. All the bi-metallic Cu(5)Mg(x)/γ-Al_2O_3 and Cu(x)Mg(5)/γ-Al_2O_3 catalysts had a pH_{pzc} between 8.45 and 8.65. The only exceptions were Cu(10)Mg(5)/γ-Al_2O_3 and Cu(5)Mg(1)/γ-Al_2O_3 with pH_{pzc} of 8.08 and 7.25, respectively. This could be related to the coverage of Mg particles by Cu at high Cu to Mg loading ratios of 10 to 5 and 5 to 1 since the impregnation of Cu was done after the impregnation of Mg [67,68].

Table 4.2. Surface hydroxyl groups and pH_{pzc} of the γ-Al_2O_3 support and catalysts.

Catalyst	Surface hydroxyl groups (mmol/g)	pH_{pzc}
γ-Al_2O_3	0.71	6.98
Cu(5)/γ-Al_2O_3	0.44	7.15
Mg(5)/γ-Al_2O_3	0.74	8.42
Cu(5)Mg(1)/γ-Al_2O_3	0.43	7.25
Cu(5)Mg(5)/γ-Al_2O_3	0.58	8.52
Cu(5)Mg(10)/γ-Al_2O_3	0.57	8.65
Cu(1)Mg(5)/γ-Al_2O_3	0.57	8.45
Cu(10)Mg(5)/γ-Al_2O_3	0.59	8.08

Figs. 4.4(a-c) present the dependency of the TOC removal of the catalysts tested in Figs. 4.1(a-c) to the amount of surface hydroxyl groups after the first 50 min of the oxidation of 4PCH. On the other hand, Figs. 4.4(d-f) show the dependency of the TOC removal of the tested catalysts to their pH_{pzc} after 120 min of the reaction. As seen in Fig. 4.4(a), the high amount of the surface hydroxyl groups of Mg(5)/γ-Al_2O_3 and γ-Al_2O_3 correlated to their high TOC removal extent (around 47%) after the first 50 min of the reaction. The TOC removal of Cu(5)/γ-Al_2O_3 in Fig. 4.4(a) was lower than those of Mg(5)/γ-Al_2O_3 and γ-Al_2O_3 due to its lower amount of surface hydroxyl groups. The liquid ozone concentration profiles reported in Fig. 4.3(a) also followed the same trends as those observed for the TOC removal of the catalysts in Fig. 4.4(a). Mg(5)/γ-Al_2O_3 and γ-Al_2O_3 showed higher rates of ozone decomposition (lower ozone concentrations) during the first 50 min of the reaction in comparison to that of Cu(5)/γ-Al_2O_3 (Fig. 4.3(a)). In fact, a U-shape was observed in the liquid ozone concentration profiles of Mg(5)/γ-Al_2O_3 and γ-Al_2O_3 due to faster decomposition of ozone to ROS by the high amount of surface hydroxyl groups of Mg(5)/γ-Al_2O_3 and γ-Al_2O_3 at 0.74 and 0.71 mmol/g, respectively [10,51,69]. On the other hand, the ozone profile of Cu(5)/γ-Al_2O_3 was mainly flat during the first 50 min of the reaction (Fig.

4.3(a)) due to its lower amount of surface hydroxyl groups at 0.44 mmol/g. One could suggest that the higher amount of surface hydroxyl groups of Mg(5)/γ-Al_2O_3 and γ-Al_2O_3 lead to fast decomposition of ozone to ROS, which resulted in the higher TOC removal of these two catalysts during the first 50 min of the reaction when compared to that of Cu(5)/γ-Al_2O_3 as shown in Fig. 4.4(a). The same dependency was also observed between the amount of surface hydroxyl groups and the TOC removal extent of the bi-metallic catalysts after the first 50 min of the reaction as shown in Figs. 4.4(b-c). As seen in Figs. 4.3(b-c), copper-containing bi-metallic catalysts also did not show a U-shape liquid ozone concentration profiles within the first 50 min of the reaction because of their lower surface hydroxyl groups amount between 0.43 and 0.59 mmol/g. In comparison to all the bi-metallic catalysts in Figs. 4.4(a-c), Mg(5)/γ-Al_2O_3 and γ-Al_2O_3 had higher TOC removal after the first 50 min of the reaction because they had higher amount of surface hydroxyl groups.

Despite the similarity in the TOC removal of Mg(5)/γ-Al_2O_3 and γ-Al_2O_3 after the first 50 min of the reaction in Fig. 4.4(a), they had a very different final TOC removal after 120 min in Fig. 4.4(d). This difference could be attributed to the difference in their pH_{pzc} as summarized in Table 4.2. At the solution pH = 8.5, the surface of γ-Al_2O_3 was negatively charged (solution pH > pH_{pzc}), which only resulted in a final TOC removal of only 63% after 120 min. On the other hand, the surface of Mg(5)/γ-Al_2O_3 was neutrally charged (solution pH ≈ pH_{pzc}), which favoured further reduction of TOC to 77% after 120 min. The higher TOC removal of Mg(5)/γ-Al_2O_3 was related to the capability of ozone to electrophilically and nucleophilically attack the O and H atoms of neutrally charged surface hydroxyl groups to accelerate the formation of ROS for complete oxidation of the reaction by-products in the bulk of the liquid phase during the final stages of the reaction (between 50 and 120 min) [56,69–72]. The effect of pH_{pzc} on the final TOC removal of Mg(5)/γ-Al_2O_3 was in accordance with the findings of Psaltou et al., where they reported catalysts with neutrally charged surface were more effective for the oxidation of para-chlorobenzoic acid by ozone [51]. Similar to γ-Al_2O_3, Cu(5)/γ-Al_2O_3 had a negatively charged surface (solution pH > pH_{pzc}). However, Cu(5)/γ-Al_2O_3 had a final TOC removal of 85%, which was higher than those of γ-Al_2O_3 and Mg(5)/γ-Al_2O_3 after 120 min. This showed that in addition to the pH_{pzc}, the presence of Cu was another influential factor to enhance the final TOC removal of the catalysts. As will be explained in Section 4.3, Cu was capable of adsorption of small carboxylic acid by-products of the reaction, which enhanced their complete oxidation to CO_2 on the catalyst's surfaces. As seen in Figs. 4.4 (e) and (f), the bi-metallic Cu(5)Mg(5)/γ-Al_2O_3, Cu(5)Mg(10)/γ-Al_2O_3, and Cu(1)Mg(5)/γ-Al_2O_3 catalysts with neutral surface charge (solution pH ≈ pH_{pzc}) had higher final TOC removals after 120 min than those of Cu(5)Mg(1)/γ-Al_2O_3 and Cu(10)Mg(5)/γ-Al_2O_3 with negative surface charge (solution pH > pH_{pzc}). Overall, the results reported in Fig. 4.4 and Table 4.2 suggested that a sufficiently high amount of surface hydroxyl groups was beneficial to produce more ROS to accelerate the initial oxidation rate of 4PCH in the bulk of the liquid phase, while a neutrally charge catalyst surface along with the presence of copper enhanced the final TOC removal by complete oxidation of recalcitrant by-products [58,69].

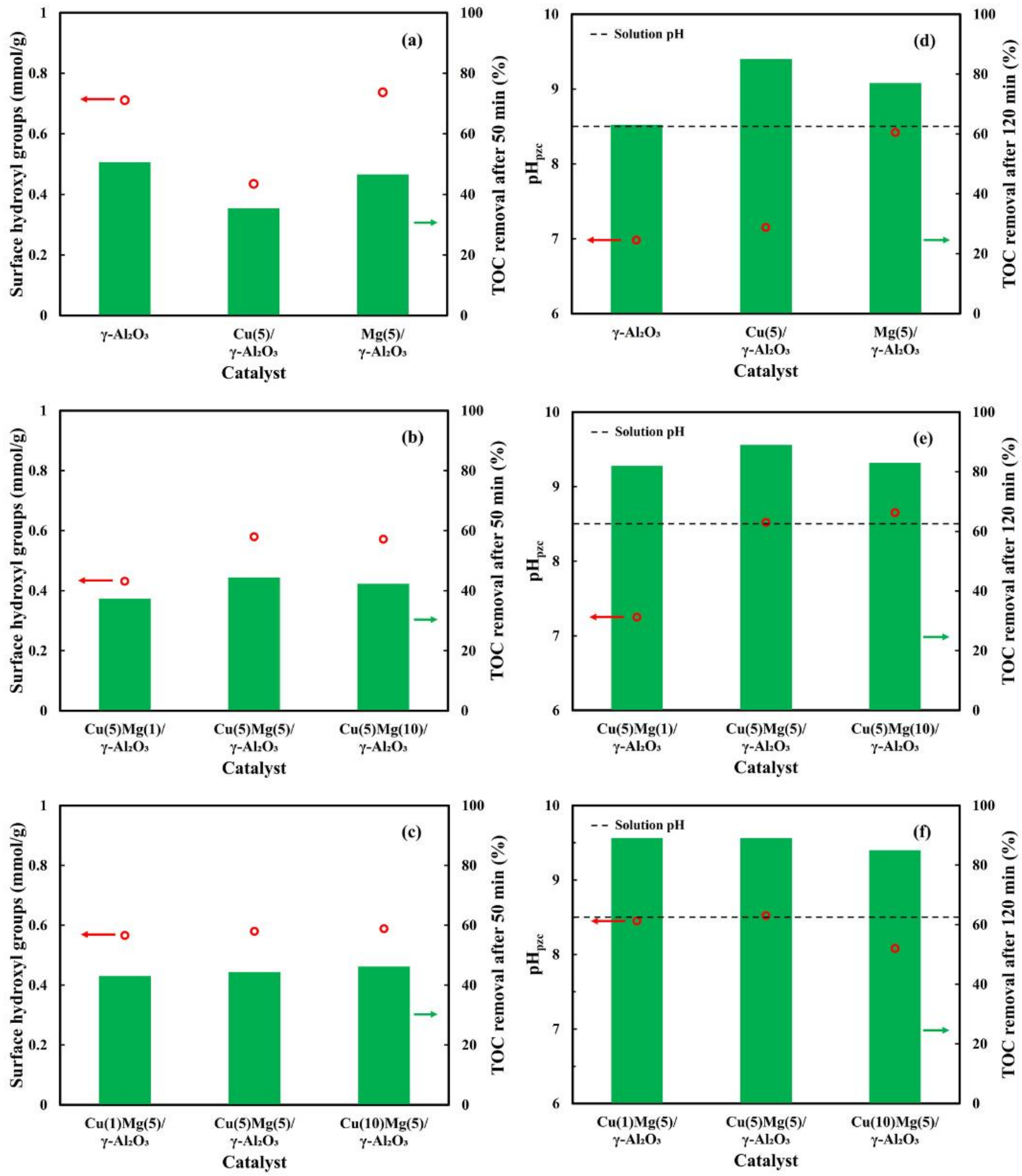

Fig. 4.4. Left panel: Surface hydroxyl groups (primary axis) and TOC removal after the initial 50 min of ozonation (secondary axis) of (a) γ-Al_2O_3, Cu(5)/γ-Al_2O_3, and Mg(5)/γ-Al_2O_3, (b) Cu(5)Mg(x)/γ-Al_2O_3, and (c) Cu(x)Mg(5)/γ-Al_2O_3; Right panel: pH_{pzc} (primary axis) and TOC removal at 120 min (secondary axis) of (d) γ-Al_2O_3, Cu(5)/γ-Al_2O_3, and Mg(5)/γ-Al_2O_3, (e) Cu(5)Mg(x)/γ-Al_2O_3, and (f) Cu(x)Mg(5)/γ-Al_2O_3. x = 1, 5, and 10 wt%.

4.2 Characterization of the mono-metallic and selected bi-metallic catalysts

The characterization section of this work focuses on the γ-Al_2O_3 support, the mono-metallic Cu(5)/γ-Al_2O_3 and Mg(5)/γ-Al_2O_3 catalysts, and the selected bi-metallic catalyst (Cu(1)Mg(5)/γ-Al_2O_3). The XRD spectra of these materials are shown in Fig. 4.5. Diffraction peaks of γ-Al_2O_3 were present for all the catalysts at 37.7°, 39.4°, 45.8°, and 66.8° (indicated by diamond symbols), which corresponded to alumina's (3 1 1), (2 2 2), (4 0 0), and (4 4 0) crystallographic planes [73]. These high index broad peaks showed the low crystallinity of Al_2O_3. No peaks of copper oxides (CuO and Cu_2O) and MgO were observed in the XRD spectra of the catalysts, suggesting that the size of the Cu and Mg containing particles were less than the detection limit of XRD at around 5 nm (see TEM analysis below).

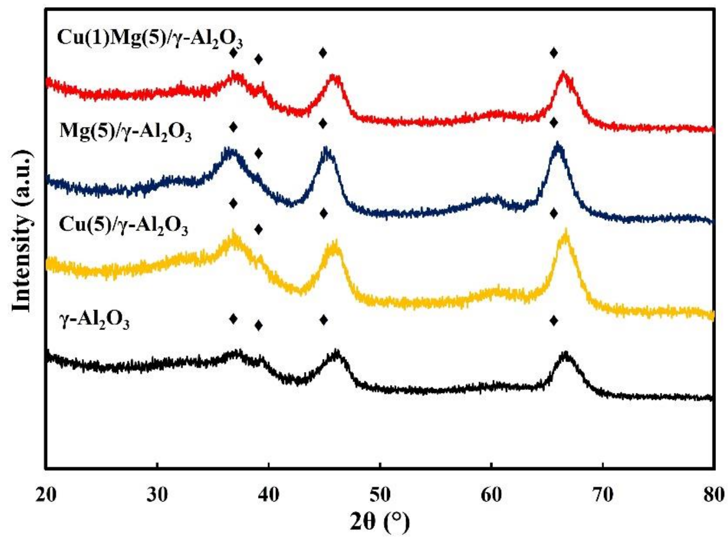

Fig. 4.5. XRD analysis of the γ-Al_2O_3 support and the Cu(5)/γ-Al_2O_3, Mg(5)/γ-Al_2O_3, and Cu(1)Mg(5)/γ-Al_2O_3 catalysts (diamond symbols represent the diffraction peaks of γ-Al_2O_3).

The XPS analysis of the support and catalysts are shown in Fig. 4.6. The wide XPS spectra (Fig. 4.6(a)) showed photoelectron peaks of Mg 2p, Cu $2p_{3/2}$, Cu $L_3M_{4.5}M_{4.5}$, O 1s, and Al 2p, which were separately analyzed in Figs. 4.6(b-f). Mg(5)/γ-Al_2O_3 and Cu(1)Mg(5)/γ-Al_2O_3 showed Mg 2p photoelectron peaks at 50.2 eV in Fig. 4.6(b), which were due to the presence of MgO [74,75]. Cu(5)/γ-Al_2O_3 and Cu(1)Mg(5)/γ-Al_2O_3 showed Cu $2p_{3/2}$ photoelectron peaks centered at 933.4 and 933.0 eV, respectively (Fig. 4.6(c)). The peaks were deconvoluted to two peaks at 933.8 and 932.2 eV, which were assigned to CuO and Cu_2O, respectively. The presence of CuO resulted in two satellite peaks centered at 941.5 and 940.8 eV for Cu(5)/γ-Al_2O_3 and Cu(1)Mg(5)/γ-Al_2O_3, respectively [74,76]. The presence of Cu_2O particles was further confirmed by the Cu $L_3M_{4.5}M_{4.5}$ peak at a binding energy of 570 eV as shown in Fig. 4.6(d) [74,77]. Using the method described by Biesinger

[76,78,79], the ratio of Cu^{2+}/Cu^{total} was calculated as 0.81 and 0.62 for Cu(5)/γ-Al_2O_3 and Cu(1)Mg(5)/γ-Al_2O_3, respectively. This indicated that both Cu containing catalysts had more CuO than Cu_2O. The O 1s peak of the support and the catalysts are shown in Fig. 4.6(e). γ-Al_2O_3 had an O 1s peak centered at 531.4 eV [80]. The O 1s peak shifted to lower values at 531.2, 531.2, and 530.9 eV for Cu(5)/γ-Al_2O_3, Mg(5)/γ-Al_2O_3, and Cu(1)Mg(5)/γ-Al_2O_3, respectively, which were likely related to electron transfer from the support to MgO and CuO_x (CuO and Cu_2O) [81]. The γ-Al_2O_3 support showed an Al 2p binding energy centered at 74.5 eV as shown in Fig. 4.6(f). The binding energy of the Al 2p peak was decreased to 74.1, 74.2, and 74.4 eV for Cu(5)/γ-Al_2O_3, Mg(5)/γ-Al_2O_3, and Cu(1)Mg(5)/γ-Al_2O_3, respectively, which further confirmed the electron transfer from the alumina support to MgO and CuO_x, resulting in a strong metal-support interaction.

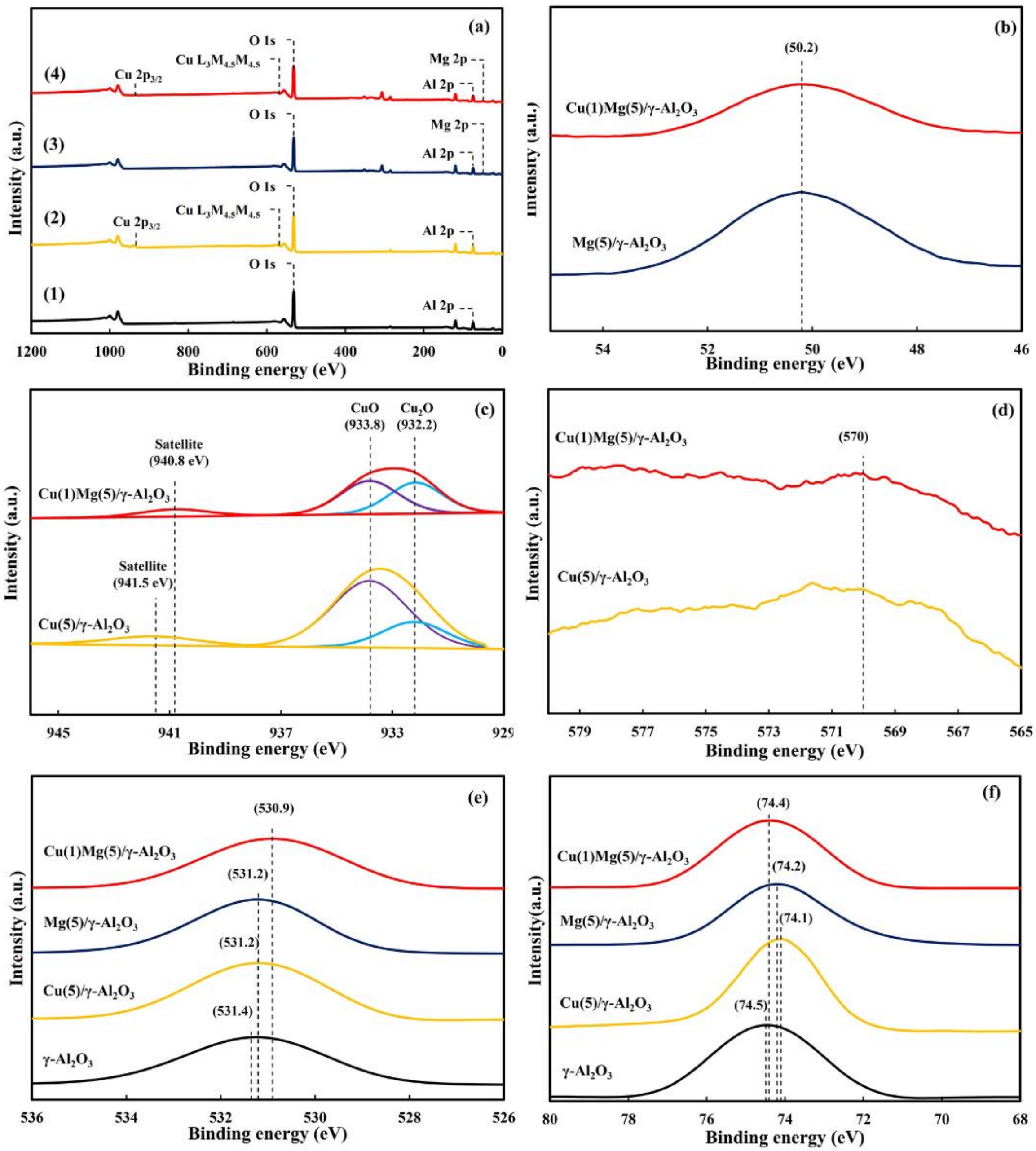

Fig. 4.6. XPS analysis of the γ-Al_2O_3 support and the Cu(5)/γ-Al_2O_3, Mg(5)/γ-Al_2O_3, and Cu(1)Mg(5)/γ-Al_2O_3 catalysts, (a) wide XPS spectra of (1) γ-Al_2O_3, (2) Cu(5)/γ-Al_2O_3, (3) Mg(5)/γ-Al_2O_3, and Cu(1)Mg(5)/γ-Al_2O_3, (b) XPS Mg 2p spectra, (c) XPS Cu $2p_{3/2}$ spectra, (d) Cu $L_3M_{4.5}M_{4.5}$ spectra, (e) XPS O 1s spectra, and (f) XPS Al 2p spectra.

The SEM-EDS analysis of the support and the catalysts are shown in Fig. (4.7). γ-Al_2O_3 had a porous structure (Figs. 4.7(a) and (b)), which was preserved in Cu(5)/γ-Al_2O_3 (Fig. 4.7(c)), Mg(5)/γ-Al_2O_3 (Fig. 4.7(e)), and Cu(1)Mg(5)/γ-Al_2O_3 (Fig. 4.7(g)). The EDS mapping of Cu(5)/γ-Al_2O_3 (Fig. 4.7(d)) and Mg(5)/γ-Al_2O_3 (Fig. 4.7(f)) showed the presence of well dispersed CuO_x and MgO particles on the external surface of the support, respectively. Likewise, the EDS mapping of Cu(1)Mg(5)/γ-Al_2O_3 showed a good dispersion of CuO_x and MgO particles as shown in Figs. 4.7(h) and (i), respectively.

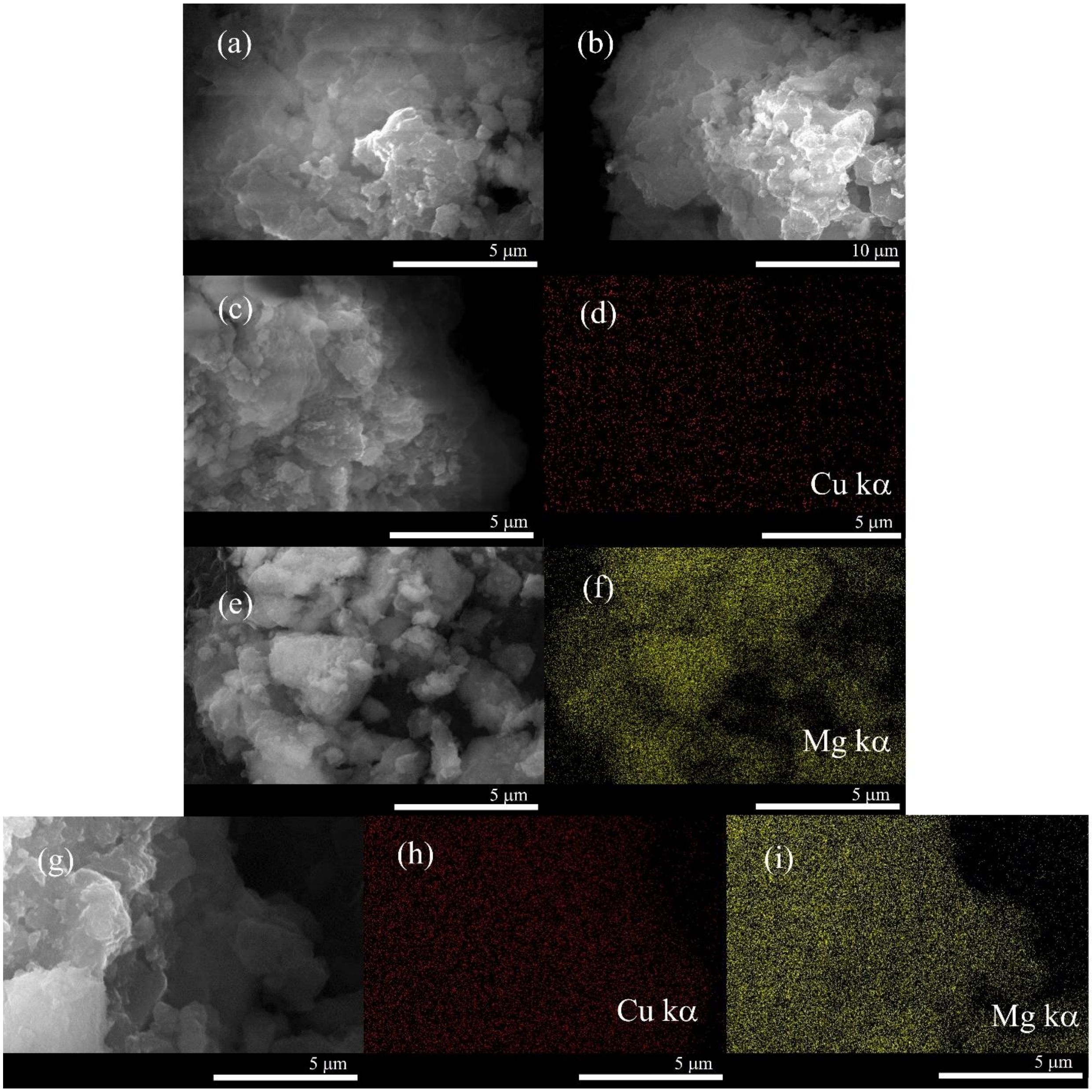

Fig. 4.7. SEM-EDS analysis of (a) and (b): γ-Al_2O_3, (c) and (d): Cu(5)/γ-Al_2O_3, (e) and (f): Mg(5)/γ-Al_2O_3, and (g) to (i) : Cu(1)Mg(5)/γ-Al_2O_3.

The TEM-EDS analysis of the support and catalysts are included in Fig. 4.8. The BF-TEM images of γ-Al_2O_3 (Figs. 4.8(a-b)) showed the fiber shape structure of γ-Al_2O_3

particles with an approximate length of 36 nm. The CuO_x particles were observable in the HAADF image of Cu(5)/γ-Al_2O_3 in Fig. 4.8(c) with estimated size of 1.2 to 2.6 nm (three of them are highlighted by red circles). The CuO_x particles were uniformly dispersed in the porous structure of the support as shown in the EDS analysis of Cu(5)/γ-Al_2O_3 in Fig. 4.8(d). The HAADF image of Mg(5)/γ-Al_2O_3 (Fig. 4.8(e)) did not show the particles of MgO due to the low contrast between Mg and Al. However, the EDS of Mg(5)/γ-Al_2O_3 (Fig. 4.8(f)) showed high dispersion of MgO particles with their size to be likely close to 1 nm. Figs. 4.8(g) to (i) show the HAADF image and EDS mapping of Cu(1)Mg(5)/γ-Al_2O_3. CuO_x particles were observable in the HAADF image of the bi-metallic catalyst in Fig. 4.8(g) since there was enough contrast between Cu and Al (two of them are highlighted by red circles in Fig. 4.8(g)). The size of the largest CuO_x particles identified in the bi-metallic catalyst was close to 1 nm. No MgO particles were observable in Fig. 4.8(g) due to their low contrast with Al atoms. The EDS analyses of Cu and Mg (Figs. 4.8(h) and (i), respectively) showed that the CuO_x and MgO particles remained highly dispersed on γ-Al_2O_3 with the majority of their size being close to 1 nm.

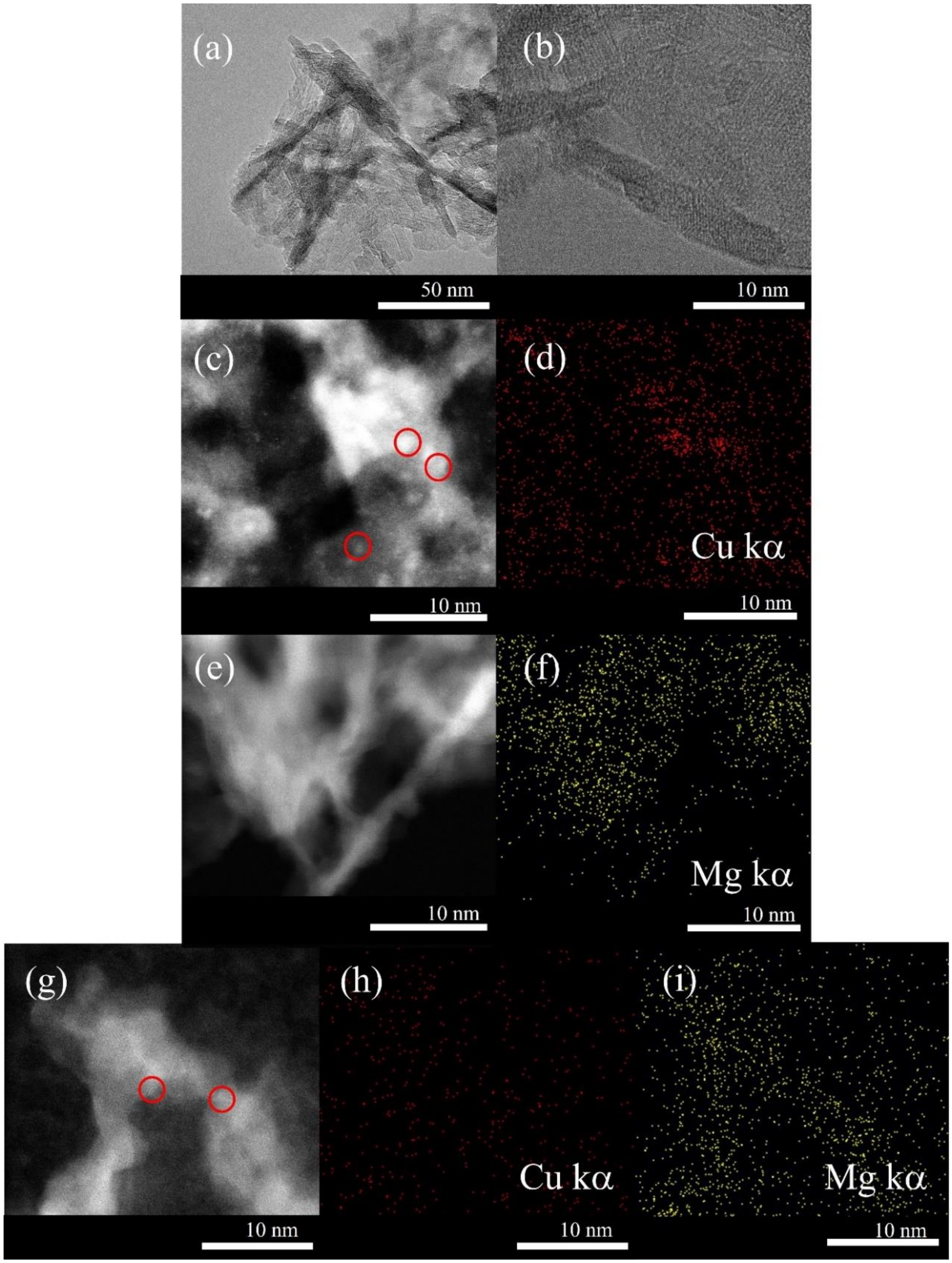

Fig. 4.8. (a) and (b) BF-TEM images of γ-Al_2O_3. HAADF-EDS images of (b) and (c) Cu(5)/γ-Al_2O_3, (d) and (e) Mg(5)/γ-Al_2O_3, and (g) to (i) Cu(1)Mg(5)/γ-Al_2O_3.

The effect of the addition of Cu and Mg on the solid acidity (Brönsted and Lewis acidity) of the support was studied by NH_3-TPD. The NH_3-TPD profiles of the γ-Al_2O_3 support, Cu(5)/γ-Al_2O_3, Mg(5)/γ-Al_2O_3, and Cu(1)Mg(5)/γ-Al_2O_3 are shown in Fig. 4.9. The quantitative analysis of the solid acidity distribution of the materials is given in Table 4.3. The acid sites were classified as weak, moderate, and strong in the temperature ranges of 150-250 °C, 250-450 °C, and >450°C, respectively [72,82,83]. γ-Al_2O_3 had a sharp desorption peak at ≈150 ºC, which was due to the physisorption of NH_3 on alumina's hydroxyl groups [83]. The NH_3 desorption between 150 and 450 ºC could be assigned to the chemisorption of NH_3 on weak Lewis acid sites (Al^{+3} cations in tetra-coordinated sites) and on the surface hydroxyl groups of γ-Al_2O_3 [84–87]. The support then showed a second desorption peak at ≈550 ºC, which was related to the chemisorption of NH_3 on strong Lewis acid sites, which were associated with unsaturated multivalent cations of alumina in tri-coordinated sites [86,87]. As shown in Fig. 4.9, the addition of Cu to alumina in Cu(5)/γ-Al_2O_3 resulted in the appearance of the first desorption peak at ≈150 ºC with the same intensity to that of γ-Al_2O_3. The NH_3 desorption peak of the strong Lewis acid sites was shifted to lower temperatures in Cu(5)/γ-Al_2O_3 with a lower intensity when compared to that of γ-Al_2O_3, which was related to the shielding of strongly acidic aluminum cations by CuO_x particles. [88,89]. When Mg was added to the support in Mg(5)/γ-Al_2O_3, a shoulder appeared at ≈220 ºC, which was due to the adsorption of NH_3 on the surface hydroxyl groups of MgO [90,91]. Mg(5)/γ-Al_2O_3 showed a strong desorption peak at ≈550 ºC with lower intensity comparing to that of the alumina support. The addition of a small amount of Cu to Mg in Cu(1)Mg(5)/γ-Al_2O_3 did not change NH_3 desorption profile of Mg(5)/γ-Al_2O_3 up to 450 ºC. However, the intensity of the strong NH_3 desorption peak was reduced in Cu(1)Mg(5)/γ-Al_2O_3 when compared to that of Mg(5)/γ-Al_2O_3. As summarized in Table 4.3, γ-Al_2O_3 had a total acidity of 0.50 mmol NH_3/g, which was close to the values reported in the literature [92]. The total acidity of γ-Al_2O_3 decreased from 0.50 to 0.42 and 0.39 mmol NH_3/g after the addition of 5 wt% loading of Cu and Mg, respectively. The major cause for this reduction was related to the significant drop of the concentration of strong Lewis acid site (around 0.1 mmol NH_3/g) after the addition of Cu or Mg to the support, while the concentration of weak and moderate acid sites almost remained the same [83,93]. The addition of Cu to Mg in Cu(1)Mg(5)/γ-Al_2O_3 resulted in the lowest concentration of strong Lewis acid sites and the lowest total acidity of 0.36 mmol NH_3/g. An inverse relation was observed between the total acidities reported in Table 4.3 and the pH_{pzc} values reported in Table 4.1 for the γ-Al_2O_3 support and Cu(5)/γ-Al_2O_3, Mg(5)/γ-Al_2O_3, and Cu(1)Mg(5)/γ-Al_2O_3. As the total acidity of the materials decreased, their pH_{pzc} increased. As discussed in Section 4.1, the increase of the pH_{pzc} to values close to the pH of the solution at 8.5 lead to the charge neutrality of the catalysts' surface, which was beneficial for the generation of ROS and the oxidation of 4PCH. Furthermore, the presence of CuO_x particles was also crucial to achieve high TOC removals by Cu(1)Mg(5)/γ-Al_2O_3. The role of Cu is further elucidated in Section 4.3 below.

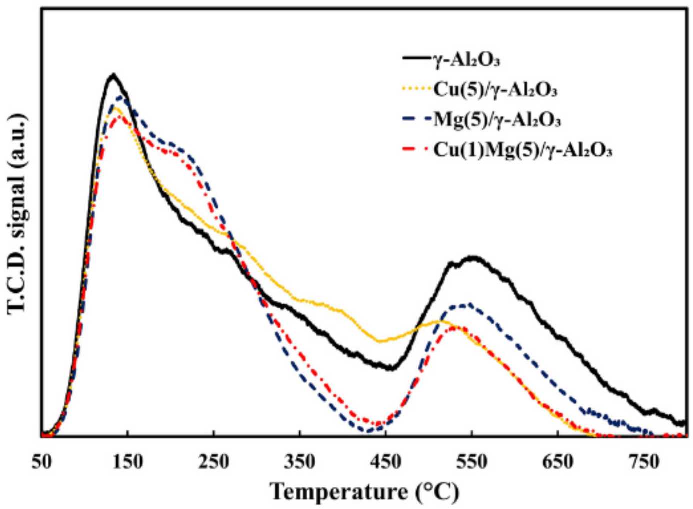

Fig. 4.9. NH_3-TPD profiles of γ-Al_2O_3, Cu(5)/γ-Al_2O_3, Mg(5)/γ-Al_2O_3, and Cu(1)Mg(5)/γ-Al_2O_3.

Table 4.3. Distribution of solid acid sites of the support and the catalysts.

	NH_3 desorbed (mmol/g)				
Catalyst	**Physisorption (T<150 ^oC)**	**Weak acidity (150 ^oC<T<250 ^oC)**	**Moderate acidity (250 ^oC<T<450 ^oC)**	**Strong acidity (450^oC<T)**	**Total acidity [a]**
γ-Al_2O_3	0.11	0.15	0.12	0.23	0.50
Cu(5)/γ-Al_2O_3	0.10	0.15	0.14	0.13	0.42
Mg(5)/γ-Al_2O_3	0.10	0.17	0.10	0.12	0.39
Cu(1)Mg(5)/γ-Al_2O_3	0.10	0.17	0.10	0.09	0.36

[a] Calculated by addition of NH_3 desorbed from the weak, moderate, and strong acidity regions excluding physisorption.

4.3 Reaction mechanism and network

TBA (2.7 mM) was used as a hydroxyl radical scavenger ($k = 3.8\times10^8 – 7.6\times10^8\ M^{-1}s^{-1}$) to determine if OH• radicals played a role in the mineralization of 4PCH by Cu(1)Mg(5)/γ-Al_2O_3 [51]. Fig. 4.10(a) show the normalized concentration profiles of 4PCH in the presence and absence of TBA. As depicted in Fig. 4.10(a), 4PCH was not detected after 18 min of the reaction when no TBA was used. However, the oxidation rate of 4PCH was significantly slowed down in the presence of TBA with detectable 4PCH up to 60 min of the reaction. This indicated that OH• radicals played a major role in the oxidation mechanism of 4PCH in the bulk of the liquid. Fig. 4.10(b) shows the liquid ozone concentration profiles associated with Fig. 4.10(a). The ozone concentration profile showed a gradual decrease in the presence of TBA over the 120 min of the reaction. This was likely because of the fast consumption of OH• radicals in the bulk liquid by TBA, which accelerated the decomposition of molecular ozone to OH• radicals in the bulk of the liquid phase. In the absence of TBA, the ozone concentration profile had a U-shape with a minimum around 40 min due to the fast decomposition of ozone to generate ROS for the oxidation of 4PCH during the early stages of the reaction. The ozone profile then increased to higher values after 40 min since less amount of ROS was needed for the oxidation of the remaining TOC, allowing the dissolution of more ozone in the liquid phase.

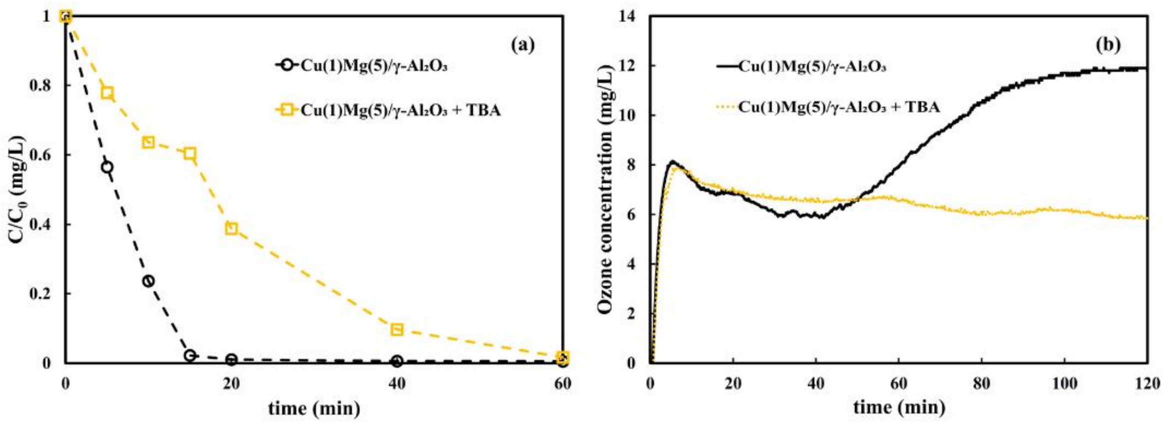

Fig. 4.10. 4PCH oxidation in the absence and presence of TBA, (a) Normalized 4PCH concentration and (b) liquid ozone concentration profiles of Cu(1)Mg(5)/γ-Al_2O_3. Initial 4PCH concentration = 40 mg/L, bicarbonate ionic strength = 5 mM, inlet gas phase ozone concentration = 23,616 ppmv, catalyst dosage = 2 g/L, initial pH = 8.5, TBA concentration = 2.7 mM.

As explained in Section 4.1, the surface hydroxyl groups of the Cu(1)Mg(5)/γ-Al_2O_3 catalyst were neutrally charged. Ozone could be decomposed to hydroxyl ($OH^{\bullet}$) and superoxide ($O_2^{\bullet-}$) radicals by the neutrally charged surface hydroxyl groups of Cu(1)Mg(5)/γ-Al_2O_3 through the cycle presented by Eqs. (4.1) to (4.4) [69]:

$$\text{M-OH} + O_3 \rightarrow \text{M-HO-}O_3 \quad (4.1)$$

$$\text{M-HO-}O_3 \rightarrow \text{M-HO}_2^- + O_2 \quad (4.2)$$

$$\text{M-HO}_2^- + O_3 \rightarrow \text{M} + OH^{\bullet} + O_2^{\bullet-} + O_2 \quad (4.3)$$

$$\text{M} + H_2O \rightarrow \text{M-OH} + H^+ \quad (4.4)$$

where M was used to represent Mg and Al cations. It was unlikely that Cu was involved in reactions (4.1) to (4.4) due its low concentration in comparison to those of Mg and Al. Ozone was first attached to the surface hydroxyl groups to form a M-OH-O_3 complex as shown by Eq. (4.1). The M-OH-O_3 complex decomposed into the deprotonated $-HO_2^-$ surface group and O_2 in Eq. (4.2). The surface $-HO_2^-$ reacted with molecular ozone to form free $OH^\bullet$ and $O_2^{\bullet-}$ radicals and to free M as shown by Eq. (4.3) [44]. The freed metal site adsorbed a water molecule to form a hydroxylated surface in (Eq. (4.4)) to restart the cycle [7,69]. The generated $O_2^{\bullet-}$ and $OH^\bullet$ radicals through Eqs. (4.1) to (4.4) were highly reactive for the oxidation of 4PCH and its by-products.

Section 4.1 also showed that the presence of copper was as important as the amount of surface hydroxyl groups and pH_{pzc}. The role of copper in the generation of ROS and the oxidation of the products of the reaction could be explained by Eqs. (4.5) to (4.11) and Eqs. (4.12) to (4.16), respectively. The following redox cycle between Cu^+ and Cu^{2+} (Eqs. (4.5) to (4.11)) was proposed to explain the role of copper for the generation of ROS [56,94]. The ROS included $O_2^{\bullet-}$, $OH^\bullet$(free radicals in the bulk of the liquid phase), and $OH^\bullet{}_{ads}$ (adsorbed radicals on the surface of copper).

$$Cu^+\text{-}OH + O_3 \rightarrow Cu^{2+}\text{-}O_2H^\bullet + O_2^{\bullet-} \tag{4.5}$$

$$Cu^{2+}\text{-}O_2H^\bullet + O_3 \rightarrow Cu^{2+}\text{-}O_3H^\bullet + O_2 \tag{4.6}$$

$$Cu^{2+}\text{-}O_3H^\bullet \rightarrow Cu^{2+} + O_2 + OH^\bullet \tag{4.7}$$

$$Cu^{2+}\text{-}O_3H^\bullet \rightarrow Cu^{2+}\text{-}OH^\bullet{}_{ads} + O_2 \tag{4.8}$$

$$Cu^{2+}\text{-}OH + O_3 \rightarrow Cu^{2+}\text{-}O_3^\bullet + OH^\bullet{}_{ads} \tag{4.9}$$

$$Cu^{2+}\text{-}O_3^\bullet + H_2O \rightarrow Cu^+ + HO_2^\bullet + O_2 + H^+ \tag{4.10}$$

$$4Cu^{2+} + 2O_{lat}{}^{2-} \rightarrow 4Cu^{+} + O_2 \quad (4.11)$$

Ozone decomposition started through an electron donation from Cu^{+} species to ozone, which lead to the formation of Cu^{2+}-$O_2H^{\bullet}$ and $O_2{}^{\bullet-}$ radicals (Eq. (4.5)). Cu^{2+}-$O_2H^{\bullet}$ further reacted with ozone to form free $OH^{\bullet}$ radicals in the bulk of the liquid phase through Eqs. (4.6) and (4.7). Cu^{2+}-$O_3H^{\bullet}$ formed in Eq. (4.6) could free an oxygen molecule to form adsorbed OH radicals (Cu^{2+}-$OH^{\bullet}{}_{ads}$) as shown by Eq. (4.8). The OH groups of hydroxylated Cu^{2+}-OH could undergo a replacement reaction with O_3 in Eq. (4.9) to form a complex as Cu^{2+}-$O_3{}^{\bullet} + OH^{\bullet}{}_{ads}$. The adsorbed OH radicals ($OH^{\bullet}{}_{ads}$) produced by Eqs. (4.8) and (4.9) were readily available for the oxidation of the reaction by-products on the surface of the catalyst. Cu^{2+} was reduced to Cu^{+} through the reaction of Cu^{2+}-$O_3{}^{\bullet}$ and H_2O in Eq. (4.10). The reduction of Cu^{2+} to Cu^{+} could also proceed by accepting electrons from the lattice oxygen of CuO_x (Eq. (4.11)).

In addition to the involvement of the unsaturated Cu^{2+} (originated from the Cu^{+}) for the generation of ROS through Eqs. (4.5) to (4.11), it could also complex with small carboxylic acidic by-products of 4MCH oxidation (e.g., oxalic acid as identified below) [61,95]. Eqs. (4.12) to (4.16) describe the role of Cu^{2+} in the adsorption of oxalates and in their complete oxidation to CO_2 [59,94,96,97]:

$$Cu(II) + C_2O_4^{-2} \rightarrow Cu(II)C_2O_4^{-2} \quad (4.12)$$

$$Cu(II)C_2O_4^{-2} + O_3 \rightarrow Cu(III)C_2O_4^{-2} + O_3^{\bullet-} \quad (4.13)$$

$$Cu(III)C_2O_4^{-2} \rightarrow Cu(II) + C_2O_4^{\bullet-} \quad (4.14)$$

$$C_2O_4^{\bullet-} + OH^{\bullet} \rightarrow 2CO_2 + OH^{-} \quad (4.15)$$

$$Cu(III)C_2O_4^{-2} + OH^{\bullet}{}_{ads} \rightarrow Cu(II) + 2CO_2 + OH^{-} \quad (4.16)$$

Oxalates ($C_2O_4^{-2}$) first complexed with Cu(II) through Eq. (4.12). The complex ($Cu(II)C_2O_4^{-2}$) then donated an electron to ozone through Eq. (4.13). This resulted in the formation of highly unstable $Cu(III)C_2O_4^{-2}$ complex and $O_3^{\bullet-}$. The $Cu(III)C_2O_4^{-2}$ then dissociated to form Cu(II) and $C_2O_4^{\bullet-}$ (Eq. (4.14)) [61,95]. $C_2O_4^{\bullet-}$ and the unstable $Cu(III)C_2O_4^{-2}$ were finally mineralized to CO_2 by $OH^{\bullet}$ in the bulk of the liquid phase and by adsorbed hydroxyl radicals in Eqs. (4.15) and (4.16), respectively [96,97]. It should be noted that ${OH^{\bullet}}_{ads}$ was generated in Eqs. (4.8) and (4.9) within the Cu^{2+}/Cu^{+} redox cycle.

To further prove the involvement of Cu^{2+}/Cu^{+} redox cycle in the reaction mechanism, the catalyst was recovered after the reaction for XPS analysis. The Cu 2p spectra of the fresh and used catalyst are shown in Fig. 4.11. The XPS analysis showed that the Cu^{2+}/Cu^{total} ratio of the used catalyst was 0.33, which was almost half of that of the fresh catalyst at 0.62. The decrease of Cu^{2+} in the used catalyst was also confirmed by the disappearance of the Cu $2p_{3/2}$ satellite peak in the used catalyst. This indicated the formation of more Cu^{+} at the end of the reaction, confirming the involvement of the Cu^{2+}/Cu^{+} redox cycle in the reaction mechanism. Two new weak photoelectron peaks (denoted by S1 and S2 on Fig. 4.11) were observed in the Cu $2p_{3/2}$ spectra of the used catalyst, which were located at 942.9 and 938.6 eV, respectively. The simultaneous appearance of these new peaks were related to the formation of Cu-$RCOO^{-}$ complexes, confirming the involvement of Cu in the adsorption of reaction by-products [98,99].

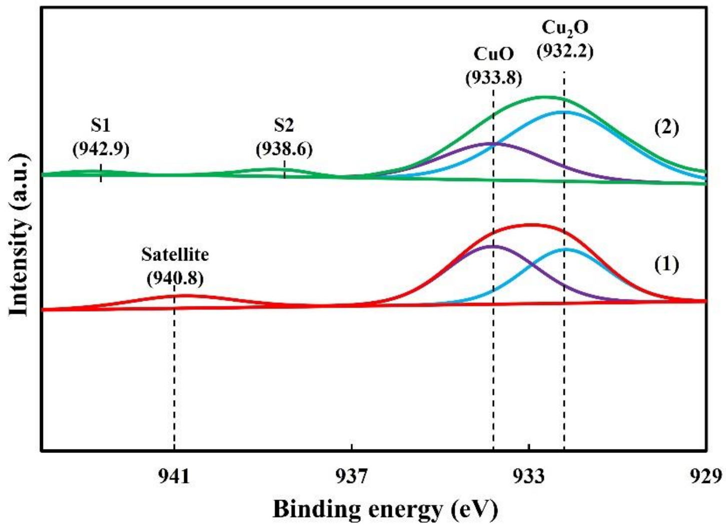

Fig. 4.11. Cu $2p_{3/2}$ photoelectron peaks of the Cu(1)Mg(5)/γ-Al_2O_3 catalyst (1) before and (2) after ozonation of 4PCH.

The by-products of the 4PCH oxidation, identified by MS, are summarized in Table 4.4. A total of 14 by-products (noted P1-P14) were found in the m/z range of 50-240. The time at which each of the by-products had their highest peak intensity is also reported in Table 4.4. P1 to P7 were identified within the first 10 min of the reaction with m/z values in the range of 211 to 229. The appearance of these by-products having m/z values higher than that of 4PCH at 197 indicated that the oxidation of 4PCH was started by the addition of ROS (e.g., OH•) to the ring of 4PCH, forming carboradicals $RO^{\bullet}$ and $RO_2^{\bullet}$ as shown by reaction routes (1) and (2) in Fig. 4.12. The ROS was likely added to the 4PCH ring by electrophilically attacking meta positions of the ring with less steric hindrance in comparison to the ring's ortho positions [35,37]. The meta-addition mechanism was also observed by Ansari et al. for the oxidation of 3-methylcyclohexanecarboxylic acid by OH• radicals [35]. After the formation of $RO^{\bullet}$ and $RO_2^{\bullet}$, the oxidation reactions could proceed through reaction routes (3) and (4). Reaction route (3) involved the transformation of $RO_2^{\bullet}$ to ketone, hydroxyl, and peroxide by-products, which were shown as P1, P2, P3, in Fig. 4.12, respectively. Reaction route (4) was comprised of the C-C bond scission of the $RO^{\bullet}$ carbon to form P4, P5, P6, and P7. In reaction route (4), the occurrence of ring-opening scission at the C-C bond close to the carboxyl group resulted in the formation of hydroxyl and aldehyde groups, i.e., P4 and P5, respectively. On the other hand, if the scission occurred at the C-C bond close to the pentyl group, H-shifts might take place in the open chain, resulting in the formation of P6 and P7. Given that the tertiary carbon attached to the pentyl group in P1-P3 is primed for an electrophilic attack by OH• radicals, the pentyl group could detach from the hexane ring to produce aldehyde (P8), and an alcohol (P9) by-products through reaction route (5) [100]. The tertiary carbon present in P4-P7 was primed to be oxidized via H-abstraction, which resulted in breaking the chain and the formation of aldehyde (P10) and ketone (P11) intermediates through reaction route (6). Further chain breaking in the open chains of P8-P11 resulted in smaller dicarboxylic acids such as P12 to P14 via reaction route (7) [54,101]. The final mineralization of P12 to P14, reaction route (8), could proceed via the complexation mechanism with copper as discussed above. Other possibilities for the mineralization of P12 to P14 could be through an H-abstraction from the carboxyl group and/or the formation of carboradicals at the β-carbon of the carboxyl group as proposed by Oturan et. al [102].

Table 4.4. Identified by-products of the mineralization of 4PCH through HCO using $Cu(1)Mg(5)/\gamma\text{-}Al_2O_3$.

ID	Name	m/z	time (min)[a]
4PCH	trans-4-pentylcyclohexanecarboxylic acid	197	0
P1	4-pentyl-5-oxocyclohexanecarboxylic acid	211	5
P2	3-hydroxy-4-pentylcyclohexanecarboxylic acid	213	5
P3	3-hydroperoxy-4-pentylcyclohexanecarboxylic acid	229	10
P4	2-hydroxymethyl-5-oxomethyldecanoic acid	229	10
P5	2,5-dioxomethyldecanoic acid	227	5
P6	10-hydroxy-2-(2-oxoethyl)decanoic acid	227	5
P7	10-oxo-2-(2-oxoethyl)decanoic acid	229	10
P8	4-formyl-5-oxo(2-oxoethyl)pentanoic acid	171	40
P9	4-formyl-5-oxo(2-hydroxyethyl)pentanoic acid	173	40
P10	1,8-octanedial	141	40
P11	4-formyl-3-oxobutanoic acid	115	100
P12	maleic acid	114	100
P13	oxalic acid	89	100
P14	fumaric acid	71	100

[a] Time at which the corresponding peak is at its highest intensity.

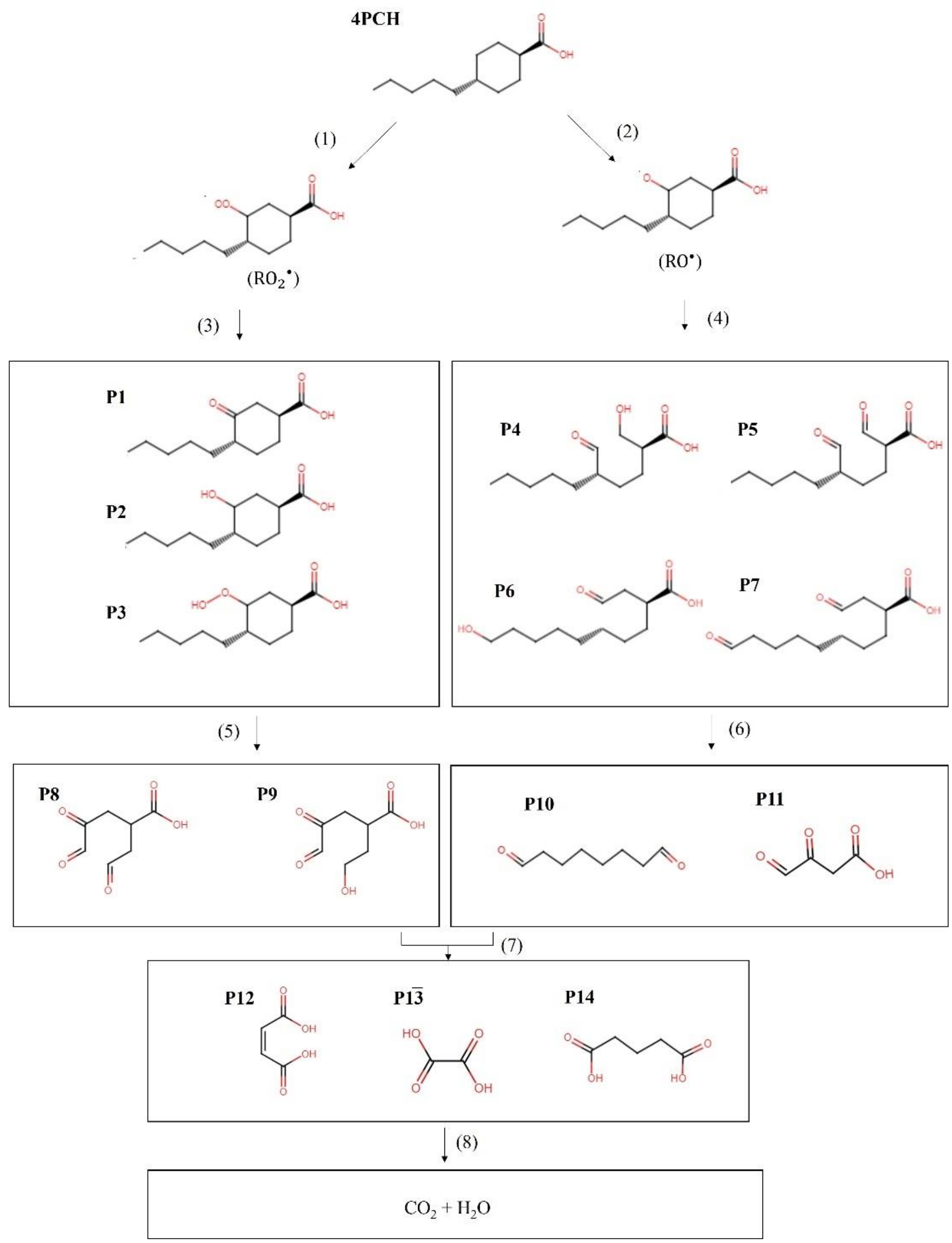

Fig. 4.12. Reaction routes of 4PCH mineralization by ozonation using Cu(1)Mg(5)/γ-Al_2O_3. (1) Formation of $RO_2^{\bullet}$, (2) formation of $RO^{\bullet}$, (3) transformation of $RO_2^{\bullet}$ to ketone, hydroxyl, and peroxide groups, (4) ring opening by C-C scission of $RO^{\bullet}$, (5) ring opening following cleavage of the pentyl group, (6) H-abstraction of the carboxylic group, (7) chain breaking, and (8) mineralization.

4.4 Insights into practical applications of the selected Cu(1)Mg(5)/γ-Al_2O_3

4.4.1 Reusability

Cu(1)Mg(5)/γ-Al_2O_3 was recovered after the reaction by filtration and dried at room temperature for 12 h to be tested for a total of five reusability cycles. Fig. 4.13(a) shows that the TOC removal after 120 min for each cycle was around 89% with no significant difference between the cycles. The pH and liquid ozone concentration profiles of the five cycles associated with Fig. 4.13(a) are presented in Figs. 4.13(b) and 4.13(c), respectively, which also showed no significant difference between the cycles. The FT-IR spectra of the surface of the fresh and used catalyst after each cycle are shown in Fig. 4.13(d). The only adsorbed species were CO_2 (1380, 2360, and 2384 cm^{-1}) and H_2O 1640 and 3460 cm^{-1}, which were likely detected as the result of exposing the catalyst to air before analysis. No adsorption of 4PCH and its reaction by-products was observed on the fresh and used catalysts, indicating that the catalyst active sites were preserved.

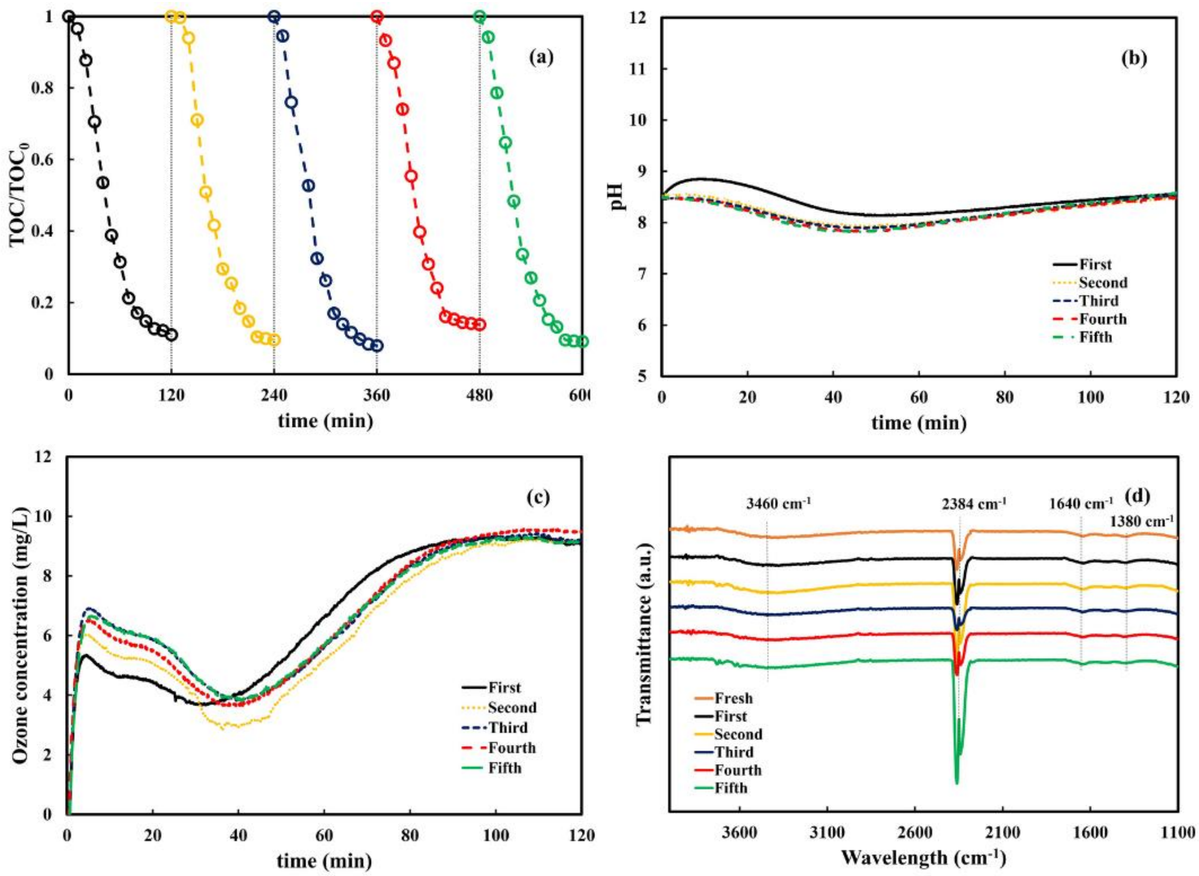

Fig. 4.13. Reusability of Cu(1)Mg(5)/γ-Al_2O_3 for 4PCH mineralization over 5 cycles, (a) Normalized TOC profiles, (b) pH profiles, (c) liquid ozone profiles, and (d) FT-IR spectra of the fresh and used Cu(1)Mg(5)/γ-Al_2O_3 catalyst. Initial 4PCH concentration = 40 mg/L (TOC_0 = 29 mg/L), bicarbonate ionic strength = 5 mM, inlet ozone concentration = 23,616 ppmv, catalyst dosage = 2 g/L, and initial pH = 8.5.

The leaching of Cu, Mg, and Al was analyzed over the five cycles with ICP-OES and the results are shown in Figs. 4.14(a) to (c). An average of 0.07, 1.3, and 0.2 mg/L of Cu, Mg, and Al leached after 120 min of the reaction for the five cycles, respectively. The leached amount of Cu and Mg was significantly lower than those reported in our previous work for a Cu/MgO catalyst, where an average of 3.4 and 44 mg/L of Cu and Mg leached after 125 min over five cycles of reaction of 4MCH oxidation, respectively [10]. The leaching values of Cu in this work were also lower than the ones reported by Sable et al. at 0.5-3.4 mg/L after 120 min oxidation of clofibric acid by a Cu-Mg-Al catalyst [60]. The average Cu leaching in this work at 0.07 mg/L was higher than the maximum allowable discharge limit of 2×10^{-3} mg/L Cu in discharged wastewater established by the Canadian Environmental Quality Guidelines (CEQG). Untreated OSPW was reported to have a Cu content as high as 1 mg/L, which already needed to be removed [3,103]. The average Cu leached from Cu(1)Mg(5)/γ-Al_2O_3 (0.07 mg/L) in our work would only increase the existing Cu content of OSPW by only 7%, which could be removed by treatment methods such as adsorption by carbon based- materials [103]. Dissolved Mg ions were not reported to pose any environmental hazards [3,104]. However, the Mg leaching resulting from the use of Cu(1)Mg(5)/γ-Al_2O_3 could increase the hardness of receiving water bodies if the treated wastewater was discharged to the environment. OSPW already had a hardness of 100 mg $CaCO_3$ eq/L. The average Mg leached from our catalyst would slightly increase the hardness of OSPW by about 5% to 105.3 mg $CaCO_3$ eq/L. As outlined by Babazadeh et al., Mg precipitation in receiving water bodies could be predicted by calculating the Langelier index. In case of the prediction of Mg precipitation, operational parameters such as flow rate and hardness of the discharged OSPW must be adjusted to avoid the precipitation of Mg [10]. The averaged leached Al at 0.2 mg/L was lower than the value reported by Fajardo et al. at 0.5 mg/L for a Pt/Al_2O_3 catalyst used for the ozonation of phenol [105]. It was reported that untreated OSPW had a maximum Al concentration of 0.5 mg/L [3]. The oxidation of NA content of OSPW by Cu(1)Mg(5)/γ-Al_2O_3 would increase the existing Al content of OSPW by 40% to 0.7 mg/L. Even though dissolved Al ions were not classified toxic by CEQG, colloids and precipitates of Al such as $Al(OH)_4$ were considered toxic to aquatic organisms [104,106]. As mentioned by CEQG, the formation of Al colloids and precipitates depended on the pH, hardness, and dissolved organic carbon (DOC) of treated wastewater [104]. Considering the pH and hardness of the wastewater generated from the oxidation of NAs by Cu(1)Mg(5)/γ-Al_2O_3 at 8.5 and 105.3 mg $CaCO_3$ eq/L, respectively, the application of CEQG guidelines would predict the formation of Al colloids and precipitates for DOC values higher than 1 mg/L (assumed for the treated OSPW) [104]. Therefore, Al removal might be necessary, which could be achieved by established microfiltration or coagulation/flocculation technologies [73,74].

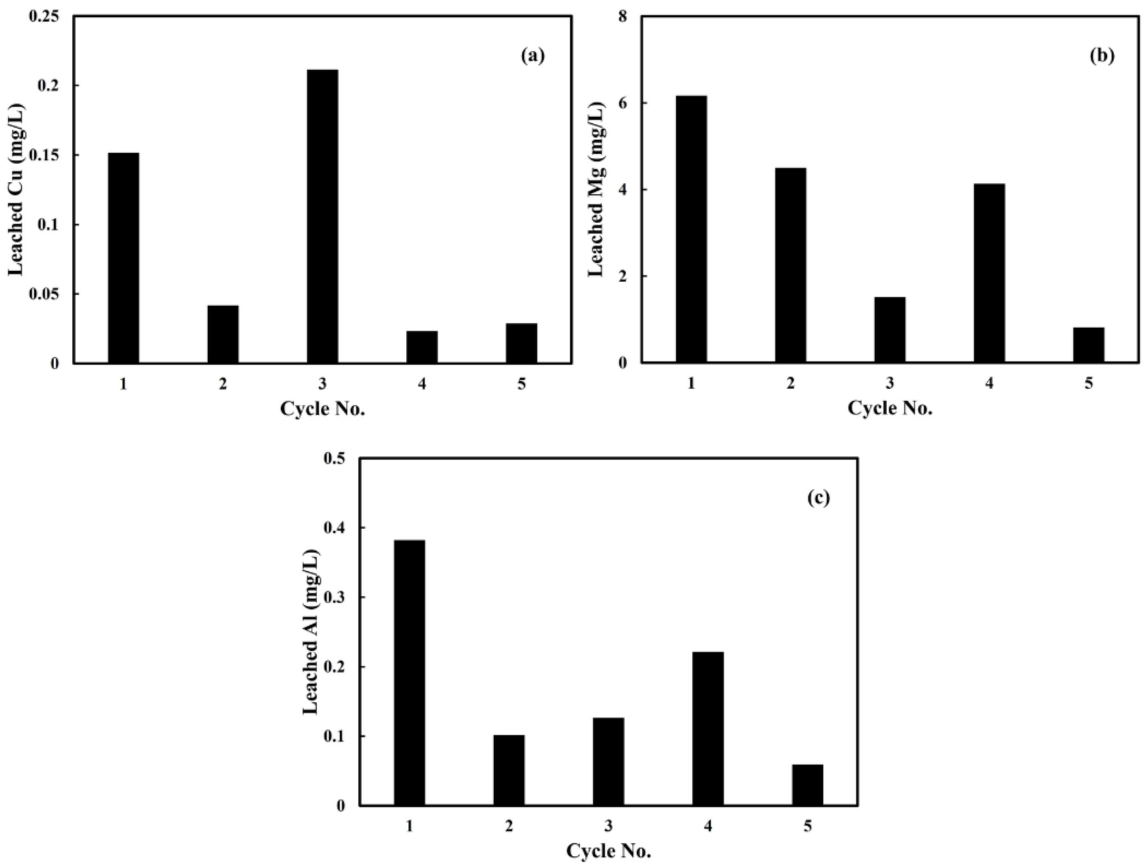

Fig. 4.14. Leaching after five reusability cycles of (a) Cu, (b) Mg, and (c) Al. Initial 4PCH concentration = 40 mg/L (TOC_0 = 29 mg/L), bicarbonate ionic strength = 5 mM, inlet ozone concentration = 23,616 ppmv, catalyst dosage = 2 g/L, and initial pH = 8.5.

4.4.2 Oxidation of a mixture of naphthenic acids

To test the effectiveness of Cu(1)Mg(5)/γ-Al_2O_3 on different NA molecules, the catalytic ozonation of 4MCH, DCHA, and ADA, as well as their mixture with 4PCH was studied. The initial TOC concentration of 4MCH, DCHA, and ADA and their mixture with 4PCH was 29 mg/L (same as the initial TOC concentration in experiments with 4PCH). The normalized TOC removal of the NA molecules is shown in Fig. 4.15. The normalized TOC profiles of 4PCH were also included for comparison as Fig. 4.15(a). The normalized TOC profile of the single ozonation of 4MCH (Fig. 4.15(b)) followed an almost identical trend to that of 4PCH in Fig. 4.15(a). This similarity suggested that the oxidation of 4MCH and 4PCH likely followed a similar mechanism due to the similarity between their molecular structures. The application of Cu(1)Mg(5)/γ-Al_2O_3 increased the TOC removal of 4PCH and 4MCH in comparison to those of single ozonation of the molecules in Figs. 4.15(a) and (b), respectively. The use of Cu(1)Mg(5)/γ-Al_2O_3 also showed an improvement in the mineralization of DCHA and ADA in comparison to their single ozonation in Figs. 4.15(c) and (d), respectively. The final TOC removal of catalytic ozonation of 4PCH, 4MCH, DCHA, and ADA was 90, 90, 97, and 98 % respectively, after 120 min. One could conclude that the order of the difficulty of the oxidation of the 4 model compounds was ADA ≈ DCHA < 4PCH ≈ 4MCH. The higher TOC removal of ADA and DCHA could be related to ease of the oxidation of their tertiary carbon with ROS [43,54]. Fig. 4.15(e) shows the catalytic ozonation of the mixture of the 4 NA model compounds. Cu(1)Mg(5)/γ-Al_2O_3 was found to also be effective for the oxidation of the mixture of NAs with a final TOC removal of 97%, which was 8% higher than the TOC removal of single ozonation of the NAs mixture at 89%.

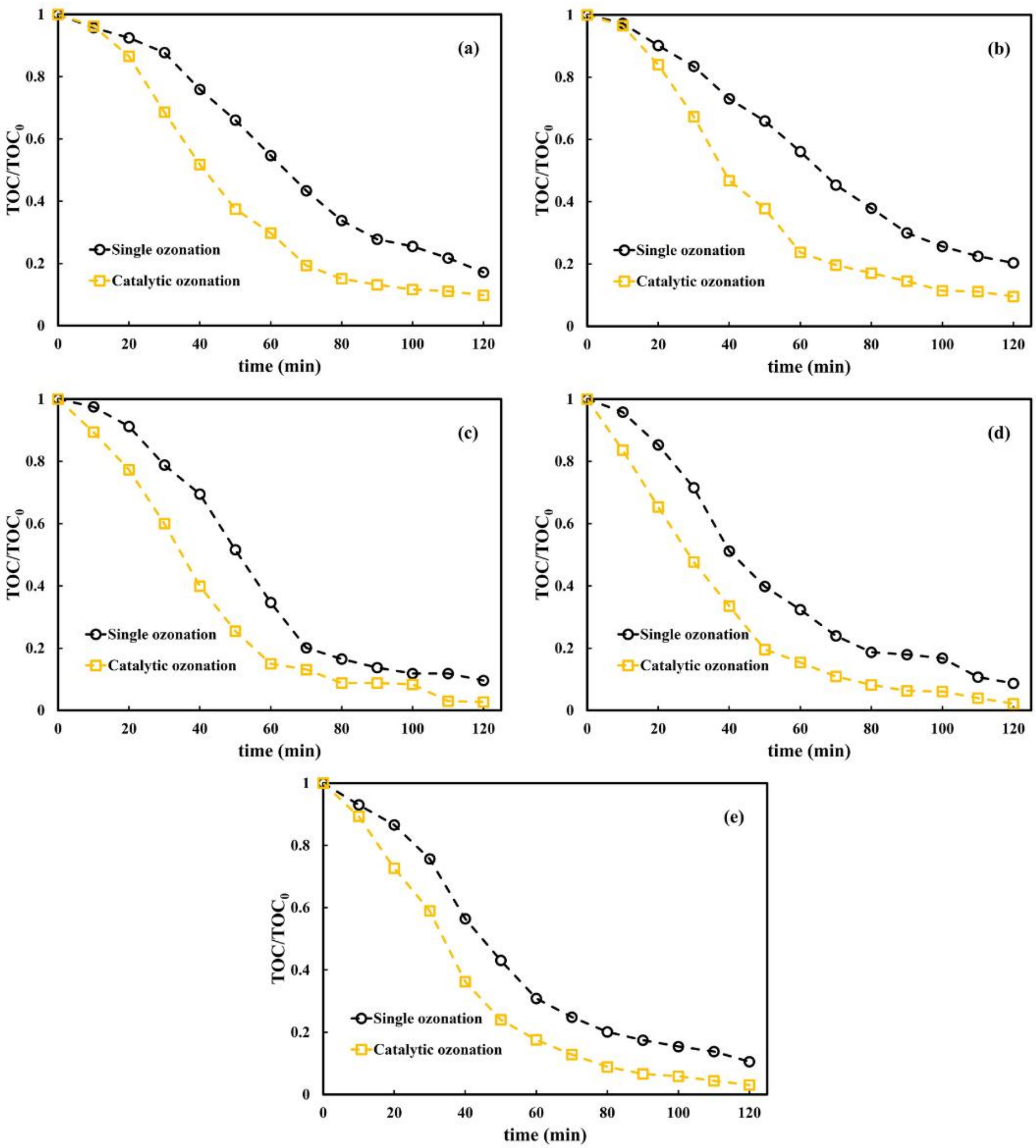

Fig. 4.15. Normalized TOC profiles of the catalytic ozonation of (a) 4PCH, (b) 4MCH, (c) DCHA, (d) ADA, and (e) mixture of 4PCH, 4MCH, DCHA, ADA using Cu(1)Mg(5)/γ-Al_2O_3. TOC_0 = 29 mg/L, bicarbonate ionic strength = 5 mM, inlet ozone concentration = 23,616 ppmv, catalyst dosage 2 g/L.

The plots of -ln(TOC/TOC_0) vs time for the single and catalytic mineralization of 4MCH, DCHA, and ADA, as well as their mixture with 4PCH are shown in Fig. 4.16. The linearity of the plots showed that the oxidation of all four molecules followed a first order kinetics with R^2 values between 0.97 and 0.99. The first order reaction rate constants obtained from the regression of the data are reported in Table 4.5. The single ozonation of 4PCH and 4MCH showed kinetic rate constants of 0.016 and 0.015 min^{-1}, respectively. These constants were increased to 0.022 min^{-1} for both molecules in the presence of Cu(1)Mg(5)/γ-Al_2O_3. Similarly, the application of the catalyst increased the rate constants of the single ozonation of DCHA and ADA from 0.023 and 0.021 min^{-1} to 0.031 min^{-1}. The rate constants single and catalytic ozonation of DCHA and ADA were higher than those of 4PCH and 4MCH since they were easier molecules to be oxidized. The rate constant of the mixture of NA molecules at 0.02 min^{-1} was also increased to 0.031 min^{-1} by Cu(1)Mg(5)/γ-Al_2O_3.

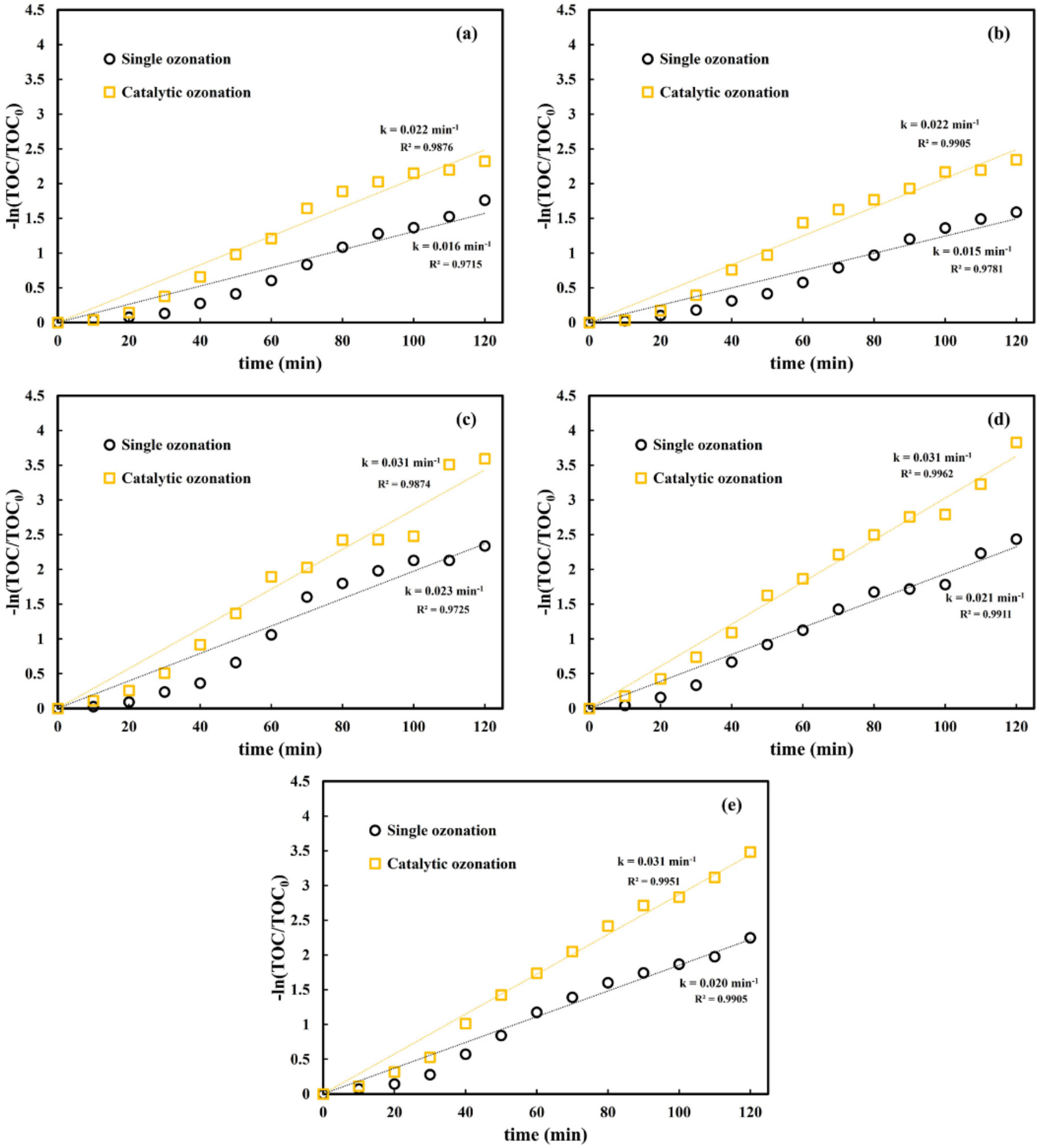

Fig. 4.16. Regression of $-\ln(TOC/TOC_0)$ vs time for the single and catalytic ozonation of (a) 4PCH, (b) 4MCH, (c) DCHA, (d) ADA, (e) mixture of 4PCH, 4MCH, DCHA, ADA using Cu(1)Mg(5)/γ-Al_2O_3. TOC_0 = 29 mg/L, bicarbonate ionic strength = 5 mM, inlet ozone concentration = 23,616 ppmv, catalyst dosage 2 g/L.

Table 4.5. First order kinetic rate constants and electrical energy per order of the single and catalytic mineralization of the different NAs and their mixture by Cu(1)Mg(5)/γ-Al_2O_3.

	Single ozonation		Catalytic ozonation	
NA	**k (min^{-1})**	**E_{EO} (kWh/m^3)**	**k (min^{-1})**	**E_{EO} (kWh/m^3)**
4PCH	0.016	154.4	0.022	117.2
4MCH	0.015	171.1	0.022	116.1
DCHA	0.023	116.3	0.031	75.8
ADA	0.021	111.6	0.031	71.1
Mixture of NAs	0.020	121.0	0.031	78.1

The Electrical Energy per Order (E_{EO}) was used to estimate the treatment energy demand of 4PCH, 4MCH, DCHA, and ADA, as well as their mixture by single ozonation and catalytic ozonation using Cu(1)Mg(5)/γ-Al_2O_3 [107]. The calculation is described by Eq. (4.17), where E_{EO} is in kWh/m^3, P is the input power of the ozone generator in kW (0.13 kW in this study), t is time of ozonation in h, V is the volume of the reactor in L, and TOC/TOC_0 is the normalized TOC removal after 120 min [107].

$$E_{EO} = \frac{P \times t \times 1000}{V \times \log\left(\frac{TOC}{TOC_0}\right)} \tag{4.17}$$

The calculated E_{EO} values are summarized in Table 4.5. The E_{EO} of single ozonation of 4PCH, 4MCH, DCHA, and ADA was 154.4, 171.1, 116.3, and 111.6 kWh/m^3, respectively. The E_{EO} of all NA molecules was decreased in the presence of Cu(1)Mg(5)/γ-Al_2O_3. The E_{EO} was reduced by ≈ 40 kWh/m^3 for all molecules except 4MCH, which was reduced by 55 kWh/m^3 due to the low performance of single ozonation to oxidize it. Overall, higher E_{EO} was required for complete oxidation of NAs with one ring (4PCH and 4MCH) by single and catalytic ozonation when compared to those of NA molecules with multiple rings (ADA and DCHA). The obtained E_{EO} of the single ozonation of the mixture of NA model compounds was 121.0 kWh/m^3, which was reduced to 78.1 kWh/m^3 by Cu(1)Mg(5)/γ-Al_2O_3. In comparison to the E_{EO} of our previously reported Cu/MgO (1 wt%) catalyst used for the mineralization of 4MCH [10], the E_{EO} of Cu(1)Mg(5)/γ-Al_2O_3 at 117.2 kWh/m^3 was significantly lower than that of the Cu/MgO (1 wt%) catalyst at 199 kWh/m^3. This was mainly related to better mineralization rate and final TOC removal of Cu(1)Mg(5)/γ-Al_2O_3 (90% in 120 min) in comparison to that of Cu/MgO (1 wt%) (76% in 125 min). It is worth noting that the treatment of actual OSPW by catalytic ozonation would likely have higher E_{EO} than the values reported in Table 4.5 due to its complex composition and the presence of inorganic compounds that could consume ozone.

4.4.3 Toxicity of the by-products

The acute and chronic toxicity of the by-products of catalytic ozonation of 4PCH by Cu(1)Mg(5)/γ-Al_2O_3 (P1 to P14 summarized in Table 4.4) was predicted using the ECOSAR software via quantitative structure activity relationships (QSARs) [108]. The by-products were categorized into 4 chemical classes by the software, being neutral organics, peroxy acids, mono- and poly-aldehydes. Neutral organics were classified as having “baseline toxicity”, while peroxy acids and mono- and polyaldehydes were identified as chemical classes with “excess toxicity” [109]. The acute and chronic toxicity of the by-products was predicted using specific QSARs for each chemical class that were a function of the logarithm base 10 of the partition coefficient of the by-product molecules in water-octanol mixtures ($\log(k_{ow})$). The toxicity decreases in each chemical class as the value of $\log(k_{ow})$ decreases [109,110]. Each chemical class had a specific $\log(k_{ow})$ value as its toxicity threshold. The acute and chronic toxicity results, as well as the chemical class and $\log(k_{ow})$ value of the by-product molecules are presented in Fig. 4.17. 4PCH was also included in Fig. 4.17 to provide a baseline for toxicity. The toxicity classification was based on the Globally Harmonized System, in which acute toxicity was estimated by the lethal concentration 50 (LC_{50}) and the half maximal effective concentration (EC_{50}), while the chronic toxicity was estimated by the chronic value index (ChV) [111]. 4PCH was identified as a neutral organic molecule with acute and chronic toxicity to fish, daphnid, and green algae with $\log(k_{ow}) = 4.74$. The toxicity of the by-products P1 to P10 (formed during the first 40 min of the reaction) showed an overall decreasing trend as the reaction proceeded. P10 was an outlier to the trend, being classified as harmful. The remaining by-products P11 to P14 (formed after 100 min of the reaction) showed no acute or chronic toxicity. An in-depth experimental study of the toxicity of the reaction medium would be required to identify the ozonation duration that resulted in a wastewater without acute and chronic toxicity. Nevertheless, the preliminary toxicity results of this work suggested that the reaction could be stopped at 100 min for safe discharge of the treated wastewater of 4PCH oxidation, which would reduce the energy demand of 4PCH removal.

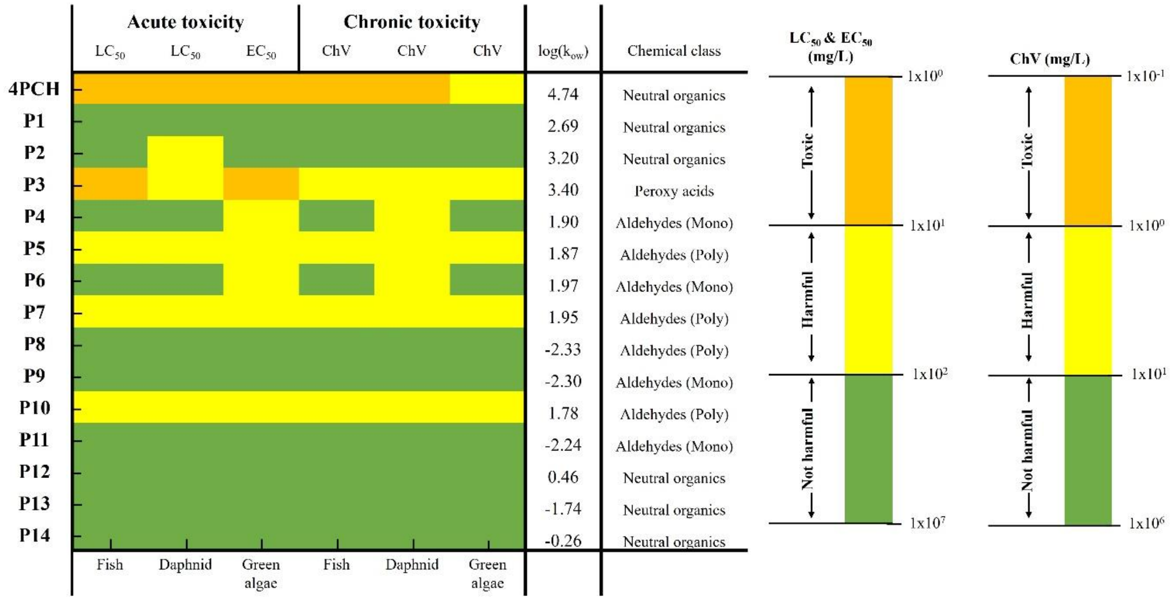

Fig. 4.17. Toxicity analysis of the by-product of 4PCH ozonation by Cu(1)Mg(5)/γ-Al_2O_3.

Chapter 5: Conclusions and recommendations

5.1 Conclusions

A bi-metallic catalyst based on Cu and Mg dispersed on γ-Al_2O_3 was formulated for the complete oxidation of 4PCH in this thesis. The optimum formulation of the bi-metallic catalyst was found to be 1 wt% Cu and 5 wt% Mg denoted as Cu(1)Mg(5)/γ-Al_2O_3. A 90% TOC removal of 4PCH was found using 2 g/L of Cu(1)Mg(5)/γ-Al_2O_3. It was found that a sufficient amount of surface hydroxyl groups played a role in increasing the TOC removal during the first 50 min of reaction, while pH_{pzc} values close to the solution pH and the presence of Cu played a role in increasing TOC removal after 120 min of reaction.

XPS and TEM analyses confirmed the presence of MgO and CuO_x (CuO and Cu_2O) particles on the Cu(1)Mg(5)/γ-Al_2O_3 catalyst with the majority of their size being close to 1 nm. XPS analyses also confirmed the presence of higher amounts of CuO compared to Cu_2O particles in copper-containing catalysts. The total acidity of the catalysts (Lewis and Brönsted acidity) determined by the NH_3-TPD analysis showed that Cu and Mg reduced the Lewis acidity of γ-Al_2O_3. The addition of Mg fine-tuned the pH_{pzc} of the catalyst to the desired values close to the solution pH.

The catalytic ozonation of 4PCH in the presence of TBA confirmed that hydroxyl radicals played a role in the oxidation process. An ROS based mechanism was proposed for the mineralization of 4PCH by the Cu(1)Mg(5)/γ-Al_2O_3 catalyst. The presence of neutrally charged surface hydroxyl groups on the surface of Cu(1)Mg(5)/γ-Al_2O_3 accelerated ozone decomposition to generate ROS ($OH^{\bullet}$ and $O_2^{\bullet -}$) to oxidize 4MCH and some of its by-products in the bulk of the liquid phase. The used catalyst contained a higher content of Cu_2O than the fresh catalyst, which confirmed that copper underwent a redox cycle to generate $OH^{\bullet}$ and $O_2^{\bullet -}$ in the bulk of the liquid phase and to form ${OH^{\bullet}}_{ads}$ on the surface of the catalyst. It was believed that the adsorbed OH radicals (${OH^{\bullet}}_{ads}$) oxidized small by-products molecules (e.g., oxalic acids) adsorbed on the surface of CuO_x particles. The reaction by-products of 4PCH oxidation were identified and a reaction network for the degradation of 4PCH by ROS was proposed. The mineralization of 4PCH was initiated through a meta-addition mechanism, which was followed by ring opening or the formation of ketone, aldehyde, alcohol, and peroxide functional groups. Further oxidation of ring-free by-products resulted in the formation of short dicarboxylic acids, which were completely oxidized to CO_2 and H_2O.

The selected Cu(1)Mg(5)/γ-Al_2O_3 catalyst maintained its activity through five reusability test cycles. The average leaching of Cu and Mg from the Cu(1)Mg(5)/γ-Al_2O_3 catalyst was significantly reduced in comparison to the values reported in our previous work for a Cu/MgO catalyst. The Cu(1)Mg(5)/γ-Al_2O_3 catalyst was efficient in the TOC removal of other NA model compounds (4MCH, ADA, and DCHA) and their mixture with 4PCH. The bi-metallic catalyst also significantly reduced the energy demand of the treatment of NAs when compared to values reported by us for the Cu/MgO catalyst. The toxicity analysis indicated that reaction by-products identified after 100 min of the reaction did not show any acute and chronic toxicity.

5.2 Recommendations for future work

The results of this dissertation proved the potential of Cu(1)Mg(5)/γ-Al_2O_3 to mineralize recalcitrant NA molecules by ozone. Additionally, this work provided insights into practical applications of the HCO process using Cu(1)Mg(5)/γ-Al_2O_3 for NA oxidation. Several research areas were identified to further investigate the scientific and practical aspects of the HCO of NAs. Recommendations for future work are described below.

In order to prove the efficiency of HCO using Cu(1)Mg(5)/γ-Al_2O_3 to completely oxidize NAs from OSPW, it is recommended to test the catalyst with real OSPW samples. Furthermore, it is recommended to study the placement of HCO using Cu(1)Mg(5)/γ-Al_2O_3 in an OSPW treatment train that comprehensively addresses the environmental concerns of the different components of OSPW such as Cu and Al.

It is recommended to use probe-based methods using different scavengers such as TBA, p-BQ, and NaN_3 to quantify the contribution of $OH^{\bullet}$, $O_2^{\bullet -}$, and $^1O_2$ in the 4PCH mineralization process by HCO. Furthermore, the quantification of ROS contribution will allow the development of kinetic models, which will be useful for reactor design and scale-up of the process.

The results of this work suggested that Cu complexed with small carboxylic acid molecules and generate free and adsorbed OH radicals for their oxidation. It is recommended that the Cu-carboxylate complexes are further confirmed by in-situ FTIR to shed light on the mechanism of reactions occurring on the surface of the catalyst for the oxidation of small carboxylic acid molecules to CO_2 and H_2O.

Although toxicity predictions were theoretically performed in this work, it is recommended to experimentally study the toxicity of the reaction medium to confirm the time when the reaction medium is environmentally safe for discharge, which can potentially reduce the energy demands of the HCO process.

References

[1] BP, Statistical Review of World Energy globally consistent data on world energy markets and authoritative publications in the field of energy, 2021.

[2] N.R. Canada, Oil Sands Extraction and Processing, (2016). https://natural-resources.canada.ca/our-natural-resources/energy-sources-distribution/fossil-fuels/crude-oil/oil-sands-extraction-and-processing/18094.

[3] E.W. Allen, Process water treatment in Canada's oil sands industry: I. Target pollutants and treatment objectives, J. Environ. Eng. Sci. 7 (2008) 123–138. https://doi.org/10.1139/S07-038.

[4] E.W. Allen, Process water treatment in Canada's oil sands industry: II. A review of emerging technologies, J. Environ. Eng. Sci. 7 (2008) 499–524. https://doi.org/10.1139/S08-020.

[5] G. of Canada, Introduction to the Crown-Indigenous Working Group for the Potential Oil Sands Mining Effluent Regulations, (2023). https://www.canada.ca/en/environment-climate-change/services/managing-pollution/sources-industry/mining-effluent/oil-sands/crown-indigenous-working-group-engagement.html.

[6] N. Wang, P. Chelme-Ayala, L. Perez-Estrada, E. Garcia-Garcia, J. Pun, J.W. Martin, M. Belosevic, M. Gamal El-Din, Impact of ozonation on naphthenic acids speciation and toxicity of oil sands process-affected water to vibrio fischeri and mammalian

immune system, Environ. Sci. Technol. 47 (2013) 6518–6526. https://doi.org/10.1021/es4008195.

[7] J. Nawrocki, B. Kasprzyk-Hordern, The efficiency and mechanisms of catalytic ozonation, Appl. Catal. B Environ. 99 (2010) 27–42. https://doi.org/10.1016/j.apcatb.2010.06.033.

[8] A.K.H. Al jibouri, J. Wu, S.R. Upreti, Heterogeneous catalytic ozonation of naphthenic acids in water, Can. J. Chem. Eng. 97 (2019) 67–73. https://doi.org/10.1002/cjce.23209.

[9] S.A. Messele, P. Chelme-Ayala, M. Gamal El-Din, Catalytic ozonation of naphthenic acids in the presence of carbon-based metal-free catalysts: Performance and kinetic study, Catal. Today. 361 (2021) 102–108. https://doi.org/10.1016/j.cattod.2020.01.042.

[10] M. Babazadeh, E. Rezaei, B. Liao, Mineralization of 4-methyl-1-cyclohexane carboxylic acid by heterogeneous catalytic ozonation, J. Environ. Chem. Eng. 11 (2023) 110909. https://doi.org/10.1016/j.jece.2023.110909.

[11] C. Chen, Y. Li, W. Ma, S. Guo, Q. Wang, Q.X. Li, Mn-Fe-Mg-Ce loaded Al2O3 catalyzed ozonation for mineralization of refractory organic chemicals in petroleum refinery wastewater, Sep. Purif. Technol. 183 (2017) 1–10. https://doi.org/10.1016/j.seppur.2017.03.054.

[12] Y. Xu, Z. Lin, Y. Zheng, J.P. Dacquin, S. Royer, H. Zhang, Mechanism and kinetics of catalytic ozonation for elimination of organic compounds with spinel-type CuAl2O4 and its precursor, Sci. Total Environ. 651 (2019) 2585–2596.

https://doi.org/10.1016/j.scitotenv.2018.10.005.

[13] T. Shen, W. Su, Q. Yang, J. Ni, S. Tong, Synergetic mechanism for basic and acid sites of MgMxOy (M = Fe, Mn) double oxides in catalytic ozonation of p-hydroxybenzoic acid and acetic acid, Appl. Catal. B Environ. 279 (2020) 119346. https://doi.org/10.1016/j.apcatb.2020.119346.

[14] F. Zhang, C. Wei, K. Wu, H. Zhou, Y. Hu, S. Preis, Mechanistic evaluation of ferrite AFe2O4 (A = Co, Ni, Cu, and Zn) catalytic performance in oxalic acid ozonation, Appl. Catal. A Gen. 547 (2017) 60–68. https://doi.org/10.1016/j.apcata.2017.08.025.

[15] D.K. Banerjee, Oil Sands, Heavy Oil & Bitumen: From Recovery to Refinery, 2012.

[16] A.E. Regulator, Oil Sands Mining, 2023.

[17] Alberta Energy Regulator, State of Fluid Tailings Management for Mineable Oil Sands, 2022, 2022. www.aer.ca.

[18] ECCC, Introduction to the Crown-Indigenous Working Group for the Potential Oil Sands Mining Effluent Regulations, (2023).

[19] J.S. Clemente, P.M. Fedorak, A review of the occurrence, analyses, toxicity, and biodegradation of naphthenic acids, Chemosphere. 60 (2005) 585–600. https://doi.org/10.1016/j.chemosphere.2005.02.065.

[20] E. V. Barros, P.R. Filgueiras, V. Lacerda, R.P. Rodgers, W. Romão, Characterization of naphthenic acids in crude oil samples – A literature review, Fuel. 319 (2022). https://doi.org/10.1016/j.fuel.2022.123775.

[21] P.J. Quinlan, K.C. Tam, Water treatment technologies for the remediation of

naphthenic acids in oil sands process-affected water, Chem. Eng. J. 279 (2015) 696–714. https://doi.org/10.1016/j.cej.2015.05.062.

[22] E. Garcia-Garcia, J. Pun, L.A. Perez-Estrada, M.G. El Din, D.W. Smith, J.W. Martin, M. Belosevic, Commercial naphthenic acids and the organic fraction of oil sands process water downregulate pro-inflammatory gene expression and macrophage antimicrobial responses, Toxicol. Lett. 203 (2011) 62–73. https://doi.org/10.1016/j.toxlet.2011.03.005.

[23] R. Huang, Y. Chen, M.N.A. Meshref, P. Chelme-Ayala, S. Dong, M.D. Ibrahim, C. Wang, N. Klamerth, S.A. Hughes, J. V. Headley, K.M. Peru, C. Brown, A. Mahaffey, M. Gamal El-Din, Characterization and determination of naphthenic acids species in oil sands process-affected water and groundwater from oil sands development area of Alberta, Canada, Water Res. 128 (2018) 129–137. https://doi.org/10.1016/j.watres.2017.10.003.

[24] V. V. Rogers, K. Liber, M.D. MacKinnon, Isolation and characterization of naphthenic acids from athabasca oil sands tailings pond water, Chemosphere. 48 (2002) 519–527. https://doi.org/10.1016/S0045-6535(02)00133-9.

[25] R.A. Frank, K. Fischer, R. Kavanagh, B. Kent Burnison, G. Arsenault, J. V. Headley, K.M. Peru, D.E.R. Van Glen Kraak, K.R. Solomon, Effect of carboxylic acid content on the acute toxicity of oil sands naphthenic acids, Environ. Sci. Technol. 43 (2009) 266–271. https://doi.org/10.1021/es8021057.

[26] P.R. Kannel, T.Y. Gan, Naphthenic acids degradation and toxicity mitigation in tailings wastewater systems and aquatic environments: A review, J. Environ. Sci.

Heal. - Part A Toxic/Hazardous Subst. Environ. Eng. 47 (2012) 1–21. https://doi.org/10.1080/10934529.2012.629574.

[27] N. McKenzie, S. Yue, X. Liu, B.A. Ramsay, J.A. Ramsay, Biodegradation of naphthenic acids in oils sands process waters in an immobilized soil/sediment bioreactor, Chemosphere. 109 (2014) 164–172. https://doi.org/10.1016/j.chemosphere.2014.02.001.

[28] S. Yue, B.A. Ramsay, J. Wang, J.A. Ramsay, Biodegradation and detoxification of naphthenic acids in oil sands process affected waters, Sci. Total Environ. 572 (2016) 273–279. https://doi.org/10.1016/j.scitotenv.2016.07.163.

[29] M. Arslan, J.A. Müller, M. Gamal El-Din, Aerobic naphthenic acid-degrading bacteria in petroleum-coke improve oil sands process water remediation in biofilters: DNA-stable isotope probing reveals methylotrophy in Schmutzdecke, Sci. Total Environ. 815 (2022). https://doi.org/10.1016/j.scitotenv.2021.151961.

[30] C. Wu, A. De Visscher, I.D. Gates, On naphthenic acids removal from crude oil and oil sands process-affected water, Fuel. 253 (2019) 1229–1246. https://doi.org/10.1016/j.fuel.2019.05.091.

[31] C. Whitby, Microbial Naphthenic Acid Degradation, 1st ed., Elsevier Inc., 2010. https://doi.org/10.1016/S0065-2164(10)70003-4.

[32] E. Vaiopoulou, T.M. Misiti, S.G. Pavlostathis, Removal and toxicity reduction of naphthenic acids by ozonation and combined ozonation-aerobic biodegradation, Bioresour. Technol. 179 (2015) 339–347. https://doi.org/10.1016/j.biortech.2014.12.058.

[33] D.C.C. da S. Medeiros, P. Chelme-Ayala, M. Gamal El-Din, Sludge-based activated biochar for adsorption treatment of real oil sands process water: Selectivity of naphthenic acids, reusability of spent biochar, leaching potential, and acute toxicity removal, Chem. Eng. J. 463 (2023). https://doi.org/10.1016/j.cej.2023.142329.

[34] H. Demir-Duz, L.A. Perez-Estrada, M.G. Álvarez, M. Gamal El-Din, S. Contreras, O3/H2O2 and UV-C light irradiation treatment of oil sands process water, Sci. Total Environ. 832 (2022). https://doi.org/10.1016/j.scitotenv.2022.154804.

[35] R. Ansari, D.M. Kirpalani, Insights into ultrasound-promoted degradation of naphthenic acid compounds in oil sands process affected water. Part I: Accelerated H-abstraction and decarboxylation of aromatic and alicyclic compounds, Ultrason. Sonochem. 83 (2022). https://doi.org/10.1016/j.ultsonch.2022.105929.

[36] P. Kumar, J. Headley, K. Peru, J. Bailey, A. Dalai, Removal of dicyclohexyl acetic acid from aqueous solution using ultrasound, ozone and their combination, J. Environ. Sci. Heal. - Part A Toxic/Hazardous Subst. Environ. Eng. 49 (2014) 1512–1519. https://doi.org/10.1080/10934529.2014.938523.

[37] A.S. Abdalrhman, C. Wang, Z.T. How, M. Gamal El-Din, Degradation of cyclohexanecarboxylic acid as a model naphthenic acid by the UV/chlorine process: Kinetics and by-products identification, J. Hazard. Mater. 402 (2021). https://doi.org/10.1016/j.jhazmat.2020.123476.

[38] X. Xu, G. Pliego, J.A. Zazo, S. Liu, J.A. Casas, J.J. Rodriguez, Two-step persulfate and Fenton oxidation of naphthenic acids in water, J. Chem. Technol. Biotechnol. 93 (2018) 2262–2270. https://doi.org/10.1002/jctb.5569.

[39] A. Abdelrahman, S.O. Ganiyu, M. Gamal El-Din, Degradation of surrogate and real naphthenic acids from simulated and real oil sands process water using electrochemically activated peroxymonosulfate (EO-PMS) process, Sep. Purif. Technol. 306 (2023). https://doi.org/10.1016/j.seppur.2022.122462.

[40] V. Kumar, M.P. Shah, Advanced oxidation processes for complex wastewater treatment, Elsevier Inc., 2020. https://doi.org/10.1016/B978-0-12-821011-6.00001-3.

[41] S.I.G. Costa, F.L. Ferreira, S.E. Weschenfelder, J.V.R. Fuck, M. de F.R. da Cunha, B.A. Marinho, L.P. Mazur, A. da Silva, S.M.A.G.U. de Souza, A.A.U. de Souza, Towards the removal of soluble organic compounds present in oilfield produced water by advanced oxidation processes: Critical review and future directions, Process Saf. Environ. Prot. 174 (2023) 608–626. https://doi.org/10.1016/j.psep.2023.04.032.

[42] A.S. Stasinakis, Use of selected advanced oxidation processes (AOPs) for wastewater treatment - A mini review, Glob. Nest J. 10 (2008) 376–385. https://doi.org/10.30955/gnj.000598.

[43] A.C. Scott, W. Zubot, M.D. MacKinnon, D.W. Smith, P.M. Fedorak, Ozonation of oil sands process water removes naphthenic acids and toxicity, Chemosphere. 71 (2008) 156–160. https://doi.org/10.1016/j.chemosphere.2007.10.051.

[44] F. Beltran, Ozone reaction kinetics for water and wastewater systems, 2005.

[45] G. Yu, Y. Wang, H. Cao, H. Zhao, Y. Xie, Reactive Oxygen Species and Catalytic Active Sites in Heterogeneous Catalytic Ozonation for Water Purification, Environ. Sci. Technol. 54 (2020) 5931–5946. https://doi.org/10.1021/acs.est.0c00575.

[46] J. Staehelin, J. Holgné, Decomposition of Ozone in Water: Rate of Initiation by Hydroxide Ions and Hydrogen Peroxide, Environ. Sci. Technol. 16 (1982) 676–681. https://doi.org/10.1021/es00104a009.

[47] B.G. Ershov, P.A. Morozov, The kinetics of ozone decomposition in water, the influence of pH and temperature, Russ. J. Phys. Chem. A. 83 (2009) 1295–1299. https://doi.org/10.1134/S0036024409080093.

[48] Y. Guo, J. Long, J. Huang, G. Yu, Y. Wang, Can the commonly used quenching method really evaluate the role of reactive oxygen species in pollutant abatement during catalytic ozonation?, Water Res. 215 (2022). https://doi.org/10.1016/j.watres.2022.118275.

[49] J. Wang, H. Chen, Catalytic ozonation for water and wastewater treatment: Recent advances and perspective, Sci. Total Environ. 704 (2020) 135249. https://doi.org/10.1016/j.scitotenv.2019.135249.

[50] Y. Guo, Y. Zhang, G. Yu, Y. Wang, Revisiting the role of reactive oxygen species for pollutant abatement during catalytic ozonation: The probe approach versus the scavenger approach, Appl. Catal. B Environ. 280 (2021). https://doi.org/10.1016/j.apcatb.2020.119418.

[51] S. Psaltou, E. Kaprara, K. Triantafyllidis, M. Mitrakas, A. Zouboulis, Heterogeneous catalytic ozonation: The significant contribution of PZC value and wettability of the catalysts, J. Environ. Chem. Eng. 9 (2021) 106173. https://doi.org/10.1016/j.jece.2021.106173.

[52] Y. Guo, G. Yu, U. von Gunten, Y. Wang, Evaluation of the role of superoxide

radical as chain carrier for the formation of hydroxyl radical during ozonation, Water Res. 242 (2023). https://doi.org/10.1016/j.watres.2023.120158.

[53] Y. Wang, Y. Xie, H. Sun, J. Xiao, H. Cao, S. Wang, Efficient Catalytic Ozonation over Reduced Graphene Oxide for p-Hydroxylbenzoic Acid (PHBA) Destruction: Active Site and Mechanism, ACS Appl. Mater. Interfaces. 8 (2016) 9710–9720. https://doi.org/10.1021/acsami.6b01175.

[54] L.A. Pérez-Estrada, X. Han, P. Drzewicz, M. Gamal El-Din, P.M. Fedorak, J.W. Martin, Structure-reactivity of naphthenic acids in the ozonation process, Environ. Sci. Technol. 45 (2011) 7431–7437. https://doi.org/10.1021/es201575h.

[55] M.S. Islam, J. Moreira, P. Chelme-Ayala, M. Gamal El-Din, Prediction of naphthenic acid species degradation by kinetic and surrogate models during the ozonation of oil sands process-affected water, Sci. Total Environ. 493 (2014) 282–290. https://doi.org/10.1016/j.scitotenv.2014.05.138.

[56] W. Chen, H. He, J. Liang, X. Wei, X. Li, J. Wang, L. Li, A comprehensive review on metal based active sites and their interaction with O3 during heterogeneous catalytic ozonation process: Types, regulation and authentication, J. Hazard. Mater. 443 (2023) 130302. https://doi.org/10.1016/j.jhazmat.2022.130302.

[57] J. Wang, Z. Bai, Fe-based catalysts for heterogeneous catalytic ozonation of emerging contaminants in water and wastewater, Chem. Eng. J. 312 (2017) 79–98. https://doi.org/10.1016/j.cej.2016.11.118.

[58] T. Zhang, J. Ma, Catalytic ozonation of trace nitrobenzene in water with synthetic goethite, J. Mol. Catal. A Chem. 279 (2008) 82–89.

https://doi.org/10.1016/j.molcata.2007.09.030.

[59] Y. Yuan, S. Garg, J. Ma, T.D. Waite, Kinetic Modeling-Assisted Mechanistic Understanding of the Catalytic Ozonation Process Using Cu-Al Layered Double Hydroxides and Copper Oxide Catalysts, Environ. Sci. Technol. 55 (2021) 13274–13285. https://doi.org/10.1021/acs.est.1c03718.

[60] S.S. Sable, P.P. Ghute, D. Fakhrnasova, R.B. Mane, C. V. Rode, F. Medina, S. Contreras, Catalytic ozonation of clofibric acid over copper-based catalysts: In situ ATR-IR studies, Appl. Catal. B Environ. 209 (2017) 523–529. https://doi.org/10.1016/j.apcatb.2017.02.071.

[61] T. Zhang, J.P. Croué, Catalytic ozonation not relying on hydroxyl radical oxidation: A selective and competitive reaction process related to metal-carboxylate complexes, Appl. Catal. B Environ. 144 (2014) 831–839. https://doi.org/10.1016/j.apcatb.2013.08.023.

[62] A. Xie, J. Dai, X. Chen, J. He, Z. Chang, Y. Yan, C. Li, Hierarchical porous carbon materials derived from a waste paper towel with ultrafast and ultrahigh performance for adsorption of tetracycline, RSC Adv. 6 (2016) 72985–72998. https://doi.org/10.1039/c6ra17286e.

[63] H. Tamura, A. Tanaka, K. ya Mita, R. Furuichi, Surface hydroxyl site densities on metal oxides as a measure for the ion-exchange capacity, J. Colloid Interface Sci. 209 (1999) 225–231. https://doi.org/10.1006/jcis.1998.5877.

[64] J. Ali, W. Jiang, A. Shahzad, J. Ifthikar, X. Yang, B. Wu, D.T. Oyekunle, W. Jia, Z. Chen, L. Zheng, Z. Chen, Isolated copper ions and surface hydroxyl groups as a

function of non-redox metals to modulate the reactivity and persulfate activation mechanism of spinel oxides, Chem. Eng. J. 425 (2021). https://doi.org/10.1016/j.cej.2021.130679.

[65] Q. Fu, T. Wagner, M. Rühle, Hydroxylated α-Al2O3 (0 0 0 1) surfaces and metal/α-Al2O3 (0 0 0 1) interfaces, Surf. Sci. 600 (2006) 4870–4877. https://doi.org/10.1016/j.susc.2006.08.008.

[66] J.F. Sanz, N.C. Hernández, Mechanism of Cu deposition on the α-Al2O3 (0001) surface, Phys. Rev. Lett. 94 (2005) 2–5. https://doi.org/10.1103/PhysRevLett.94.016104.

[67] X. Ren, S. Yang, X. Tan, C. Chen, G. Sheng, X. Wang, Mutual effects of copper and phosphate on their interaction with γ-Al2O3: Combined batch macroscopic experiments with DFT calculations, J. Hazard. Mater. 237–238 (2012) 199–208. https://doi.org/10.1016/j.jhazmat.2012.08.032.

[68] Z. Wang, H. Wan, B. Liu, X. Zhao, X. Li, H. Zhu, X. Xu, F. Ji, K. Sun, L. Dong, Y. Chen, Influence of magnesia modification on the properties of copper oxide supported on γ-alumina, J. Colloid Interface Sci. 320 (2008) 520–526. https://doi.org/10.1016/j.jcis.2008.02.001.

[69] T. Zhang, C. Li, J. Ma, H. Tian, Z. Qiang, Surface hydroxyl groups of synthetic α-FeOOH in promoting {radical dot}OH generation from aqueous ozone: Property and activity relationship, Appl. Catal. B Environ. 82 (2008) 131–137. https://doi.org/10.1016/j.apcatb.2008.01.008.

[70] K.M. Bulanin, J.C. Lavalley, A.A. Tsyganenko, IR spectra of adsorbed ozone,

Colloids Surfaces A Physicochem. Eng. Asp. 101 (1995) 153–158. https://doi.org/10.1016/0927-7757(95)03130-6.

[71] H.H. Kung, ed., Surface acidity, 1989. https://doi.org/10.1016/S0167-2991(08)60928-3.

[72] P. Kumar, A.K. Shah, J.H. Lee, Y.H. Park, U.L. Štangar, Selective Hydrogenolysis of Glycerol over Bifunctional Copper-Magnesium-Supported Catalysts for Propanediol Synthesis, Ind. Eng. Chem. Res. 59 (2020) 6506–6516. https://doi.org/10.1021/acs.iecr.9b06978.

[73] International Union of Crystallography, Acta crystallographica. Section B, Structural science., Published for the International Union of Crystallography by Blackwell Pub, 2012. https://inis.iaea.org/search/search.aspx?orig_q=RN:23047167 (accessed November 20, 2023).

[74] C.D. Wagner, NIST X-ray Photoelectron Spectrometry Database, NIST Stand. Ref. Database 20, Version 4.1. (1991) 1–76. http://srdata.nist.gov/xps/Default.aspx.

[75] S. Ardizzone, C.L. Bianchi, M. Fadoni, B. Vercelli, Magnesium salts and oxide: An XPS overview, Appl. Surf. Sci. 119 (1997) 253–259. https://doi.org/10.1016/S0169-4332(97)00180-3.

[76] M.C. Biesinger, Advanced analysis of copper X-ray photoelectron spectra, Surf. Interface Anal. 49 (2017) 1325–1334. https://doi.org/10.1002/sia.6239.

[77] Y. Zhang, Y. Zhou, C. Peng, J. Shi, Q. Wang, L. He, L. Shi, Enhanced activity and stability of copper oxide/γ-alumina catalyst in catalytic wet-air oxidation: Critical roles of cerium incorporation, Appl. Surf. Sci. 436 (2018) 981–988.

https://doi.org/10.1016/j.apsusc.2017.12.036.

[78] J. Batista, A. Pintar, D. Mandrino, M. Jenko, V. Martin, XPS and TPR examinations of γ-alumina-supported Pd-Cu catalysts, Appl. Catal. A Gen. 206 (2001) 113–124. https://doi.org/10.1016/S0926-860X(00)00589-5.

[79] T. Ghodselahi, M.A. Vesaghi, A. Shafiekhani, A. Baghizadeh, M. Lameii, XPS study of the Cu@Cu 2 O core-shell nanoparticles, Appl. Surf. Sci. 255 (2008) 2730–2734. https://doi.org/10.1016/j.apsusc.2008.08.110.

[80] B.R. Strohmeier, Gamma-Alumina (γ-Al2O3) by XPS, Surf. Sci. Spectra. (1994) 135–140.

[81] B.V. Crist, Monochromatic XPS Spectra Commercially Pure Binary Oxides, (2019). https://xpslibrary.com.

[82] P. Kumar, V.C. Srivastava, I.M. Mishra, Dimethyl carbonate synthesis from propylene carbonate with methanol using Cu-Zn-Al catalyst, Energy and Fuels. 29 (2015) 2664–2675. https://doi.org/10.1021/ef502856z.

[83] G.V. Sagar, P.V.R. Rao, C.S. Srikanth, K.V.R. Chary, Dispersion and reactivity of copper catalysts supported on Al 2O3-ZrO2, J. Phys. Chem. B. 110 (2006) 13881–13888. https://doi.org/10.1021/jp0575153.

[84] H. Knözinger, P. Ratnasamy, Catalytic Aluminas : Surface Models and Characterization of Surface sites, Catal. Rev. (1978) 31–70.

[85] M.A. Rodriguez-Olguin, H. Atia, M. Bosco, A. Aguirre, R. Eckelt, E.D. Asuquo, M. Vandichel, J.G.E. Gardeniers, A. Susarrey-Arce, Al2O3 nanofibers prepared from

aluminum Di(sec-butoxide)acetoacetic ester chelate exhibits high surface area and acidity, J. Catal. 405 (2022) 520–533. https://doi.org/10.1016/j.jcat.2021.11.019.

[86] I.B. Moroz, K. Larmier, W.C. Liao, C. Copéret, Discerning γ-Alumina Surface Sites with Nitrogen-15 Dynamic Nuclear Polarization Surface Enhanced NMR Spectroscopy of Adsorbed Pyridine, J. Phys. Chem. C. 122 (2018) 10871–10882. https://doi.org/10.1021/acs.jpcc.8b01823.

[87] P. Hirva, T.A. Pakkanen, The interaction of amine bases on the Lewis acid sites of aluminum oxide - a theoretical study, Surf. Sci. 277 (1992) 389–394. https://doi.org/10.1016/0039-6028(92)90778-5.

[88] C. Sivaraj, S.T. Srinivas, V.N. Rao, P. Kanta Rao, Selectivity dependence on the acidity of copper-alumina catalysts in the dehydrogenation of cyclohexanol1 1 IICT Communication No.: 2487., J. Mol. Catal. 60 (1990). https://doi.org/10.1016/0304-5102(90)85248-G.

[89] C. Hsin-Fu, S. Mohammed Abu, H. Wen-Su, L. Wen-Hsiung, Effect of acidity and copper surface area of the Cu/Al2O3 catalyst prepared by electroless plating procedure on dehydrogenation reactions, J. Mol. Catal. 94 (1994) 233–242. https://doi.org/10.1016/S0304-5102(94)87045-4.

[90] J.A. Lercher, C. Colombier, H. Noller, Acid-Base Properties of Al203/MgO Oxides: III. Infrared study of adsorption of pyrrole, Zeitschrift Fur Phys. Chemie. 131 (1982) 111–122. https://doi.org/10.1524/zpch.1982.131.1.111.

[91] J. Shen, M. Tu, C. Hu, Structural and Surface Acid/Base Properties of Hydrotalcite-Derived MgAlO Oxides Calcined at Varying Temperatures, J. Solid State Chem. 137

(1998) 295–301. https://doi.org/10.1006/jssc.1997.7739.

[92] G. Bagnasco, Improving the selectivity of NH3 TPD measurements, J. Catal. 159 (1996) 249–252. https://doi.org/10.1006/jcat.1996.0085.

[93] M.C. Sánchez-Sánchez, R.M. Navarro, J.L.G. Fierro, Ethanol steam reforming over Ni / Mx Oy-Al2 O3 (M = Ce, La, Zr and Mg) catalysts: Influence of support on the hydrogen production, Int. J. Hydrogen Energy. 32 (2007) 1462–1471. https://doi.org/10.1016/j.ijhydene.2006.10.025.

[94] H. Chen, C. Fang, X. Gao, G. Jiang, X. Wang, S.P. Sun, W. Duo Wu, Z. Wu, Sintering- and oxidation-resistant ultrasmall Cu(I)/(II) oxides supported on defect-rich mesoporous alumina microspheres boosting catalytic ozonation, J. Colloid Interface Sci. 581 (2021) 964–978. https://doi.org/10.1016/j.jcis.2020.09.002.

[95] T. Zhang, W. Li, J.P. Croué, A non-acid-assisted and non-hydroxyl-radical-related catalytic ozonation with ceria supported copper oxide in efficient oxalate degradation in water, Appl. Catal. B Environ. 121–122 (2012) 88–94. https://doi.org/10.1016/j.apcatb.2012.03.021.

[96] L. Ke, J. Liu, L. Sun, F. Pan, X. Yuan, D. Xia, A non-specific surface area dominated catalytic ozonation with CuO modified β-MnO2 in efficient oxalic acid degradation, J. Water Process Eng. 46 (2022) 102535. https://doi.org/10.1016/j.jwpe.2021.102535.

[97] L. Zhang, Y. Li, J. Guo, Z. Kan, Y. Jia, Catalytic ozonation mechanisms of Norfloxacin using Cu–CuFe2O4, Environ. Res. 216 (2023) 114521. https://doi.org/10.1016/j.envres.2022.114521.

[98] S.P. Chenakin, R. Szukiewicz, R. Barbosa, N. Kruse, Surface analysis of transition metal oxalates: Damage aspects, J. Electron Spectros. Relat. Phenomena. 209 (2016) 66–77. https://doi.org/10.1016/j.elspec.2016.04.001.

[99] S. Chenakin, N. Kruse, XPS characterization of transition metal oxalates, Appl. Surf. Sci. 515 (2020). https://doi.org/10.1016/j.apsusc.2020.146041.

[100] M.S. Alam, M. Camredon, A.R. Rickard, T. Carr, K.P. Wyche, K.E. Hornsby, P.S. Monks, W.J. Bloss, Total radical yields from tropospheric ethene ozonolysis, Phys. Chem. Chem. Phys. 13 (2011) 11002–11015. https://doi.org/10.1039/c0cp02342f.

[101] H. Zhang, C.R. Ruehl, A.W.H. Chan, T. Nah, D.R. Worton, G. Isaacman, A.H. Goldstein, K.R. Wilson, OH-initiated heterogeneous oxidation of cholestane: A model system for understanding the photochemical aging of cyclic alkane aerosols, J. Phys. Chem. A. 117 (2013) 12449–12458. https://doi.org/10.1021/jp407994m.

[102] M.A. Oturan, M. Pimentel, N. Oturan, I. Sirés, Reaction sequence for the mineralization of the short-chain carboxylic acids usually formed upon cleavage of aromatics during electrochemical Fenton treatment, Electrochim. Acta. 54 (2008) 173–182. https://doi.org/10.1016/j.electacta.2008.08.012.

[103] J. Song, S.A. Messele, L. Meng, Z. Huang, M. Gamal El-Din, Adsorption of metals from oil sands process water (OSPW) under natural pH by sludge-based Biochar/Chitosan composite, Water Res. 194 (2021) 116930. https://doi.org/10.1016/j.watres.2021.116930.

[104] E. Canada, Canadian Environmental Protection Act, 1999 Federal Environmental Quality Guidelines, Gov. Canada. (2022) 17. http://www.ec.gc.ca/ese-

ees/38E6993C-76AA-4486-BAEB-
D3828B430A6E/PFOS_En.pdf%5Cnhttps://www.ec.gc.ca/ese-
ees/default.asp?lang=En&n=05DF7A37-1.

[105] A.S. Fajardo, R.C. Martins, R.M. Quinta-Ferreira, Treatment of a simulated phenolic effluent by heterogeneous catalytic ozonation using Pt/Al2O3, Environ. Technol. (United Kingdom). 34 (2013) 301–311. https://doi.org/10.1080/09593330.2012.692720.

[106] A.S. Cardwell, W.J. Adams, R.W. Gensemer, E. Nordheim, R.C. Santore, A.C. Ryan, W.A. Stubblefield, Chronic toxicity of aluminum, at a pH of 6, to freshwater organisms: Empirical data for the development of international regulatory standards/criteria, Environ. Toxicol. Chem. 37 (2018) 36–48. https://doi.org/10.1002/etc.3901.

[107] J.R. Bolton, K.G. Bircher, W. Tumas, C.A. Tolman, Figures-of-merit for the technical development and application of advanced oxidation technologies for both electric- and solar-driven systems, Pure Appl. Chem. 73 (2001) 627–637. https://doi.org/10.1351/pac200173040627.

[108] Y. Cheng, B. Wang, P. Yan, J. Shen, J. Kang, S. Zhao, X. Zhu, L. Shen, S. Wang, Y. Shen, Z. Chen, In-situ formation of surface reactive oxygen species on defective sites over N-doped biochar in catalytic ozonation, Chem. Eng. J. 454 (2023) 140232. https://doi.org/10.1016/j.cej.2022.140232.

[109] J.T. R. Tracy Wright, Kellie Fay, Amuel Kennedy, Kelly Mayo-Bean, Kendra Moran-Bruce, William Meylan, Peter Ranslow, Michele Lock, J. Vince Nabholz,

Justine Von Runnen, Lauren M. Cassidy, Operation manual for the ecolological Structure-Activity Relationship Model (ECOSAR) Class Program, U.S. Environ. Prot. Agency. (2022) 1–42. https://www.epa.gov/tsca-screening-tools/ecological-structure-activity-relationships-ecosar-predictive-model.

[110] F.N. Lambert, D.N. Vivian, S. Raimondo, C.T. Tebes-Stevens, M.G. Barron, Relationships Between Aquatic Toxicity, Chemical Hydrophobicity, and Mode of Action: Log Kow Revisited, Arch. Environ. Contam. Toxicol. 83 (2022) 326–338. https://doi.org/10.1007/s00244-022-00944-5.

[111] GHS (United Nations), Globally harmonized system of classification and labelling of chemicals (GHS)(4th Edition), United Nations. (2021) 3–539.

Appendix A: TOC calibration curve

The TOC content measurements in this work were performed using a TC-IC method. Fig. A.1 presents the calibration curve used for TOC analysis.

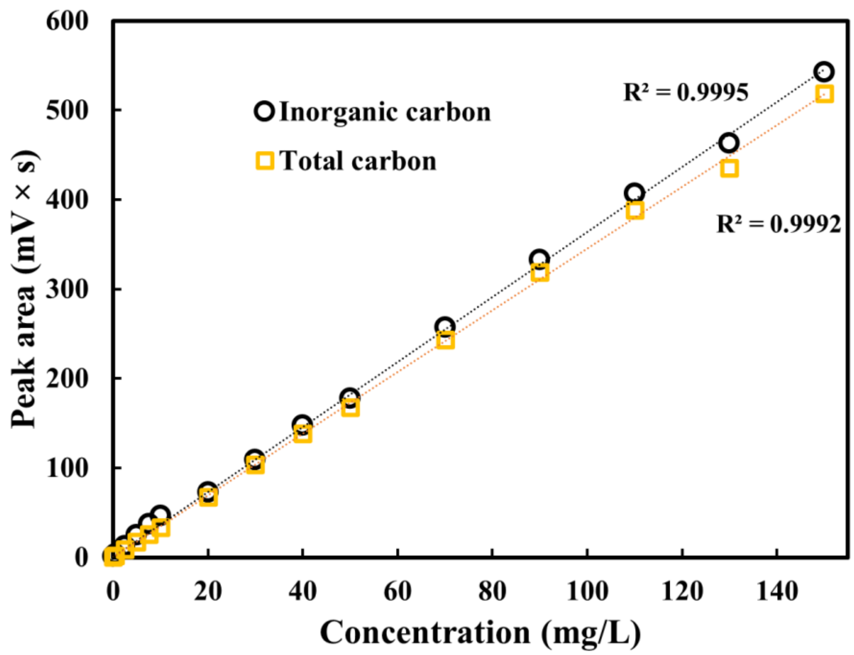

Fig. A.1. Calibration curve for TC and IC measurements.

Appendix B: Repeatability of experiments

Selected ozonation experiments were performed in triplicate. A maximum standard deviation of ±3% TOC removal was observed, confirming the repeatability and reliability of the data obtained. Figure B.1 shows the normalized TOC profiles with error bars for the single ozonation of 4PCH. The normalized TOC profiles of 4PCH ozonation by Cu(1)Mg(5)/γ-Al_2O_3 at two dosages of 1 and 2 g/L are shown in Figures B.2 and B.3, respectively.

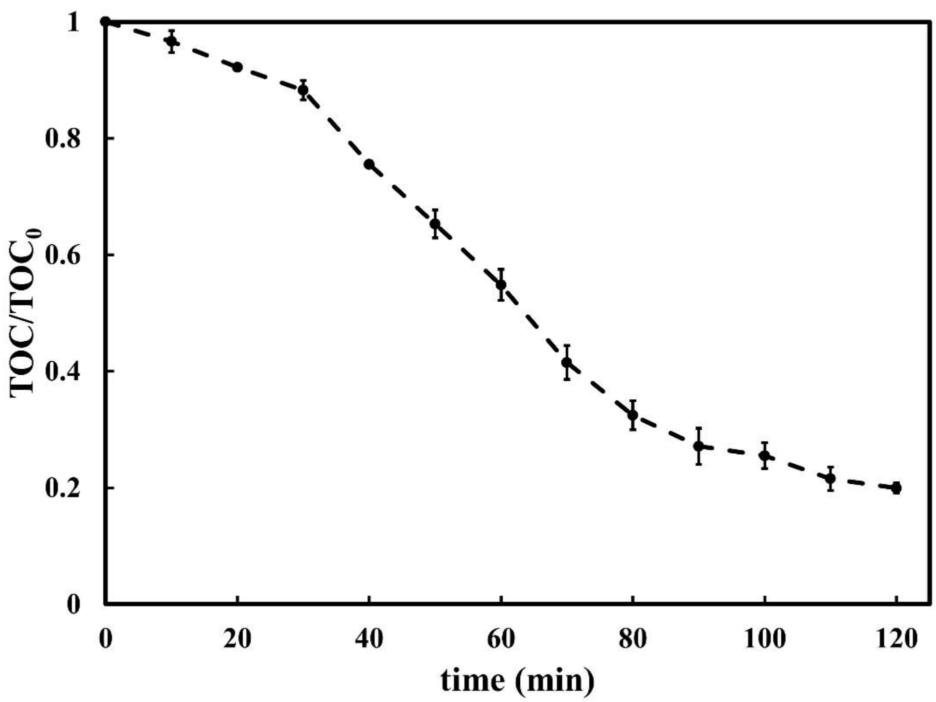

Fig. B.1. Single ozonation of 4PCH. Initial 4PCH concentration = 40 mg/L (TOC_0 = 29 mg/L), bicarbonate ionic strength = 5 mM, inlet gas phase ozone concentration = 23,616 ppmv, and initial pH = 8.5.

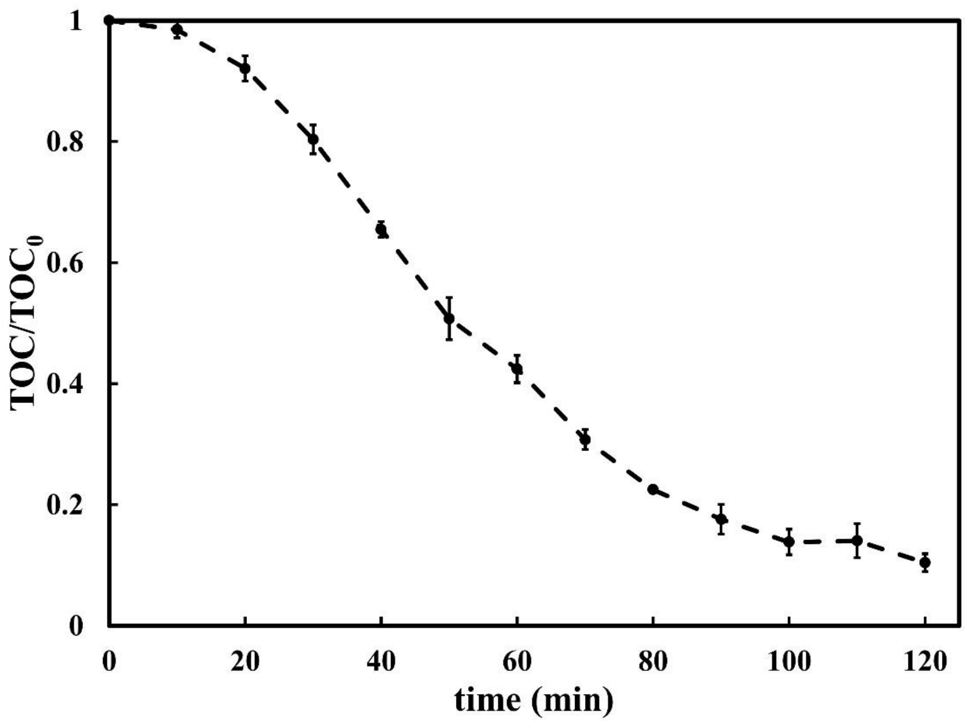

Fig. B.2. Catalytic ozonation of 4PCH using 1 g/L of Cu(1)Mg(5)/γ-Al_2O_3. Initial 4PCH concentration = 40 mg/L (TOC_0 = 29 mg/L), bicarbonate ionic strength = 5 mM, inlet gas phase ozone concentration = 23,616 ppmv, and initial pH = 8.5.

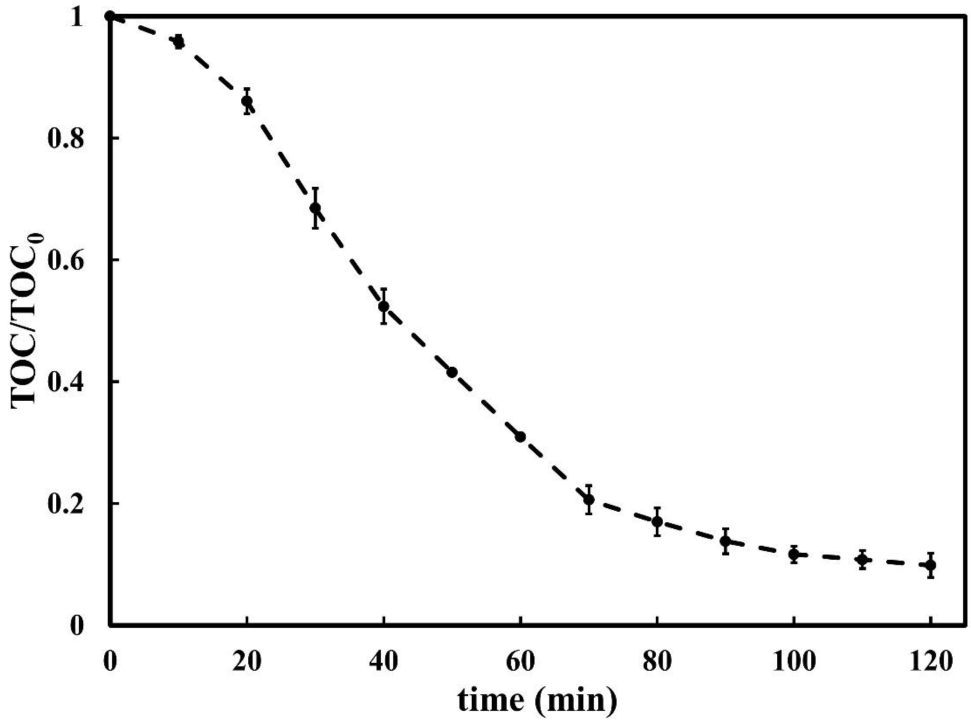

Fig. B.3. Catalytic ozonation of 4PCH using 2 g/L of Cu(1)Mg(5)/γ-Al_2O_3. Initial 4PCH concentration = 40 mg/L (TOC_0 = 29 mg/L), bicarbonate ionic strength = 5 mM, inlet gas phase ozone concentration = 23,616 ppmv, and initial pH = 8.5.

Appendix C: Mass transfer limitations

In order to confirm that there were no external mass transfer limitations on the HCO of 4PCH using 2 g/L of Cu(1)Mg(5)/γ-Al_2O_3, the stirring speed of the reactor was increased to 700 rpm. Fig. C.1 shows the normalized TOC profile at 700 rpm and its comparison to that of 600 rpm. The normalized TOC profile obtained at 700 rpm was almost identical to that of the experiment at 600 rpm, showing that there were no external mass transfer effects for the adsorption of reactants from the bulk of the liquid phase to the surface of the catalyst and for the desorption of by-products from the surface of the catalyst to the bulk of the liquid phase.

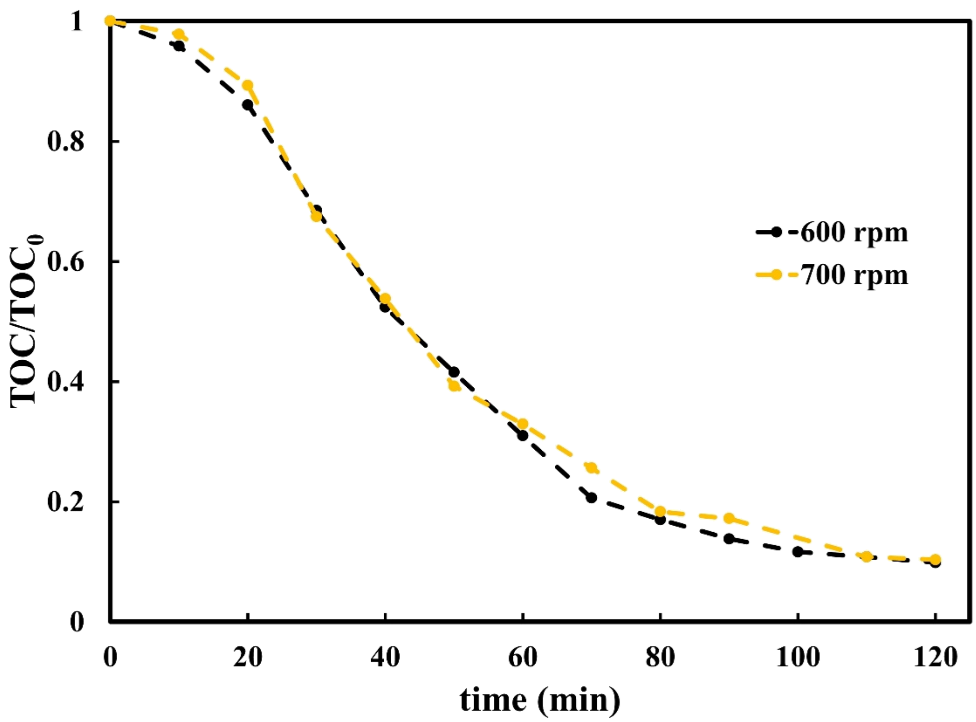

Fig. C.1. Catalytic ozonation of 4PCH using Cu(1)Mg(5)/γ-Al_2O_3 at different stirring speeds. Initial 4PCH concentration = 40 mg/L (TOC_0 = 29 mg/L), bicarbonate ionic strength = 5 mM, inlet gas phase ozone concentration = 23,616 ppmv, catalyst dosage = 2 g/L and initial pH = 8.5.

The absence of internal mass transfer limitations was proven by using two different catalyst particle sizes of less than 105 µm and between 105 and 210 µm. Fig. C.2 shows the normalized TOC profiles of the ozonation of 4PCH using 2 g/L of Cu(1)Mg(5)/γ-Al_2O_3 at the two range of particle sizes. Both normalized TOC profiles were nearly the same, confirming that particles with a size range of 105 – 210 µm were sufficiently small to allow for surface reactions without internal mass transfer limitations.

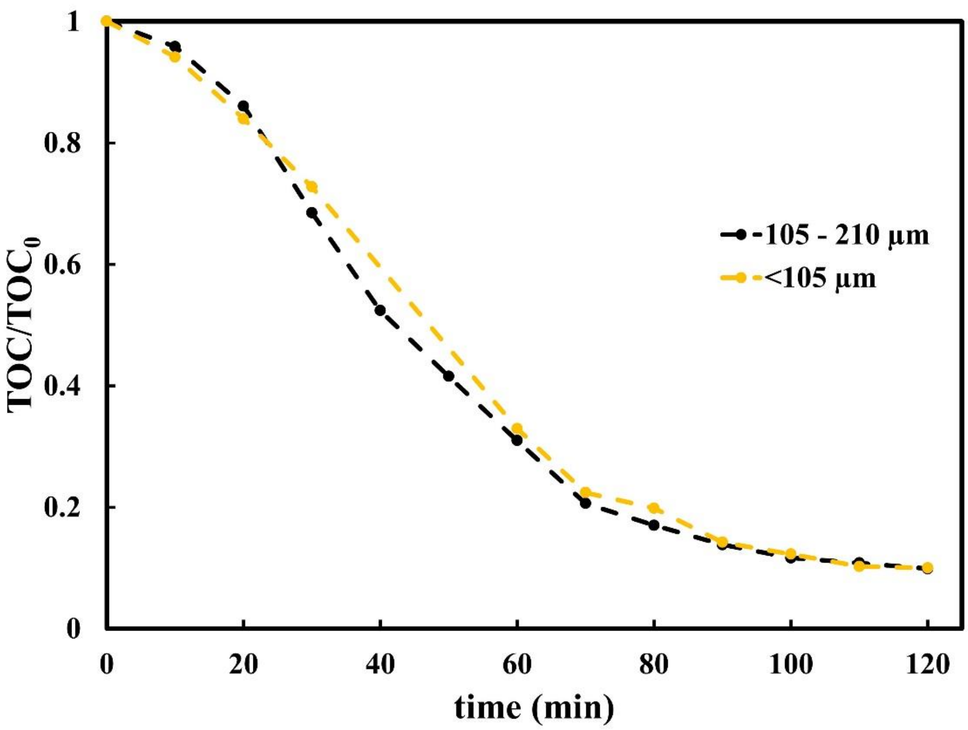

Fig. C.2. Catalytic ozonation of 4PCH using Cu(1)Mg(5)/γ-Al_2O_3 at different particle sizes. Initial 4PCH concentration = 40 mg/L (TOC_0 = 29 mg/L), bicarbonate ionic strength = 5 mM, inlet gas phase ozone concentration = 23,616 ppmv, catalyst dosage = 2 g/L and initial pH = 8.5.